HORIZON 2020
The EU Framework Programme for Research and Innovation

Urban Cross-cutting Applications Development Report

Deliverable D3.4

DATE
31 December 2022

ISSUE
2.0

GRANT AGREEMENT
no 870337

DISSEMINATION LEVEL
PU

PROJECT WEB-SITE
http://cure-copernicus.eu/

LEAD AUTHOR
Zina Mitraka (FORTH)

CO-AUTHORS
Nektarios Chrysoulakis, Giannis Lantzanakis (FORTH), Benjamin Leutner, Mattia Marconcini (DLR), Christian Feigenwinter (UNIBAS), Katerina Jupova, Jan Kolomaznik, Miroslav Kopecky, Erika Orlitova, Tomas Soukup (GISAT), Dirk Lauwaet, Hans Hooyberghs (VITO), Alessandra Gandini, Daniel Navarro, Efren Feliu (TECNALIA), Birgitte Holt Andersen, Louise Kjær-Hansen (CWare)

1 INTRODUCTION

1.1 Purpose of this document

This document is the deliverable D3.4 of the CURE (Copernicus for Urban Resilience in Europe) Project. The goal of this deliverable is to fully describe the development process of the 11 CURE Cross-Cutting Applications, including the list of Copernicus and non-Copernicus data used as input, the algorithms and methods adapted for the needs of CURE, example of resulting products for the CURE front-runner and follower cities and the methods evaluation and the dockerization process.

The CURE applications are developed for at least one front-runner city and one or more follower cities. Table 1 lists the applications per city, as decided after consultation with the users (details in CURE D1.1).

Figure 1 shows the dependency of the CURE applications to the Copernicus Core Services.

In the next Chapters, the applications are presented one by one, in the same order as Table 1.

Table 1. *CURE Applications study sites.*

AP	Cross-cutting applications	Berlin	Copenhagen	Sofia	Heraklion	Bristol	Ostrava	Basel	Munich	San Sebastian	Vitoria-Gasteiz
01	Local Scale Surface Temperature Dynamics (FORTH)	●	●	●	●	●	●	●	●	●	●
02	Surface Urban Heat Island Assessment (DLR)	●	●	●	●	●	●	●	●	●	●
03	Urban Heat Emissions Monitoring (UNIBAS)				●			●			
04	Urban CO_2 Emissions Monitoring (UNIBAS)				●			●			
05	Urban Flood Risk (GISAT)				●		●				
06	Urban Subsidence, Movements and Deformation Risk (GISAT)				●		●				
07	Urban Air Quality (VITO)			●		●	●				
08	Urban Thermal Comfort (VITO)		●	●			●			●	
09	Urban Heat Storage Monitoring (FORTH)				●			●			
10	Nature Based Solutions (TECNALIA)			●						●	
11	Health Impacts (socioeconomic perspective) (CWare)		●	●		●					

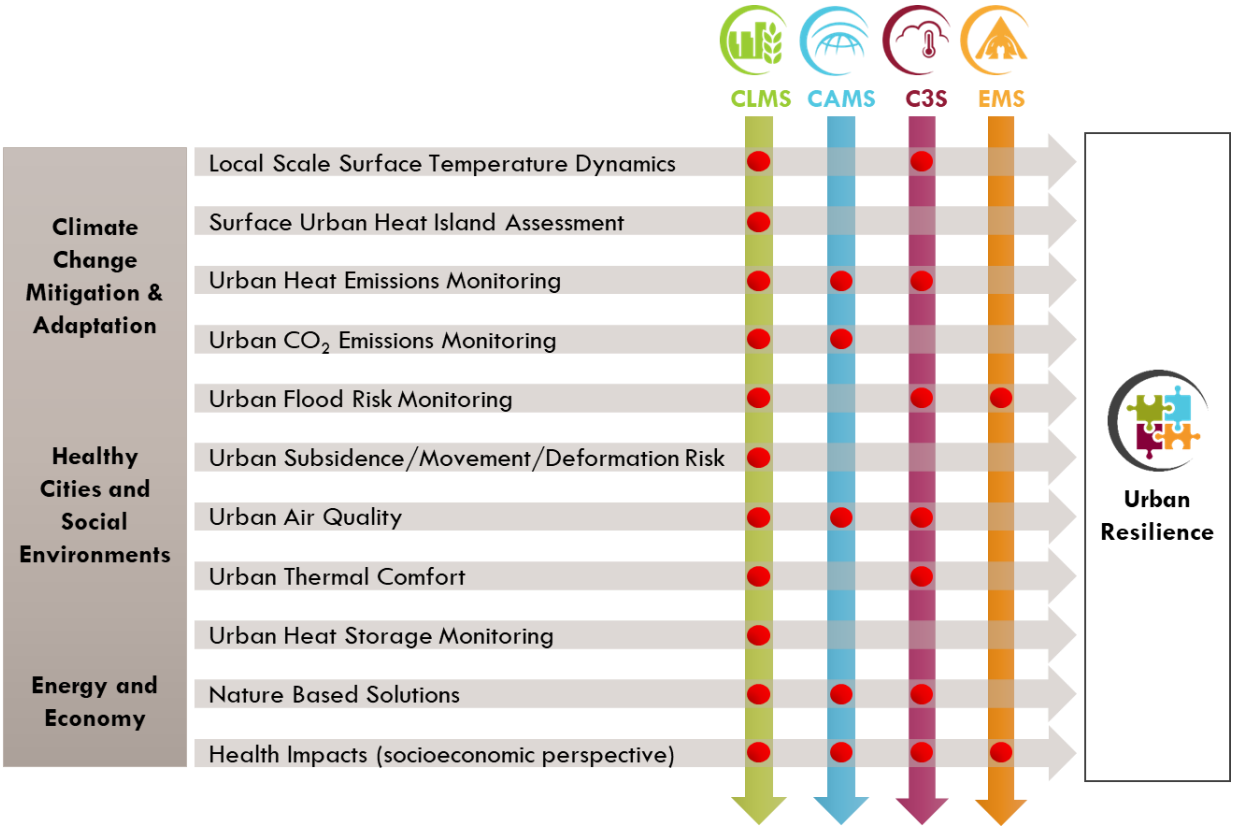

Figure 1. CURE cross-cutting applications among the Copernicus Core Services.

1.2 Definitions and acronyms

Acronyms

AOI	Area of Interest
AP	CURE Application followed by number, i.e. 01 to 11
ARM	Aerodynamic Resistance Method
C3S	Copernicus Climate Change Service
CAMS	Copernicus Atmospheric Service
CLMS	Copernicus Land Monitoring Service
CURE	Copernicus for Urban Resilience in Europe
DOM	Digital Object Model
DSM	Digital Surface Model
DTM	Detailed terrain model
EC	Eddy Covariance
EMS	Copernicus Emergency Service
EO	Earth Observation
EVA	Economic Valuation of Air pollution
IFDM	Immission Frequency Distribution Model
IMD HRL	imperviousness density
InSAR	Synthetic Aperture Radar Interferometry
LST	Land Surface Temperature
MOST	Monin-Obukhov similarity theory
NBS	Nature-based solutions
NRT	Near Real Time
PSI	Persistent Scatterer Interferometry
QA/QC	quality assessment and quality control
SUHII	Surface Heat Island Intensity Indicator
UHI	Urban Heat Island
UHII	UHI indicators
UMEP	Urban Multi-scale Environmental Predictor
VHR	Very High Resolution
WP	Work Package
WSFE	World Surface Footprint Evolution

2 AP01 LOCAL SCALE SURFACE TEMPERATURE DYNAMICS

2.1 Data & Methodology

2.1.1 Data

AP01 is implemented for all CURE front-runners cities: Berlin, Copenhagen, Heraklion and Sofia and all the follower cities: Bristol, Ostrava, Basel, Munich, San Sebastian and Vitoria-Gasteiz.

Table 2 lists the data used for the AP01. AP01 is using data from two Copernicus Services (CLMS and C3S), data from two Copernicus Satellites, Sentinel-2 and Sentinel-3, and very high resolution optical third-party data from the Copernicus Contributing missions Data Warehouse (Copernicus, 2020).

Table 2. *Summary of data used for AP01.*

Data Source	Description of the Product
CLMS	Imperviousness
CLMS	Urban Atlas
CLMS	Urban Atlas: Building Heights
CLMS	High Resolution Vegetation Phenology and Productivity
C3S	UERRA regional reanalysis for Europe on single levels from 1961 to 2019
C3S	ERA5 hourly data on single levels from 1979 to present
Copernicus Satellite	Sentinel-2, Level-2A Bottom Of Atmosphere (BOA) reflectance images
Copernicus Satellite	Sentinel-3, SLSTR Level-1B thermal imagery
Third-party	Baseline Land Cover from VHR (from the DWH)
Third-party	Material emissivity information from spectral libraries (Kotthaus et al., 2014)

2.1.2 Methodology

The CURE methodology for deriving the local scale urban surface temperature dynamics is outlined in Figure 2. Data from various sources, including the CLMS, are used to achieve the surface characterization and this information is then used to estimate the urban surface emissivity and to downscale the thermal imagery in order to retrieve land surface temperature (LST), given atmospheric information from C3S. The methodology described in Mitraka et al. (2015) is used to downscale the Sentinel-3, 1 km spatial resolution thermal infrared (TIR) imagery, to retrieve the final LST products at local scale (100 m). The methodology for downscaling the thermal bands, requires higher spatial resolution surface cover information. For this VHR land cover information is derived from the VHR optical third-party data available

from the Copernicus Contributing missions Data Warehouse (Copernicus, 2020) is used, as described in CURE D3.5-D3.10. The VHR land cover map is used to derive a local scale (100 m) surface cover fractions map, which contains information on the abundance of each land cover class in 100 m pixel. The surface cover fractions baseline map is updated to capture changes in time, using information from Sentinel-2 imagery. Emissivity maps are estimated using the surface cover maps and ancillary information from spectral libraries. The LST time series is estimated from the downscaled TIR information (using the surface cover), the emissivity and C3S water vapour products.

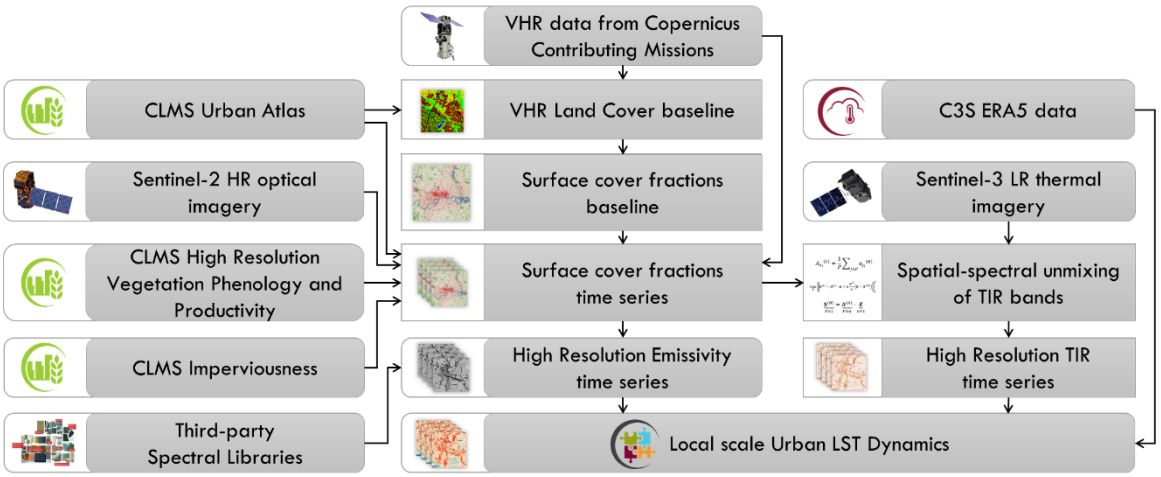

Figure 2. *Methodology for the estimation of Urban Land surface Temperature (LST) dynamics at local scale.*

A surface cover map of very high spatial resolution (2 m) is initially created, from the VHR data available from the DWH (Copernicus, 2020) to serve as baseline, assuming 5 classes (i.e. buildings, paved surfaces, bare soil, vegetation, water surfaces). It is essential to have this information in VHR, to ensure the quality of the resulting products. Surface cover fractions of 100 m spatial resolution are then estimated from the VHR surface cover map, to be used as baseline. The update in time of the baseline map is performed using Sentinel-2 imagery and (when available) CLMS Vegetation Phenology and Productivity data, to capture the changes of the 5 classes.

The vegetation, bare soil and water surfaces classes update is performed using vegetation and water indices approach. The buildings and paved surfaces classes are updated using VHR imagery, CLMS Urban Atlas and CLMS imperviousness data when available and Sentinel-2 optical imagery in the meantime.
The resulting surface cover maps are used to downscale the thermal measurements and to estimate the surface emissivity in local scale using ancillary information from third-party spectral libraries (Mitraka et al., 2012). Different spectral libraries are considered, in order to obtain emissivity information for the different classes. The emissivity information along with the local scale thermal products are then used along with water vapour information from C3S, for the derivation of LST maps using a split-window algorithm (Mitraka et al., 2015).

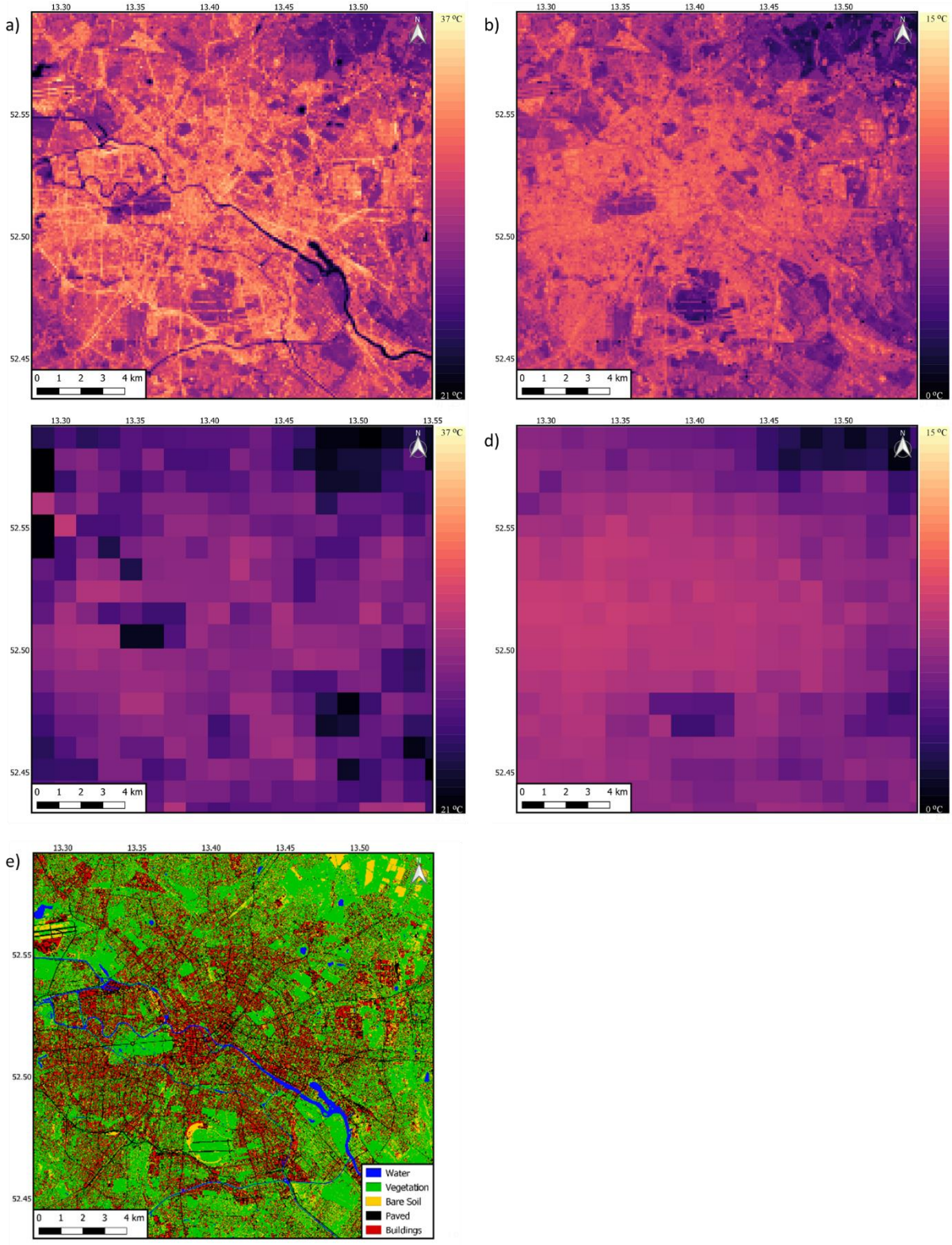

Figure 3. Sample products of AP01: a) Daytime (11.26 local time 30/05/2019) and b) Nighttime (22.32 local time 16/04/2019) Land Surface Temperature (LST) map of 100 m spatial resolution for the city of Berlin and b), c) the respective 1 km spatial resolution products. e) The VHR baseline land cover map is shown for reference.

2.2 Results

The CURE AP01 products are detailed LST maps, which reveal information on the surface temperature of the individual urban surfaces. Figure 3 shows two sample LST product maps for the city of Berlin. The level of detail emerging in the 100 m spatial resolution products (Figure 3a and b) is evident, particularly compared to the 1 km products (Figure 3c and d). In the daytime product (Figure 3a) of May 2019, mid-day (11.26 local time) individual temperatures are observed for different surface covers, i.e. paved surfaces like the road network, the parking lots and airport runaways present higher surface temperatures than urban green spaces, reaching up to 37 ^{o}C). The nighttime product (Figure 3b) corresponds to mid-April 2019, a couple of hours after the sunset. The slow release of heat in the urban surfaces is evident in this surface temperature map, which remain hot compared to the surroundings after the sunset.

While surface temperature maps like this, can directly provide quantitative information for the impact interventions like the application of cool materials in paved surfaces, which immediately would reduce the surface temperature, in order to have a comprehensive overview of the city's heat load, the combination of all CURE heat related applications in needed.

2.3 Evaluation

CURE AP01 was evaluated for the case of Heraklion, Greece and Basel, Switzerland, where LST is available from in-situ measured outgoing radiation in flux towers, using the Stefan Boltzmann law. The evaluation was performed using data from the 100 m × 100 m pixel closest to the location of the radiometer. Although satellite derived T_{LST} may undersample wall temperatures, a tower mounted radiation sensor T_{rad} will have a different proportion of walls impacting the upwelling longwave radiation $L\uparrow$ sensor, which allows determination via the Stefan Boltzmann law:

$$T_{rad} = \left[\frac{L\uparrow-(1-\varepsilon)L\downarrow}{\sigma\varepsilon}\right]^{0.25} \quad , \qquad (1)$$

where ε is the emissivity in the source area (0.97, assumed – but actually variable with facet), σ is the Stefan Boltzmann constant (5.67 x 10^{-8} W m^{-2} K^{-4}) and $L\downarrow$ the downward longwave radiation.

For Heraklion, measurements from HECKOR flux tower were used to calculate the LST, while for Basel, measurements from BKLI, BAES and BLER flux towers are used.

Figure 4 shows the time series of the estimated CURE LST over the HECKOR area and the respective reference LST for daytime and nighttime, while Figure 5 presents the respective scatterplots. Figure 6 shows the CURE LST (K) vs. the reference (K) over the area of the BKLI, BAES and BLER flux towers. A good agreement is generally observed for both cases.

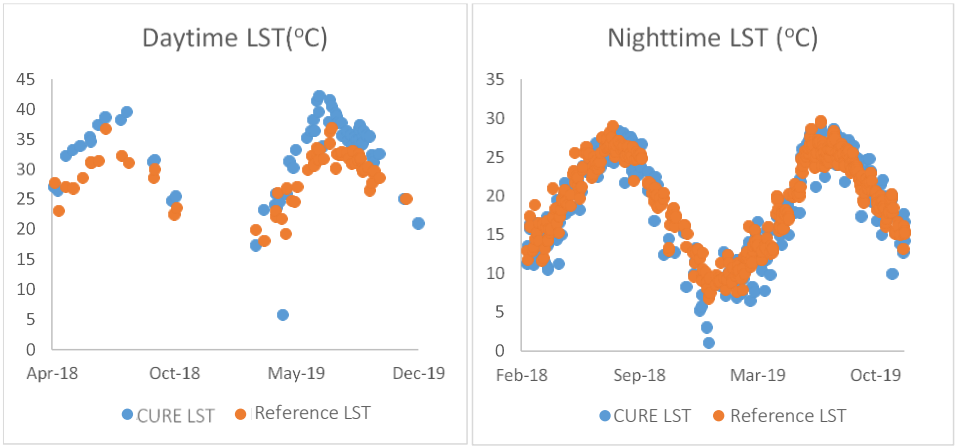

Figure 4. Time series of CURE LST (°C) with blue and reference LST (°C) with orange for (a) daytime and (b) nighttime in Heraklion, Greece, over the area of the HECKOR flux tower, where reference data are available.

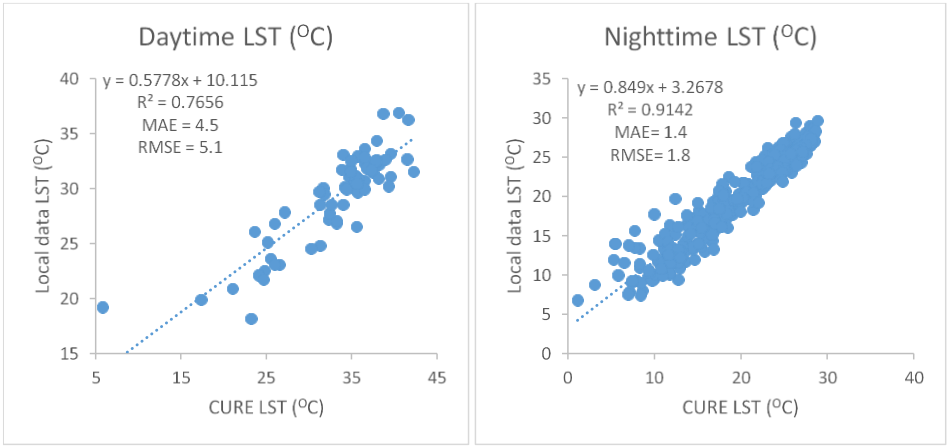

Figure 5. CURE LST vs. reference (°C) for (a) daytime and (b) nighttime in Heraklion, Greece, over the area of the HECKOR flux tower, where reference data are available.

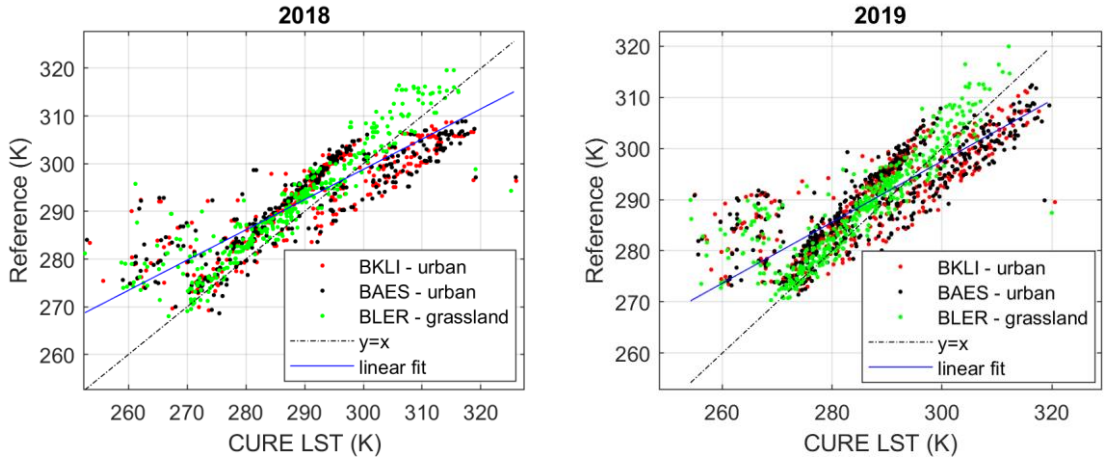

Figure 6. CURE LST vs. reference (K) for (a) 2018 and (b) 2019 in Basel, Switzerland, over the area of the BKLI, BAES and BLER flux towers.

2.4 Application Dockerization

AP01 has been implemented mainly in Matlab®, but it contains also functions from GDAL (in python) and commands from 2 stand-alone software, ESA SNAP and 7zip. It was packaged into a Docker image and can be operated as a standard python module, but also has an API allowing automated requests via parameter specification.

Input data to AP01 are zipped files (.zip) from Sentinel-2 and Sentinel-3 archive, and GRIdded Binary data (.grib) from ERA5 of CAMS, and a high-resolution Landcover map in GeoTiff format (.tif) at WGS84 UTM projection. More specifically, AP01 handles JPEG 2000 (.jp2) and Extensible Markup Language (.xml) data which constitute the content of Sentinel-2 zipped files, and netCDF (.nc) data from Sentinel-3 zipped files. The landcover map must contain 5 classes with the respective values: 1 – water, 2 – vegetation, 3 – bare soil, 4 – paved, 5 – buildings.

The output products of AP01 are time-series of LST in Kelvin at 100 m spatial resolution in GeoTiff format for a given city. Each GeoTiff file corresponds to a single date, same with the Sentinel-3 image was received. It also produces an emissivity map and a landcover fractions map for each date of Sentinel-3 data.

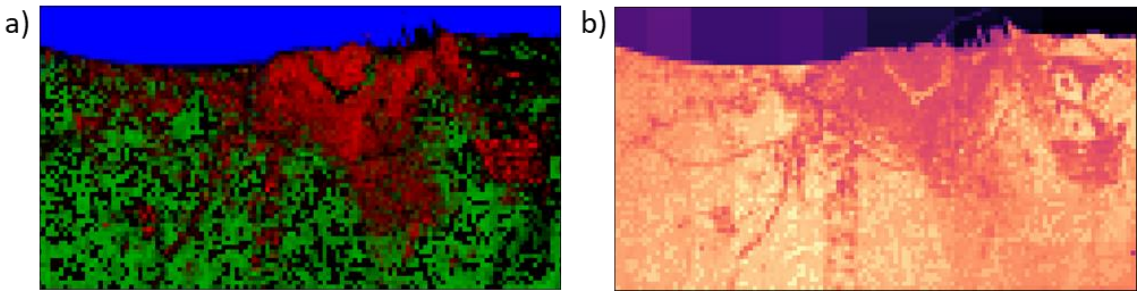

Figure 7. Example products of AP01: a) Intermediate product of Surface Cover Fraction (red: buildings, green: vegetation, blue: water) b) Land Surface Temperature product of 100 m spatial resolution.

3 AP02 SURFACE URBAN HEAT ISLAND ASSESSMENT

3.1 Data & Methodology

Theoretically, the SUHII is defined as the difference in temperature between urban and surrounding rural regions. Traditionally, the quantification of UHII is conducted at two fixed in-situ stations, one in urban and the other in rural regions. Similarly, the remote sensing-based variant, the SUHII, has been derived using selected pixels that are located in the urban and rural regions, respectively. However, it is immediately clear, that single locations or pixels can only reflect part of the SUHI characteristics, especially in cities with multiple UHI centres, and do not necessarily generalize to an entire city. Moreover, the different definitions of "urban" and "rural" regions make the inter-comparison study of SUHII among different cities particularly challenging. To overcome these limitations, the methodology recently presented by Li et al. (2018) is used in CURE. In particular, the intended approach will allow calculating SUHII and its temporal dynamics by exploiting the relationship between land surface temperature (LST) and the percentage impervious surface (PIS), which – according to the literature – proved consistent for cities in biomes dominated by forests and grasslands as in Europe.

3.1.1 Data

There are a number of urban imperviousness products provided through the Copernicus program. In particular, AP02 makes use of the CLMS High Resolution Layers of imperviousness density (IMD HRL), which have been published for the years 2006, 2009, 2012, 2015 and 2018. These serve as the primary data source for the PIS layer. These status layers are available in 20m spatial resolution for the years 2006 to 2015 and 10m spatial resolution for the year 2018.

Figure 8 displays the 2018 IMD HRL for the CURE front-runner cities after pre-processing with the convolution step described in the Methodology section.

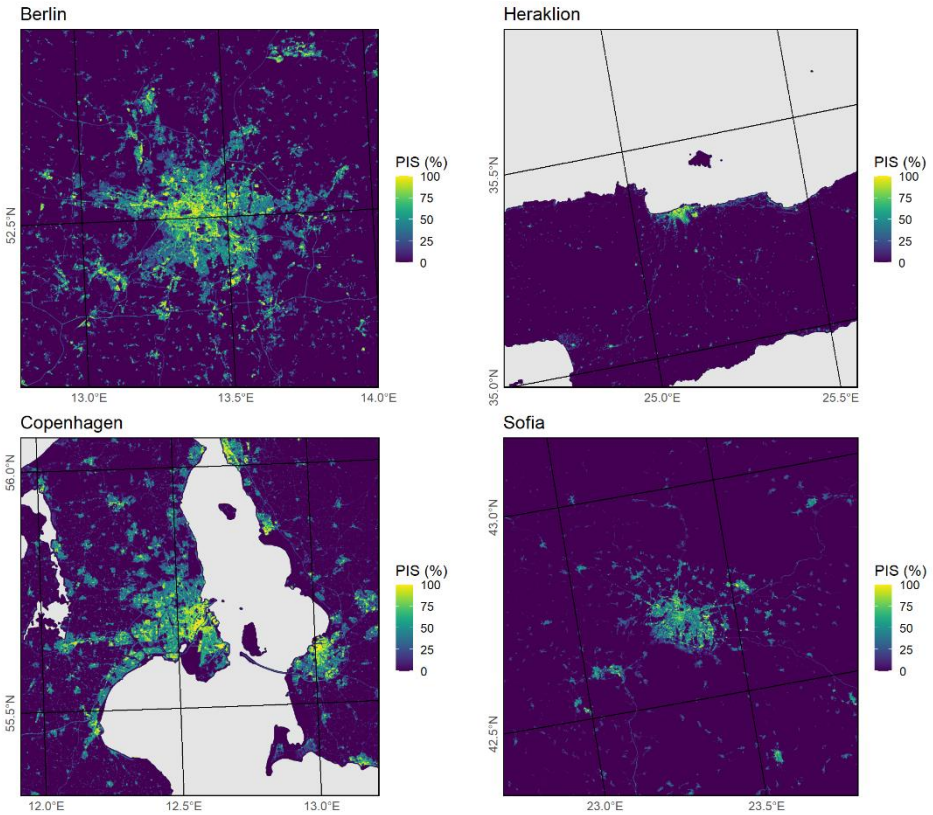

Figure 8. *PIS layer derived from CLMS IMD HRL 2018 for the CURE front-runner cities after convolution with PSF kernel.*

Furthermore, the framework has also been tested in addition on an improved imperviousness product developed in the processing framework of the World Settlement Footprint (Marconcini et al. 2020), which is based on Copernicus Sentinel-2 data for the year 2019 (which can be extended backwards to 2015).

For the LST layer, AP02 relies on land surface temperature data developed and processed in AP01, thus implicitly making use of both CLMS and CAMS data sources. For initial development and pre-Sentinel era analyses, AP02 made use of Landsat 5, Landsat 7 and Landsat 8 derived LST data (Parastatidis et al. 2017).

Figure 9 displays LST composites derived from Landsat 8 TIRS data over the summer months of 2017-2018 for all CURE front-runner as described in the Methodology section.

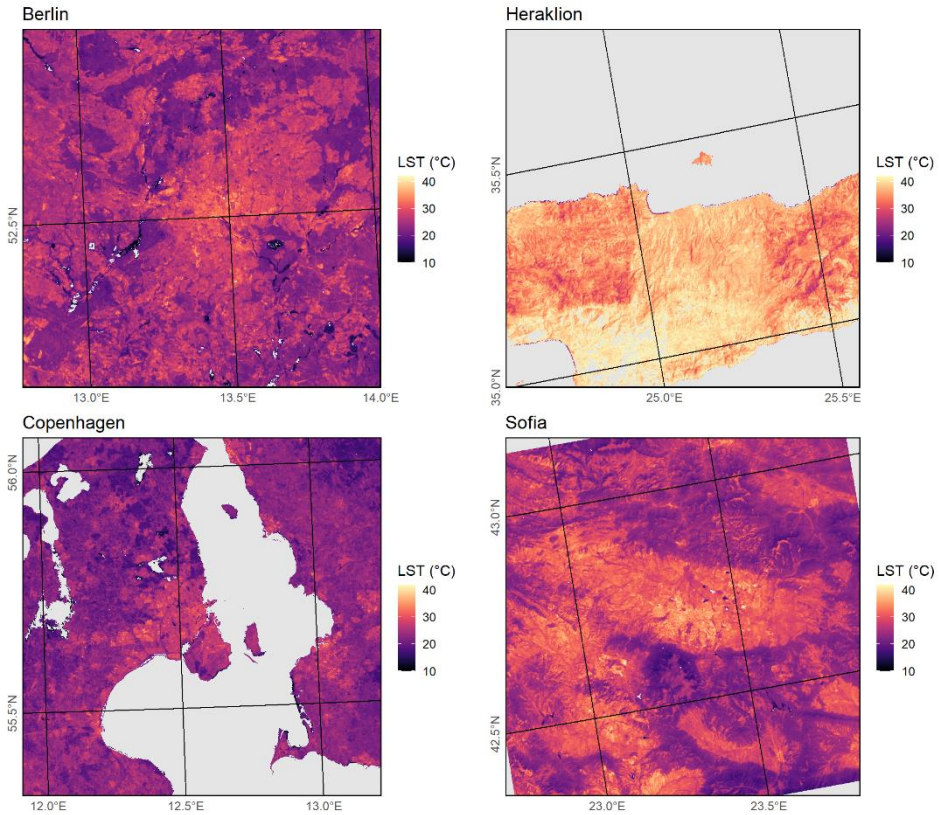

Figure 9. *LST multi-temporal composite layer derived from Landsat 8 TIRS data for the CURE front-runner cities.*

3.1.2 Methodology

Following the state-of-the-art summary given in D1.3, the selected methodology for SUHII derivation is based on performing a regression of the measured LST against the imperviousness degree following the method of Li et al. (2018). The SUHII is then defined as the slope of a linear regression line. This method avoids having to define “urban” and “rural” pixels explicitly.

Figure 11 summarizes the processing steps needed to implement the AP02 processor. The LST data from AP01 described in the previous section is provided on a per-scene basis. LST from individual acquisitions is subject to gaps due to cloud-cover, as well as natural variability of temperatures due to weather. Therefore, in order to obtain a robust characterization of the LST properties, the individual acquisitions are composited by calculating the mean over a given temporal window, which can be set by the user. In our experiments with the Landsat-based LST, to take into consideration the months May to October for two consecutive years proved to be a promising choice. However, this is mostly driven by the 16-day Landsat acquisition frequency in contrast to the daily information expected to be derived based on Sentinel-3 imagery by AP01. With the LST data from AP01 very robust results can be achieved for bi-monthly temporal windows, and for some cites even for monthly intervals.

Next, the imperviousness layer from the CLMS IMD HRLs is processed to match the LST data. Since the spatial resolution of the thermal Landsat bands is 100m and Sentinel 3 is even larger,

plus adjacency effects due to the sensor's point spread function (PSF), the high-resolution PIS data is convolved with a Gaussian kernel of width σ = 50m to correspond to the LST measurement.

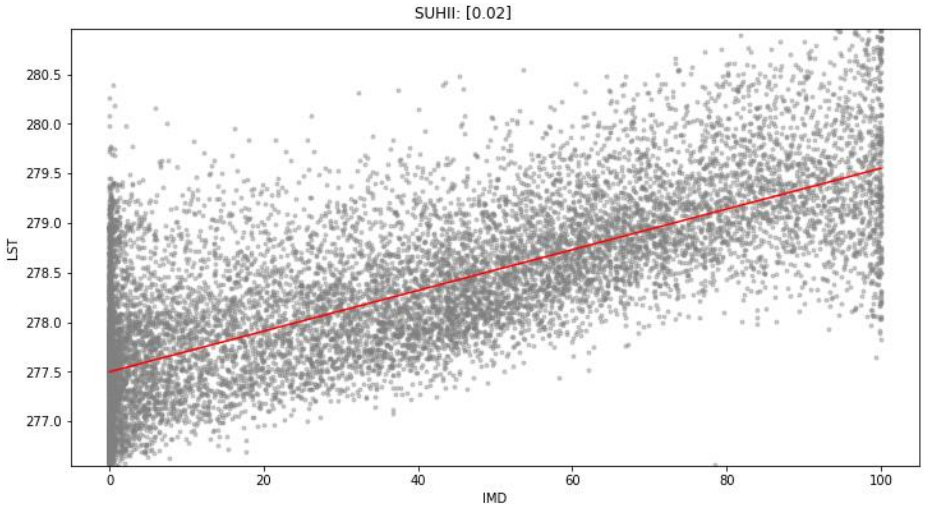

Figure 10. *Exemplary SUHII analysis fro the city of Basel, months January and Februrary 2018 and 2019. The red line is the robust model fit, with a slope (SUHII) of 0.02 LST/IMD. The grey points designate single pixel values. X-axis is the imperviousness density of the CLMS HRL and the y-axis is the LST from a bi-monthly composite of AP01 data.*

.

Subsequently, pixel values are sampled from both the IMD and LST composite using a regular sampling grid and discarding no-data, as well as water pixels. Using these samples, we fit a robust linear model, in order to avoid undue influence of extreme values, as:

$$LST = \beta_0 + \beta_1 \cdot PIS,$$

where finally β_1 defines the SUHII. By using a bootstrapping approach with 50 resamples, it is further possible to derive confidence intervals around the SUHII estimate.

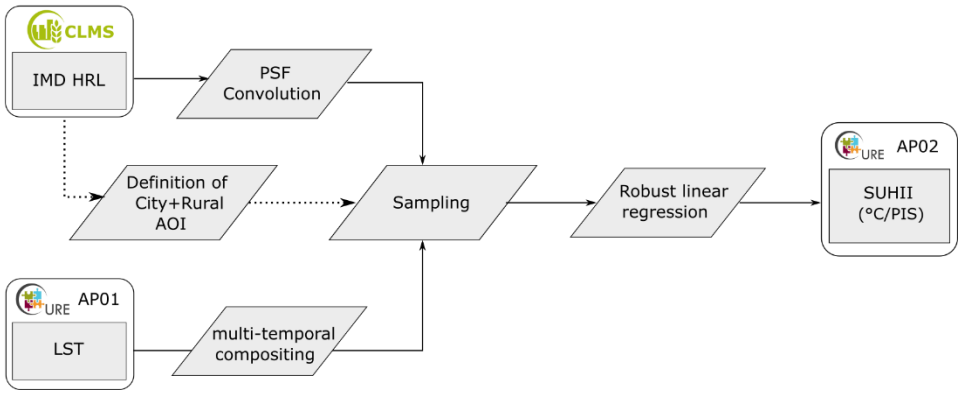

Figure 11. *Simplified flowchart of the AP02 SUHII processor.*

Initial results have been produced for all four CURE front-runner cities with the CLMS IMD HRL 2018 and Landsat 8 LST data, which were calibrated using an emissivity based on Landsat NDVI as well as atmospheric water vapour content derived from the NCEP/NCAR Reanalysis Project as described in Parastatidis (2017).

Figure 12 displays the resulting SUHII index values with their corresponding confidence intervals over variably sized buffers around the city centres. This clearly highlights the sensitivity of the SUHII to the definition of the urban extent, yet also provides an opportunity to define the cut-off in a data-driven manner, for example as the point of initial saturation.

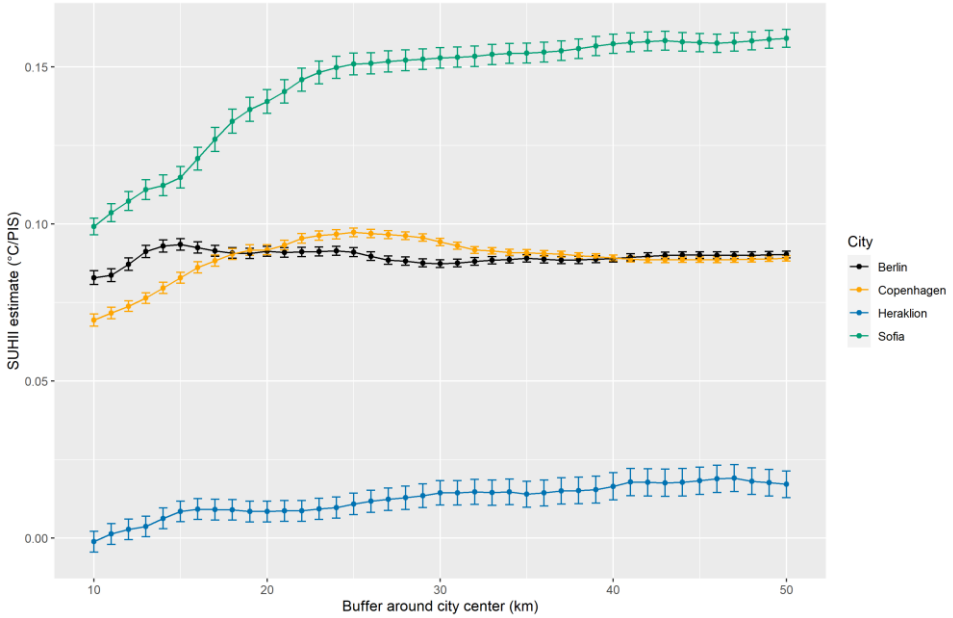

Figure 12. *Estimates of SUHII vary depending on the definition of the city and encompassing rural extent.*

3.2 Results

SUHII temporal profiles were calculated for all frontrunner cities. They clearly distinguish between different thermal properties, as well as their annual dynamics. Results presented below were derived for bi-monthly LST data of the years 2018 and 2019 calculated via CURE AP01. High SUHII values indicate a pronounced heating effect of the city core as opposed to its rural surroundings. Values around zero indicate no effect and negative values indicate an opposite with a cooler city body than the surroundings. Noteworthy in addition to the annual profiles are the diurnal variations, which are complementary in understanding urban thermal properties

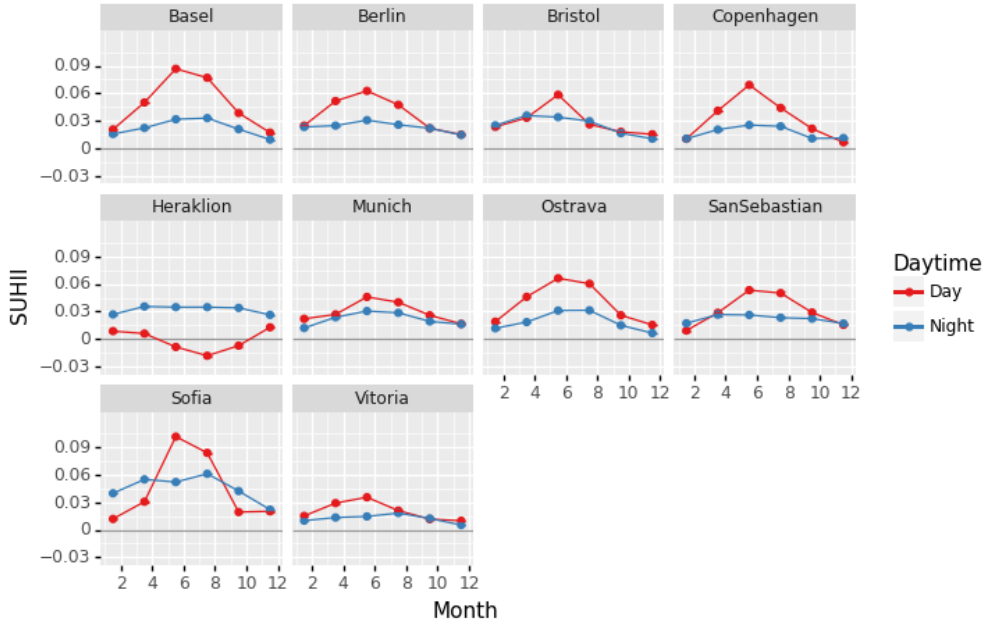

Figure 13. SUHII profiles for all frontrunner and follower cities based on the CLMS HRL IMD 2018 layer.

3.3 Evaluation

AP02 is novel as it is the first attempt to characterize both annual and diurnal temporal dynamics of the urban heat island effect. There are no existing products which provide comparable SUHII values to our knowledge.

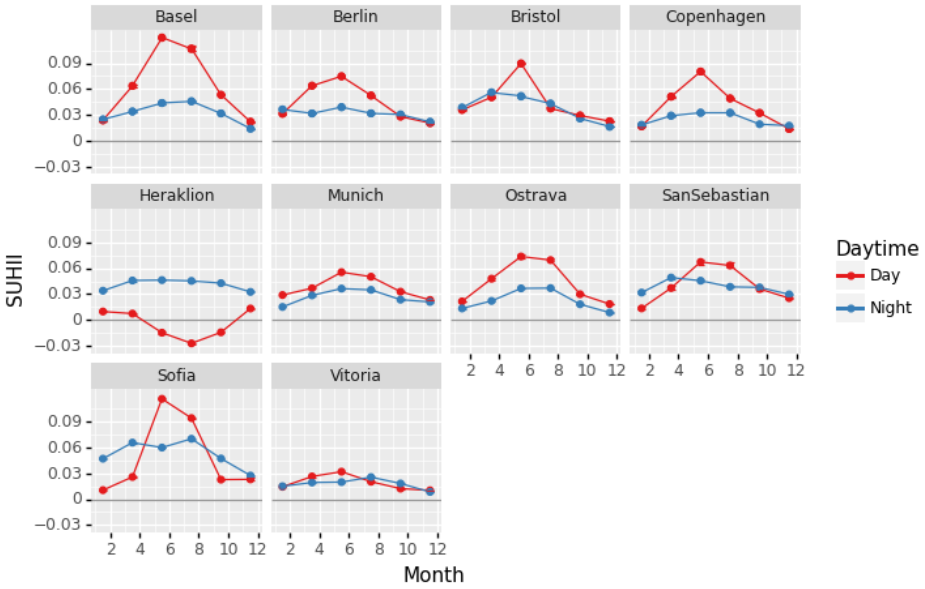

Figure 14. SUHII profiles for all frontrunner and follower cities calculated based on WSF 2019 imperviousness layer.

However, due to our access to alternative IMD data from the World Settlement Footprint (WSF) suite, we compared the impact of differences between WSF IMD and CLMS HRL IMD layers as input data. Both input layers resulted in very similar SUHII profiles, with the absolute dependence of LST on PIS being slightly higher in the case of the WSF layer.

3.4 Application Dockerization

AP02 has been implemented entirely in python and gdal. It was packaged into a Docker image and can be operated as a standard python module, but also has an API allowing automated requests via parameter specification.

Input data to AP02 are PIS data from the CLMS HRL IMD layer and daily AP01 LST data. The processor however is not limited to these data sources and can also operate on other IMD or LST data sets.

The output products of AP02 are time-series of SUHII values for a given city (or all cities) which are produced as JSON files and CSV files. The JSON file contains the machine-readable output of AP02. Each entry corresponds to a single SUHII estimate at a given reference time-period., where the following slots are available:

- [city]: Location
- [filters]: defines the time-period of LST data considered
- [aoi]: city area considered during calculations
- [number_of_scenes]: number of LST acquisition dates considered
- [suhii]: SUHII point estimate
- [suhii_ci]: SUHII 95% confidence interval (lower and upper)

The following example entry shows the results for Sofia, calculated over the months September and October of the years 2018 and 2019 during daytime (resulting in 61 LST products). The SUHII was estimated as 0.02 (0.018, 0.020).


```
{
 "city": "Sofia",
 "filters": {
   "years": [
     2018,
     2019
   ],
   "months": [
     9,
     10
   ],
   "daytimes": [
     "Day"
   ]
 },
 "number_of_scenes": 61,
 "suhii": 0.01904810053785863,
 "suhii_ci": [
   0.017760741169068384,
   0.020176750881793496
 ]
}
```

4 AP03 URBAN HEAT EMISSIONS MONITORING

4.1 Data & Methodology

CURE AP03 is based on the Aerodynamic Resistance Method (ARM) for the estimation of sensible heat flux Q_H at local scale (Voogt and Grimmond, 2000). The ARM was successfully applied in the former URBANFLUXES project (Chrysoulakis et al., 2018) for the calculation of citywide sensible and latent heat flux in a spatial resolution of 100 m x 100 m. In CURE, the ARM implementation described in Feigenwinter et al. (2018) is further developed and adapted to suit the requirements of CURE end users, i.e. city planners and stakeholders. The model results are evaluated with in-situ turbulent sensible heat fluxes measured by the Eddy Covariance (EC) method at urban flux towers (Feigenwinter et al., 2012).

4.1.1 Data

In a first step, AP03 will rely mainly on local (non-Copernicus) data to produce a first implementation of the application. In a second step, the local input data is replaced by Copernicus data, where possible.

- Digital Object Model (DOM): A high resolution (1 m x 1 m) model of buildings and trees is the essential base for calculation of roughness parameters and aerodynamic resistances (see Section 4.2.2).
- Land Surface Temperature (LST): For the LST layer, AP03 relies on land surface temperature data developed and processed in AP01
- Meteorological data: Air temperature, humidity, wind velocity, wind direction, radiation from in-situ measurements
- Turbulent fluxes for evaluation: in-situ measurements from urban flux towers equipped with Eddy Covariance systems

Table 3 provides an overview of the datasets used in AP03.

Table 3. *Input data for AP03 (local and Copernicus).*

Data	Local	Copernicus service
DOM	Available in high resolution for front-runner city Heraklion and follower-city Basel (buildings and trees)	CLMS building heights CLMS street tree layer
LST	LST derived from upwelling longwave radiation measurements for evaluation of AP01 LST product	AP01 LST product
Meteorological data	In-situ measurement network	C3S ERA5 Reanalysis data
Turbulent sensible heat flux Q_H	In-situ EC flux tower	

4.1.2 Methodology

The estimation of sensible heat flux with remote sensing data is based on the bulk transfer approach (Yang et al., 2019), where the surface temperature is derived from satellite data. An implementation of the bulk transfer method is ARM (Voogt and Grimmond, 2000), which is used in several microscale urban climate models.

ARM uses the Monin-Obukhov similarity theory (MOST) (e.g. Foken, 2006) as the theoretical basis to estimate momentum and scalar fluxes in the atmospheric surface layer. MOST is commonly used in meteorological numerical modeling systems. In the MOST framework, roughness lengths for momentum and heat (z_{0m} and z_{0h}, respectively) are the key parameters identifying the aerodynamic features of underlying surfaces (Kanda et al., 2007).

The ARM is a common approach for modelling surface fluxes. Q_H is basically calculated as

$$Q_H = c_p \rho \frac{T_0 - T_A}{r_H} \qquad (4.1)$$

where c_p is the heat capacity of the air (J kg^{-1} K^{-1}), ρ is the air density (kg m^{-3}), T_0 is the surface temperature (K), T_{air} is the air temperature (K) and r_H is the bulk aerodynamic resistance for heat (s m^{-1}) of the complete 3D urban surface (Crawford et al., 2018). T_0 is replaced with the satellite-derived LST product from AP01. Using the radiative surface temperature instead of T_0 requires the completion of r_H with a radiometric excess resistance (Voogt and Grimmond, 2000).

In detail, the aerodynamic resistance for heat r_H will be calculated with

$$r_H = \frac{1}{u_* k}\left[ln\left(\frac{z-z_d}{z_{0m}}\right) - \psi_h\left(\frac{z-z_d}{L}\right) + \ln\left(\frac{z_{0m}}{z_{0h}}\right)\right] \qquad (4.2)$$

$$u_* = Uk\left[ln\left(\frac{z-z_d}{z_{0m}}\right) - \psi_m\left(\frac{z-z_d}{L}\right) - \psi_m\left(\frac{z_{0m}}{L}\right)\right]^{-1} \qquad (4.3)$$

where u_* is the friction velocity, k is the von Karman constant (0.4), z refers to a reference height (usually the height of wind measurements), z_d is the zero-plane displacement height, L is the Monin-Obukhov length, z_{0m} and z_{0h} are the roughness lengths and $\psi_{m,h}$ are the stability functions for momentum and heat, respectively. Equation (4.3) can be used to estimate u_* from wind velocity U, if no direct measurements of the friction velocity is available. z_{0h} values are usually reported as the dimensionless number $k\beta^{-1}$, defined as

$$k\beta^{-1} = ln\left(\frac{z_{0m}}{z_{0h}}\right) \qquad (4.4)$$

$k\beta^{-1}$ is a key parameter in the ARM. In literature, reported values for $k\beta^{-1}$ show a large variability, even for similar types of surfaces. Lowest values of around 2 correspond to homogeneous vegetative surfaces (Brutsaert 1982), but also to flat semi-arid areas (Koshiek et al. 1993). Higher values are reported for heterogeneous surfaces and urban land use classes, e.g. with values around 20-27 for a light industrial site as reported by Voogt and Grimmond (2000). Kato and Yamaguchi (2007) list values for $k\beta^{-1}$ of 7 (industrial, urban, forest), 4.6

(grassland) and 3.9 (lawn, bare soil). Several studies used Eddy Covariance (EC) and/or scintillometry measurements to determine $k\beta^{-1}$ in the footprint of their measured fluxes. z_{0h} may also be calculated from the roughness Reynold's number (e.g. Kanda et al., 2007)

$$z_{0h} = z_{0m}[7.4\ exp(-\alpha Re_*^{0.25})] \qquad (4.5)$$

where α = 1.29 and $Re_*=z_{0m}u_*/\nu$ is the roughness Reynolds number with a kinematic molecular viscosity ν of 1.461 × 10^{-5} ms^{-1}. This z_{0h} value is used in Equation (4.4) for the calculation of aerodynamic resistance r_H.

The Urban Multi-scale Environmental Predictor (UMEP, Lindberg et al., 2018) provides the framework for calculation of the spatial distribution of roughness parameters and derived aerodynamical resistances needed for the calculation of Q_H in Equation (4.1) with the input data listed in Table 3. The zero-plane displacement height z_d is calculated after Kanda et al. (2013), using additional morphological parameters like the plan area index λ_p and the frontal area index λ_f.

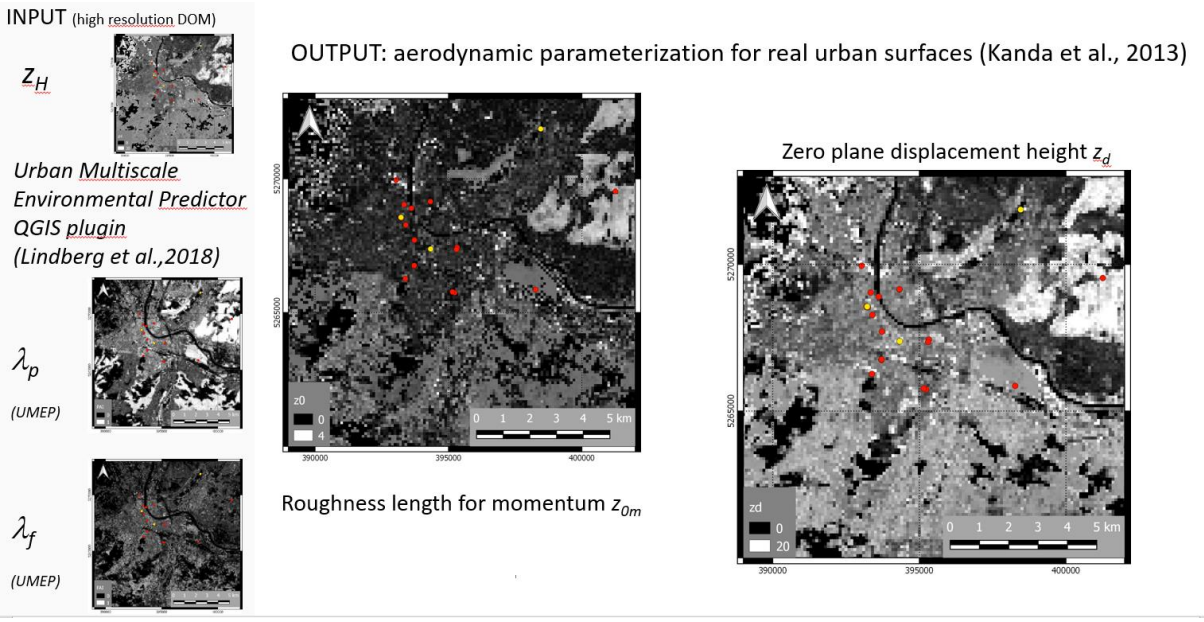

Figure 15. UMEP input (left) and output of roughness parameters for calculation of aerodynamic resistance.

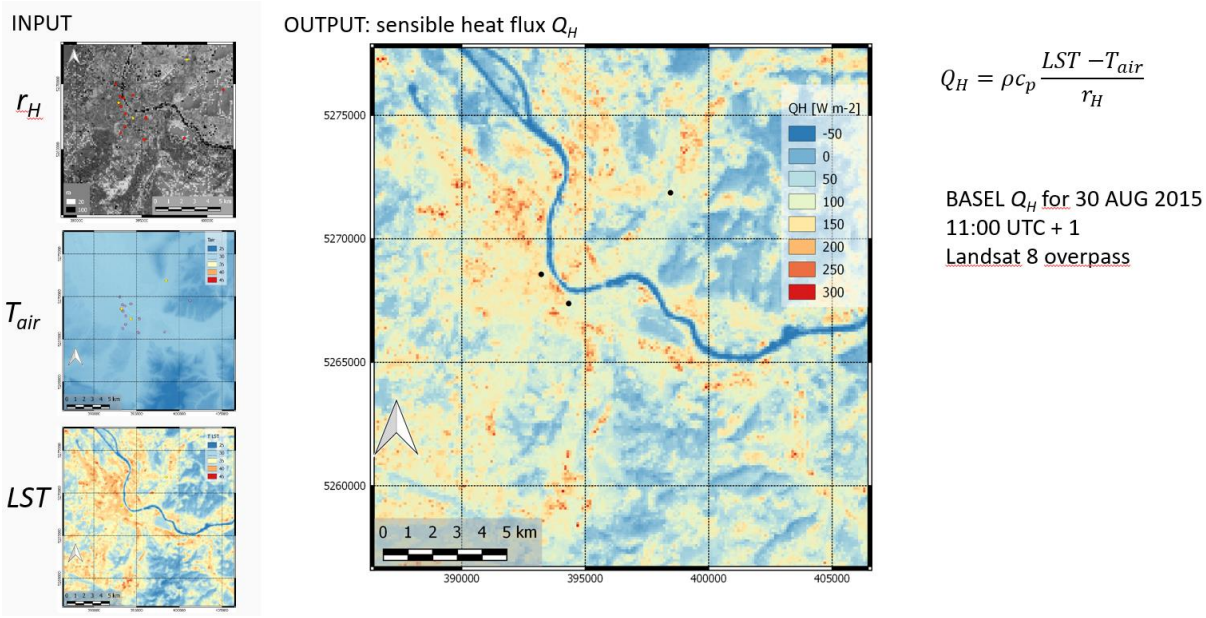

Figure 16. *Final calculation of spatial distribution of Q_H for Basel, Switzerland.*

4.2 Evaluation

4.2.1 Uncertainty, limitations and validation

A comparison of measured sensible heat fluxes with weighted modelled fluxes in the footprint of the flux towers in the frame of the URBANFLUXES project showed that measured Q_H were generally higher for all case study cities. Several reasons may lead to these differences, as discussed in Feigenwinter et al. (2018): The uncertainty inherent to EC measurements for Q_H is in the range of 10% (25% for other trace gases), the representativeness of flux tower measurements in urban environments is reduced compared to rural areas due to the heterogeneity of urban neighbourhoods and there are large (inherent) variations in EC measurements between the averaging intervals which additionally increase the uncertainty for the time of the satellite overpass. There are also known drawbacks of the ARM method: input parameters (T_{air} , friction/wind velocity) have to be spatially derived from in-situ measurements (flux towers and/or sensor networks) and may differ from "true" values in certain areas during satellite overpass; further large uncertainties exist in the calculation of the aerodynamic resistance including $k\beta^{-1}$. Figure 17 shows the deviations between measured and modelled values of QH for two flux tower sites (adapted from the URBANFLUXES project).

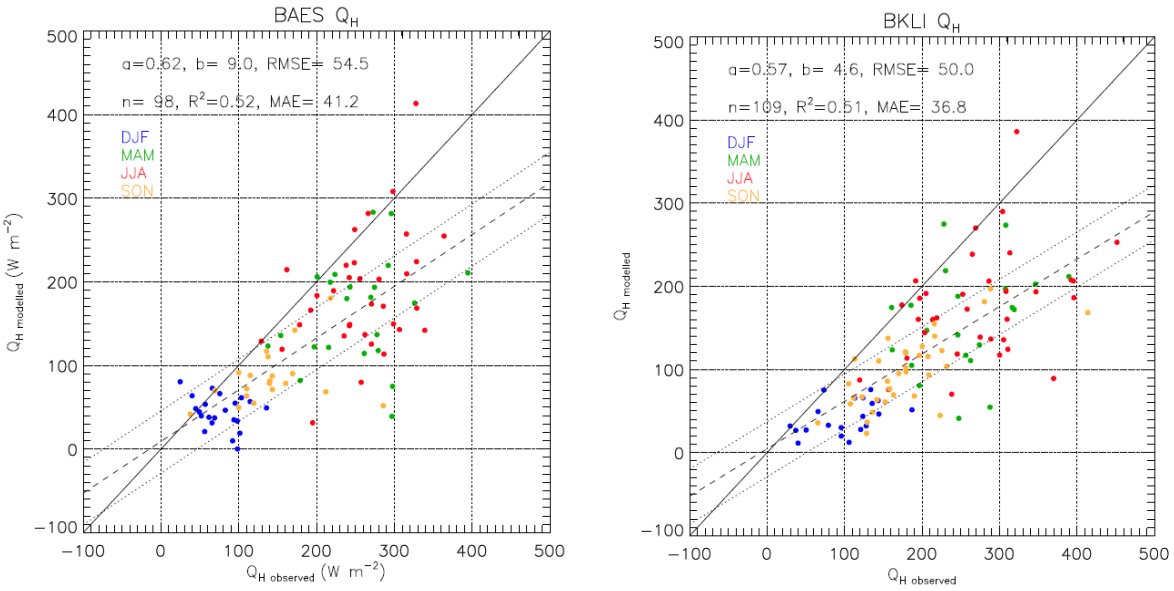

Figure 17. Differences between measured and modelled Q_H for two flux tower sites in Basel, Switzerland.

The same validation procedure was performed for the CURE AP03 results, i.e. the comparison of sensible heat flux QH measured at the flux towers in HERAKLION and BASEL city centers with the modelled sensible heat flux in the respective footprint of the flux tower. Similar results as in the URBANFLUXES project are obtained for CURE and are displayed in Figure 18 and Figure 19.

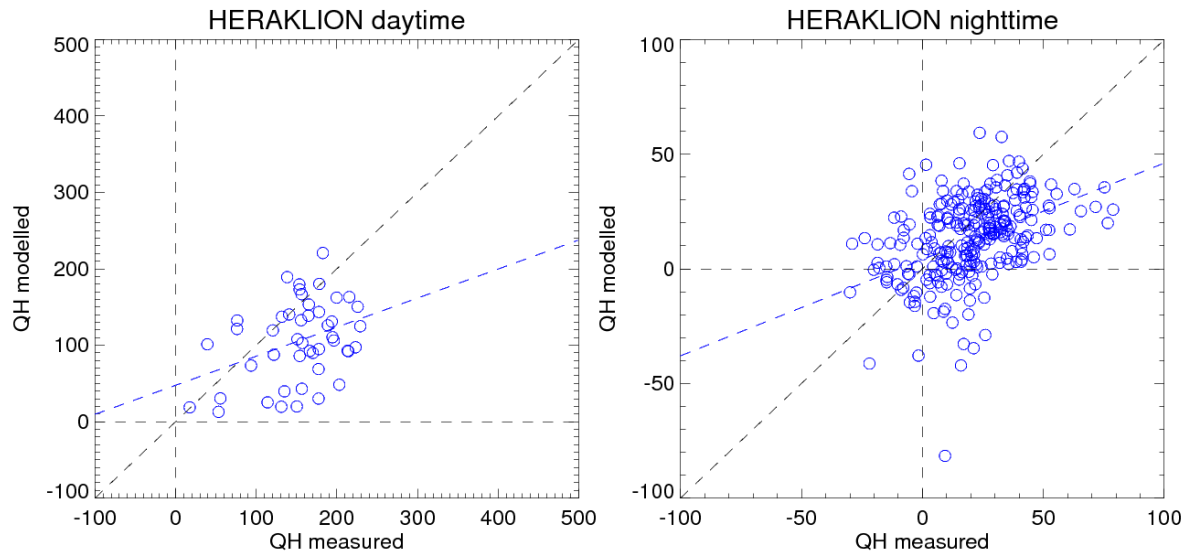

Figure 18. Differences in W m^{-2} between measured and modelled QH for daytime (left) and nighttime(right) in front-runner city HERAKLION. Regression lines are dashed blue. The low number of daytime values is due to missing LST data for the location of the HERAKLION flux tower.

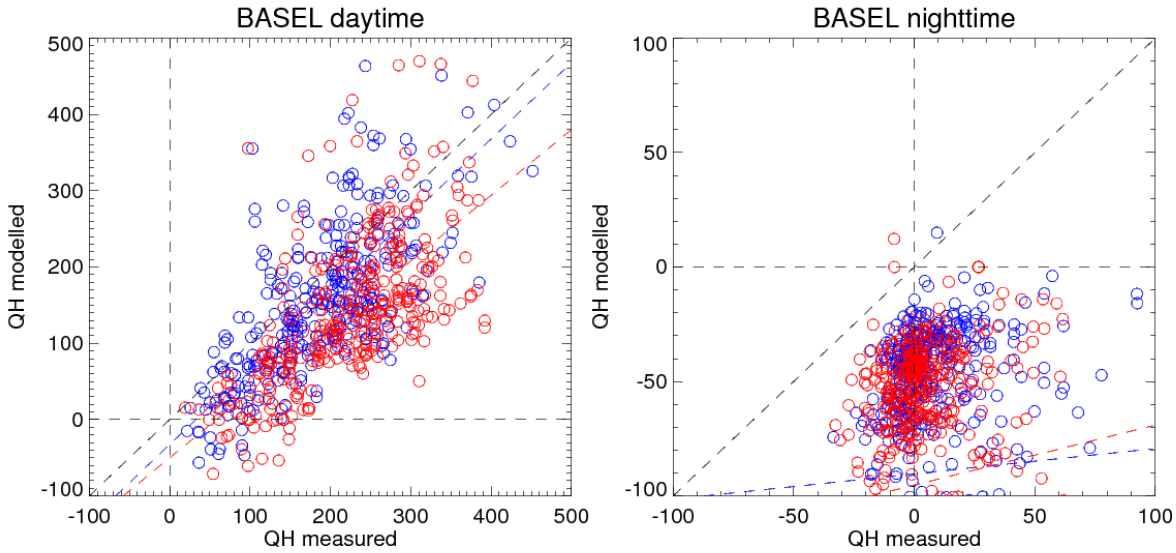

Figure 19. Differences in W m^{-2} between measured and modelled QH for daytime (left) and nighttime(right) in follower city BASEL. Blue and red colors refer to flux towers BAES and BKLI, respectively.

Since the deviations are systematic, we hypothesize that the differences are related to the anthropogenic heat flux, which may not be considered in the ARM method but is measured by the EC system.

4.3 Results

Figure 20 shows a sample result of AP03 for front-runner city Heraklion. A daytime and a nighttime map of sensible heat flux Q_H in W m^{-2} are displayed.

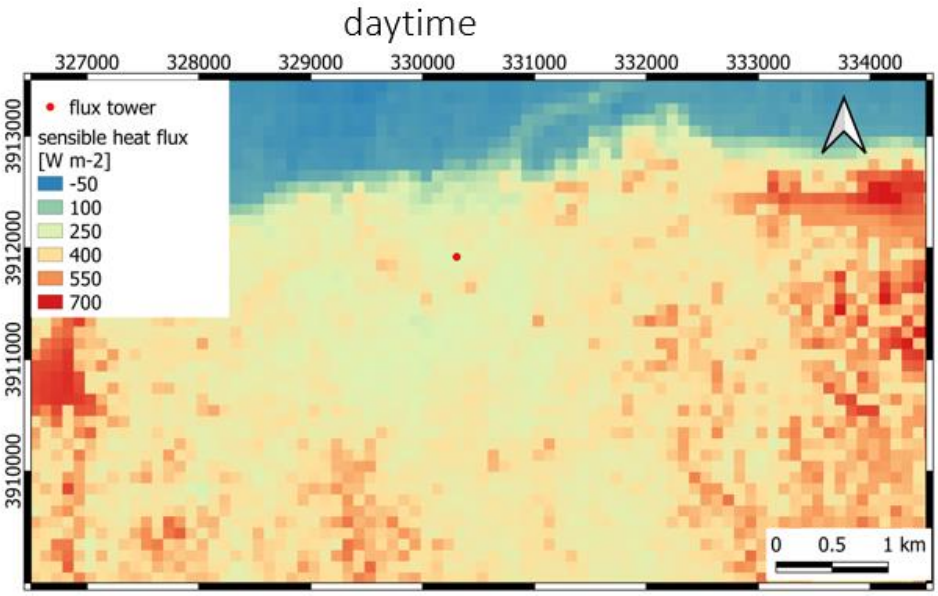

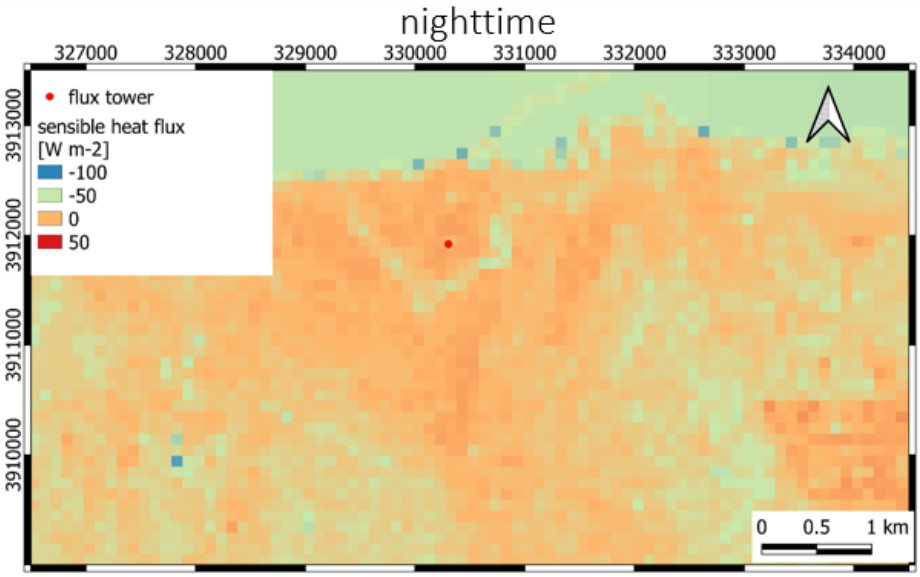

Figure 20. *Example for AP03 product for front-runner city HERAKLION: Spatial distribution of sensible heat flux Q_H for daytime (top) and nighttime (bottom).*

4.4 Application Dockerization

AP03 has been implemented with Python and GDAL. It has been packaged in a Docker image with all the required libraries. The Docker can run AP03 as a standard Python script along with all the parameters needed as input depending on the user inputs (Date range, City of Interest). To run AP03 Docker all inputs data should be placed in a single folder. These include the LST products from AP01 Docker (.tiff files) and C3S ERA5 Reanalysis data (single .grib file). In addition, to get the output product from AP03 Docker there should be an output folder residing in the machine running the Docker. In order for the Docker to be able to receive the input data and deliver the output data, both input and output folders should be mounted with the Docker container where AP03 is running.Following the above instructions an example command for running the Docker should be like this:

```
sudo docker run -v $(pwd)/user_input/:/working_dir/user_input/ -v
$(pwd)/output/:/working_dir/output/ remotesensinglab/ap03-image:latest
python3 py/CURE_AP03_ERA5.py ./
```

Dockerization of AP03 was realized using C3S ERA5 meteorological input data instead of local data (see also Table 3). Input data are listed in Table 5. Some of the required input parameters for AP03 in eqs. (4.1) and (4.2), namely the friction velocity u^* and the Monin-Obukhov length L are not directly available from the Copernicus Service and have to be derived from the wind components and mean surface sensible heat flux, respectively. Friction velocity u_* was derived

from 10m wind components by applying the "rule of thumb" for the relation between friction velocity and horizontal wind speed in urban areas (Oke et al., 2017):

$$u_* = 0.15 * \mathrm{sqrt}(u^2 + v^2), \qquad (4.6)$$

with u and v as the 10 m components of wind from C3S ERA5.

Monin-Obukhov length L was derived by

$$L = -(T_{air} * u_*^3)/(k*g*wt), \qquad (4.7)$$

with T_{air} as the 2 m air Temperature from C3S ERA5, u_* the friction velocity as calculated above, k the von Kármán constant (0.4), g the gravitational acceleration (9.81 m s^{-2}) and wt the kinematic heat flux derived by division of C3S ERA5 'Mean_surface_sensible_heat_flux' by ($\rho_{air} * c_p$), the density of air (1.2 kg m^{-3}) and the specific heat capacity at constant pressure (1005 J kg^{-1} K^{-1}), respectively.

Table 4. *Input data for AP03 Docker (Copernicus).*

Docker input data		Docker output
Input Data C3S ERA5 'reanalysis-era5-single-levels'	Area	
10m_u_component_of_wind	For HERAKLION:	
10m_v_component_of_wind	Lat : 35.28..35.5 °N	
2m_temperature	Lon: 25.04..25.2 °E	**AP03 product "Sensible heat flux" as geotiff for the respective city AOI**
2m_dewpoint temperature	For BASEL:	
Surface_pressure	Lat : 47.45..47.5 °N	
Mean_surface_sensible_heat_flux	Lon: 7.45.. 7.7 °E	
Input from CURE AP01		
Land Surface Temperature LST (for CS input data refer to Table 2)	AOI HERAKLION AOI BASEL	

4.5 Comparison of Copernicus Services input data with local data

The use of input data from Copernicus Services for AP03 dockerization affects the output, since CS ERA5 data are gridded in 0.25° resolution. This means, that the urban influence on the meteorological input parameters (temperature, humidity, wind) is blurred by the large rural part in the pixels. In Figure 21 the scatter plots are shown for 4 relevant input parameters, namely: air temperature, relative humidity (derived from C3S ERA5 dewpoint temperature), wind velocity and mean surface sensible heat flux. Differences between ERA5 data and in-situ measurements are obvious in all four displayed variables, but the impact on the final product has to be analyzed in more detail.

The highest impact is expected from air temperature, where the measured value at the flux tower is in average about 2-4 K higher than the ERA5 value, which is representative for a much larger area including a large part of non-urban land cover. This means that the difference of $LST - T_{air}$ in the nominator of eq. 4.1 is smaller, resulting in smaller Q_H. The impact of the other three parameters on the result is much lower and considered to be negligible: Relative humidity is converted into water vapour pressure and used to calculate air density, wind velocity affects friction velocity u^* (and thus also the amount of Monin-Obukhov length L), and the mean sensible heat flux from ERA5 defines mainly the sign of the stability parameter used in the stability functions of eqs. (4.2) and (4.3).

Nevertheless, the usage of C3S ERA5 data has the advantage of full availability. In situ data is subject to larger periods of missing data due to instrument failure as was the case for the first six months of 2019 in HERAKLION.

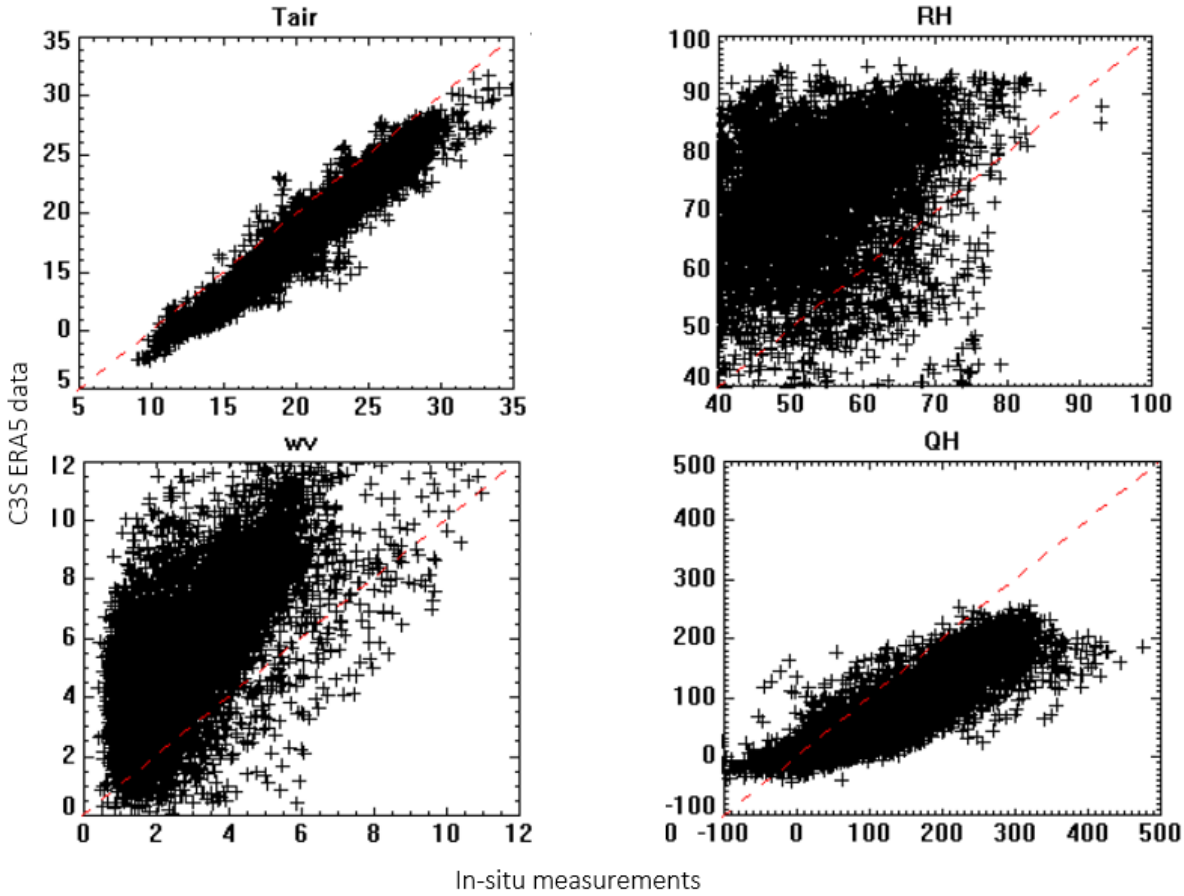

Figure 21. *Comparison of C3S meteorological input data (y-axis) with in-situ measurements (x-axis) for HERAKLION for 2018 (Tair: air temperature, RH: relative humidity, wv: wind velocity, QH: sensible heat flux).*

Figure 22 shows the difference of Q_H between the two options (ERA5 and in-situ) for input data. Depicted is the difference $Q_{HERA5} - Q_{Hin\text{-}situ}$ for the scenes from AUG 18 2018 at 19:36 UTC (nighttime) and from AUG 10 2018 08:27 UTC (daytime). Differences are huge especially for

rural areas during daytime. In order to correct the ERA5 output to deliver reasonable values, the AP03 code would have to be completely rewritten for adaptation to the different input data and the coarse resolution air temperature in detail. In conclusion, we think, that the coarse resolution of C3S ERA5 air temperature is not suited for the application of the ARM and we do not recommend to use C3S ERA5 meteorological data as input for AP03.

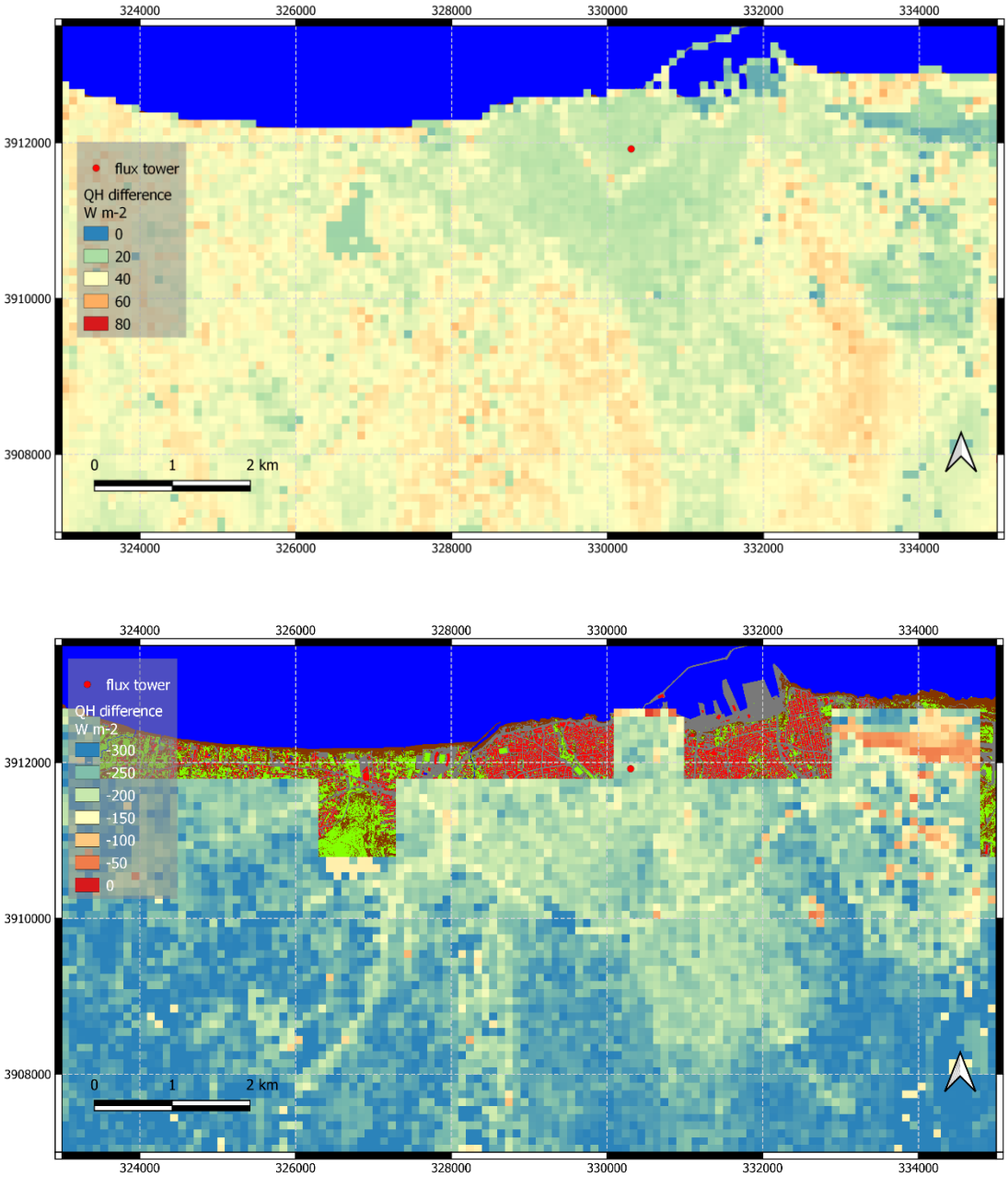

Figure 22. *Comparison of AP03 output using C3S meteorological input data and in-situ measurements. Displayed is the difference Q_H(ERA5) minus Q_H(in-situ). Top: Difference for nighttime AUG 18 2018 at 19:36 UTC. Bottom: Difference for daytime AUG 10 2018 at 08:27 UTC.*

5 AP04 URBAN CO_2 EMISSIONS MONITORING

5.1 Data & Methodology

CURE AP04 will be developed for retrieving CO_2 emissions within city boundaries in neighborhood scale, combining local scale CO_2 flux measurements by Eddy Covariance (Stagakis et al., 2019) with surface parameterization based on source strenghts proxies derived from local data, Sentinel-2, VHR satellite data and CLMS products through the most up-to-date turbulent flux source area model (Kljun et al. 2015). The individual processes contributing to the total CO_2 emissions will be statistically modelled and scaled up according to the associated source strength proxies.

5.1.1 Data

AP04 is based on a mix of local data, products from ESA- and Copernicus data sources and pure Copernicus services. Key data sets are:

- Road network and traffic data
- High resolution digital object model (DOM) of buildings
- Population density
- Seasonal NDVI
- Turbulent fluxes of CO_2: in-situ measurements from urban flux towers equipped with Eddy Covariance systems. The core data set of AP04 to be used for assigning the contributions from the four basic sectors to the total flux.
- Meteorological data: Air temperature, humidity, wind velocity, wind direction, radiation from in-situ measurements. Needed for flux footprint calculation.
- Digital Object Model (DOM): A high resolution (1 m x 1 m) model of buildings and trees is the essential base for calculation of sectorial roughness parameters as input for the flux footprint model.

Table 5 provides an overview of the datasets used in AP04.

Table 5. *Input data for AP04 (local and Copernicus).*

Data	Local	Copernicus service
Land Use/Land Cover map	Available in high resolution for front-runner city Heraklion and follower-city Basel based on VHR satellite data	CLMS urban atlas
DOM	Available in high resolution for front-runner city Heraklion and follower-city Basel (buildings and trees)	CLMS building heights CLMS street tree layer
Road network and traffic data	TomTom traffic statistics product, traffic counts and road network	
Population density Seasonal NDVI		URBAN ATLAS 2012 Sentinel-2
Meteorological data	In-situ measurement network	C3S ERA5 Reanalysis data
Turbulent CO_2 flux F_C	In-situ EC flux tower	
CO_2 concentration and fluxes		CAMS Flux inversion reanalysis of global CO_2
Energy/Fossil fuel consumption	From city authorities, where available	

5.1.1.1 LULC and road network

The concept of LULC map from the former H2020 URBANFLUXES project (Chrysoulakis et al., 2018) is the base for LULC classification used in AP04. This classification is extended with the road network from OSM, because traffic is one of the main sources of CO_2 emissions in general and in the front-runner city Heraklion in detail. Figure 23 shows the LULC classification with road network.

Figure 23. LULC map of the HERAKLION city center extended with OSM network.

Because there are no traffic data available for the front-runner city Heraklion a trial set of the traffic statistics from the TomTom Historical Traffic Services (https://support.move.tomtom.com/ts-introduction/) is used. Figure 23 shows an example of the capabilities of this data set. For each street node, "hits", i.e. the number of vehicles, are available in hourly resolution. Since the road is in the area of the main contribution to the total flux (red and yellow colors of the flux footprint), this dataset is considered as an adequate substitute for automatic permanent traffic count locations.

5.1.1.2 Eddy Covariance flux tower data

CO_2 fluxes from the Heraklion flux tower measured by the Eddy Covariance (EC) method are available from November 2016 to date, with a large gap due to technical problems from November 2018 to July 2019. A detailed description of the EC method in general can be found in Aubinet et al. (2012), while Feigenwinter et al. (2012) refers to the specific issues of EC measurements in urban environments. EC raw data (20 Hz) were processed with the EddyPro® Software version 7 from LI-COR Biosciences resulting in half hourly CO_2 fluxes and numerous diagnostic parameters. A very useful diagnostic parameter is the quality flag calculated after the method of Foken et al. (2004) which provides the flag "0" for high quality fluxes, "1" for intermediate quality fluxes and "2" for poor quality fluxes. This system is suitable for selecting flux results complying with international practices.

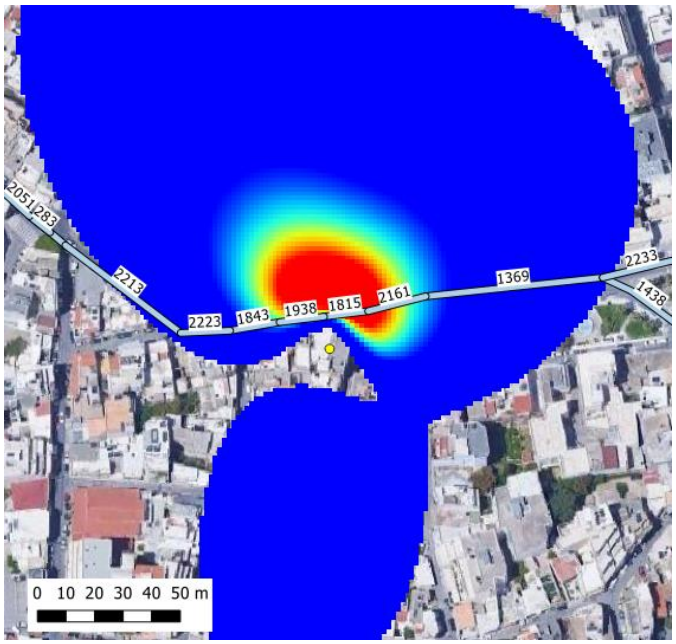

Figure 24. *TomTom road nodes (numbers) with hourly vehicle counts in the footprint of the HERAKLION flux tower (yellow dot). Colors refer to relative contributions to the total flux from high (yellow) to low (blue).*

Figure 25 exemplarily shows the data availability and the data quality of half hourly Heraklion CO_2 fluxes for the months JUL/AUG/SEP 2018. For all further processing only fluxes with flags 0 and 1 are used.

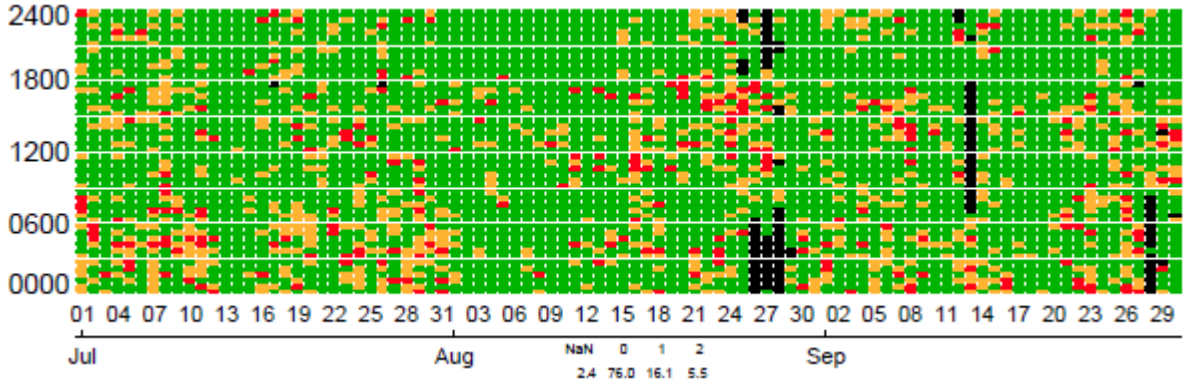

Figure 25. *Data availability for and data quality of HERAKLION CO_2 fluxes for JUL/AUG/SEP. Green, orange and red colors refer to quality flags 0,1,2 (high, intermediate, poor), respectively. Black colors refer to "no data".*

5.1.2 Methodology

The approach for estimating within urban boundaries' CO_2 emissions (excluding industrial processes) is based on statistical modelling of four basic source and sink processes in the urban environment, according to the following equation:

$$CO_2(x,y) = c_{traffic} * SS_{traffic} + c_{build} * SS_{build} + c_{popdense} * SS_{popdense} + c_{veg} * SS_{veg} \quad (4.5)$$

where subscripts *traffic*, *build*, *popdense* and *veg* represent the contributions to the total CO_2 emission at point x,y from the transport sector, building sector, human metabolism and vegetation, respectively. SS stands for source strengths. Table 6 provides an overview of the proxy datasets used in eq (4.5).

Table 6. *List of proxy data sets for emission sectors*

Emission Sector	Data	Source
Transport	Vehicle counts	Local, TomTom statistics
Buildings	Building volume	Local, Copernicus Urban Atlas
Human metabolism	Population density	Copernicus Urban Atlas
Vegetation	Tree volume, NDVI	Local, Copernicus Sentinel

Coefficients *c* in eq (4.5) are determined in an iterative way by comparing with local scale contributions from the respective emission sector in the source area of the CO_2 flux measurements by Eddy Covariance. The turbulent flux source area model (Kljun et al., 2015) is applied and parameterized based on detailed urban morphology indicators. Air temperature derived heating degree days will be auxiliary parameters for emissions from the building sector where relevant. Emission estimates from human metabolism are based on spatially aggregated population statistics (Christen et al., 2011). Since the vegetation fraction in the footprint of the Heraklion flux tower is very small, the biogenic contribution in the area of interest is modelled by an empirical approach based on seasonal NDVI (Del Grosso et al., 2018). Individual emission sector contributions are scaled up to city-wide maps and synthesized to net CO_2 emission products. Figure 26 shows the general concept of AP04 methodology.

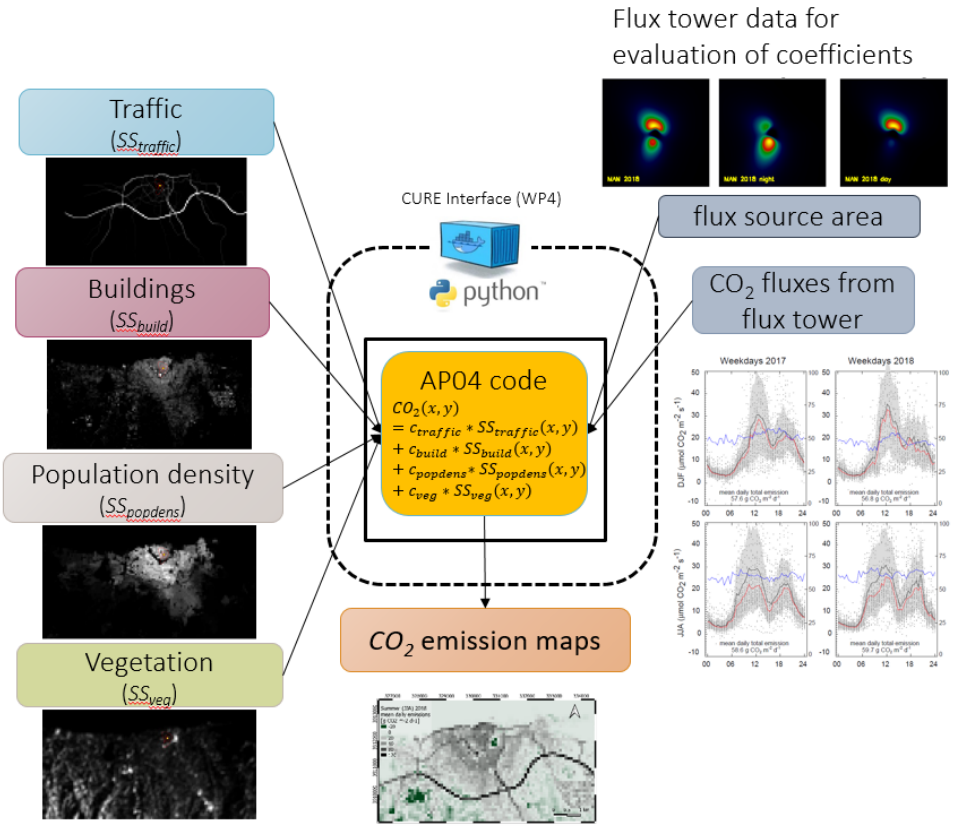

Figure 26. General concept scheme of AP04 methodology

5.1.2.1 Mean seasonal diurnal and hourly fluxes and footprint calculation

For the final AP04 product we propose an approach based on seasonal mean diurnal fluxes and the corresponding averaged footprints, i.e. the footprint climatology. Figure 27 shows the mean diurnal course of CO_2 fluxes for the meteorological seasons winter (DJF), spring (MAM), summer (JJA) and autumn (SON) for the years 2017 to 2020. The bi-modal shape indicates that traffic (rush hours) are the main driver of CO_2 emissions in the footprint of the HERAKLION flux tower. It is therefore important to have detailed information about traffic in order to correlate the CO_2 fluxes with traffic frequencies. From Figure 27 it is also obvious, that heating in the winter plays a minor role since no increase of the mean daily total emission is observed. On the other hand, also no significant signal from vegetation is observed, because this would exhibit lower emissions due to photosynthesis in the vegetation period. Mean half hourly footprints are calculated by averaging the available footprints for each half hour in a similar way (not shown). The mean diurnal courses of CO_2 fluxes and the average footprints were used for further processing as described in the previous section.

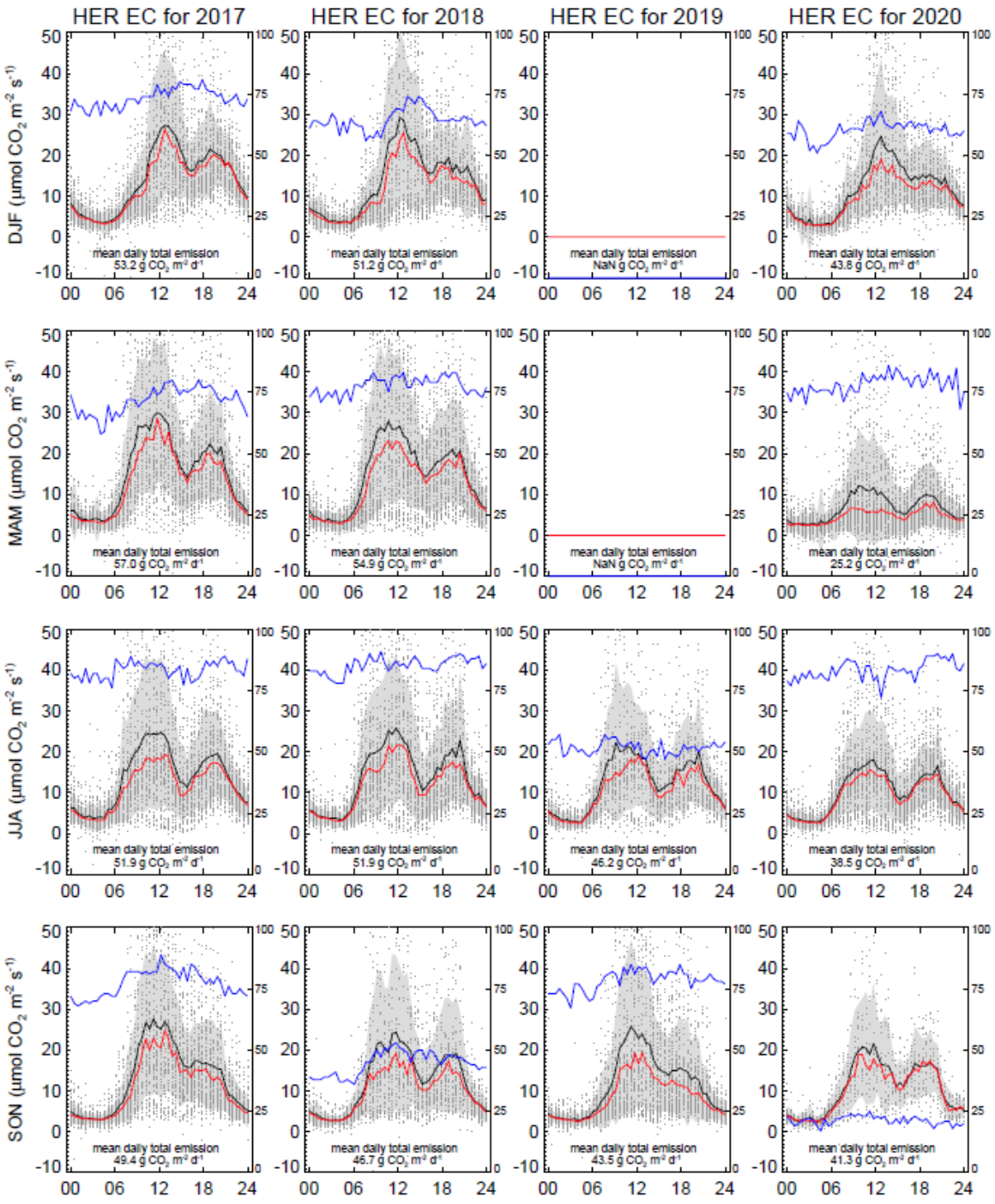

Figure 27. *Mean diurnal course of F_C for all seasons (top to bottom) and years 2017 to 2020 (left to right) with mean daily total emissions. Arithmetic mean (black), median (red), standard deviation (gray shaded) and single half hourly values (dots). The blue curve refers to the number of measurements used for averaging and scales with the right y-axis (max. number of measurements is around 90 days for a season).*

5.2 Results

Figure 28 shows a sample result of AP04 for front-runner city Heraklion. Mean daily total CO_2 emissions in g CO_2 m^{-2} d^{-1} are displayed for workdays in spring season (MAM) 2019.

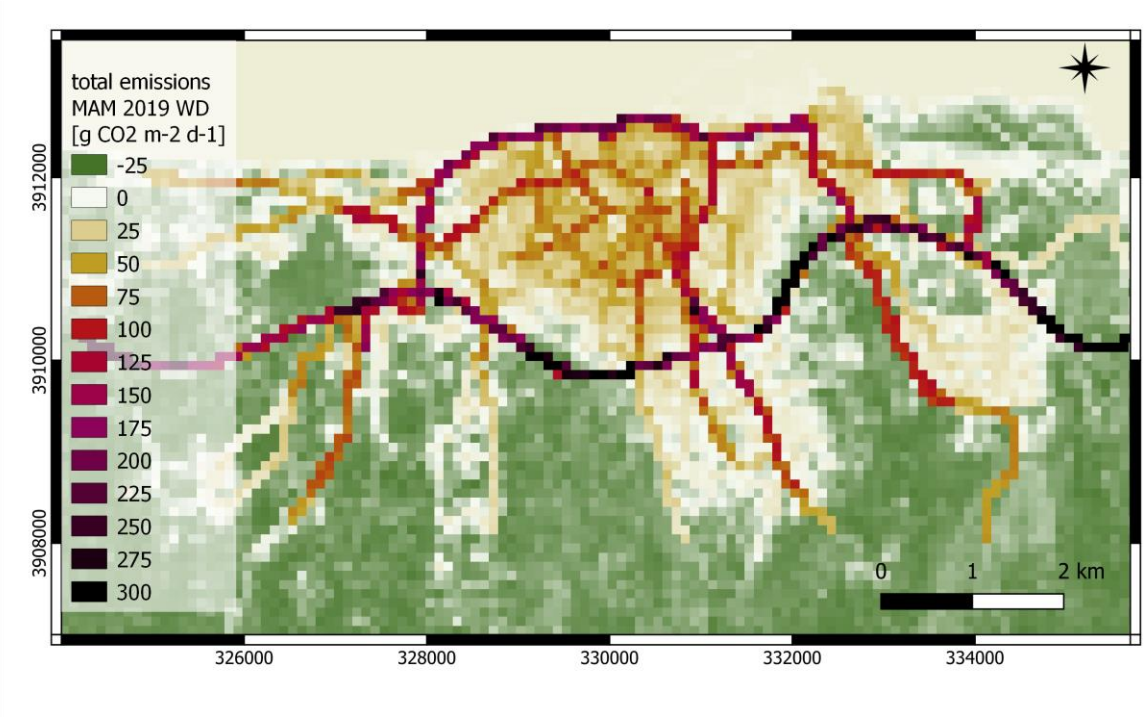

Figure 28. *Example for AP04 product for front-runner city HERAKLION: Spatial distribution of mean daily CO_2 emissions for workdays during spring season 2019 (months March, April, May). Highest emissions are linked to traffic (road network) and densely built-up areas (buildings, human metabolism). Vegetated areas act as a sink for CO_2 during the vegetation period.*

Maps are produced for mean diurnal emissions for all seasons in 2018 and 2019 for weekends and workdays and emission sources *total, traffic, buildings, population and vegetation*, respectively. Table 7 provides an overview for all available AP04 products. Additionally, hourly maps for emission sources *traffic* and *vegetation* are also available. These hourly maps are combined into an animation in order to highlight the pronounced diurnal courses of these two sources, i.e. the two peaks of the morning and evening rush hour (for *traffic,* as shown in Figure 28Figure 30) and the characteristic source/sink (night/day) behavior of vegetation. The other sources (*buildings* and *population*) show only very small diurnal variations. Seasonal variations are most pronounced in emissions from *buildings* due to heating and in *vegetation* due to seasonal vegetation dynamics. As example the *buildings* emissions for winter and summer 2018 for the follower-city BASEL are shown in Figure 29. Note that HERAKLION does not show such pronounced seasonal differences in *buildings* emissions because of its favorable mild winter climate conditions.

Table 7. *List of available AP04 products*

city	year	seasons	sources	weekdays	Hour
HERAKLION	2018	winter	total	working days	full day
BASEL	2019	spring	traffic	weekend	01:00
		summer	buildings		…
		autumn	population		23:00
			vegetation		24:00

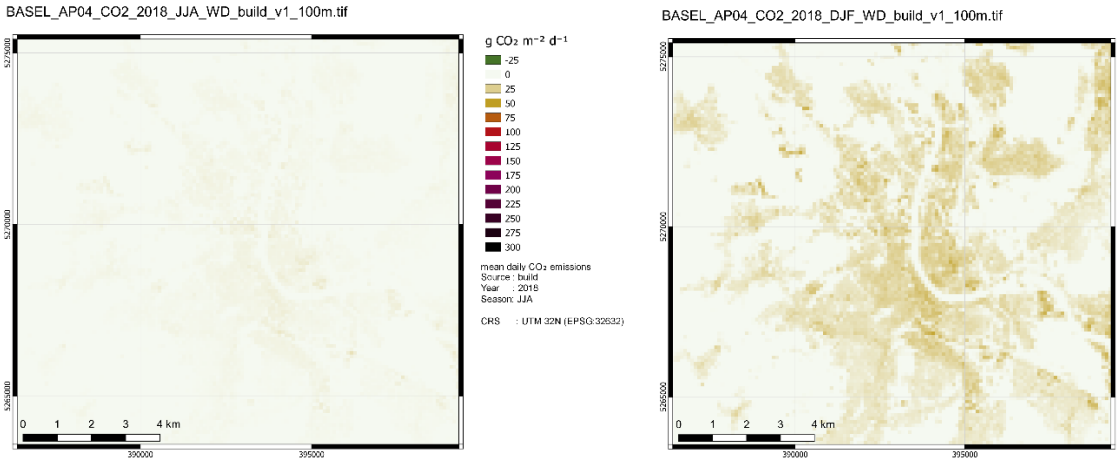

Figure 29*. Example for AP04 product for follower city BASEL highlighting the seasonal (winter/summer) differences in mean diurnal CO_2 emission from buildings with winter on the left and summer on the right side.*

For a comprehensive overview of AP04 products and applications refer to the CURE system storylines implemented in WP4.

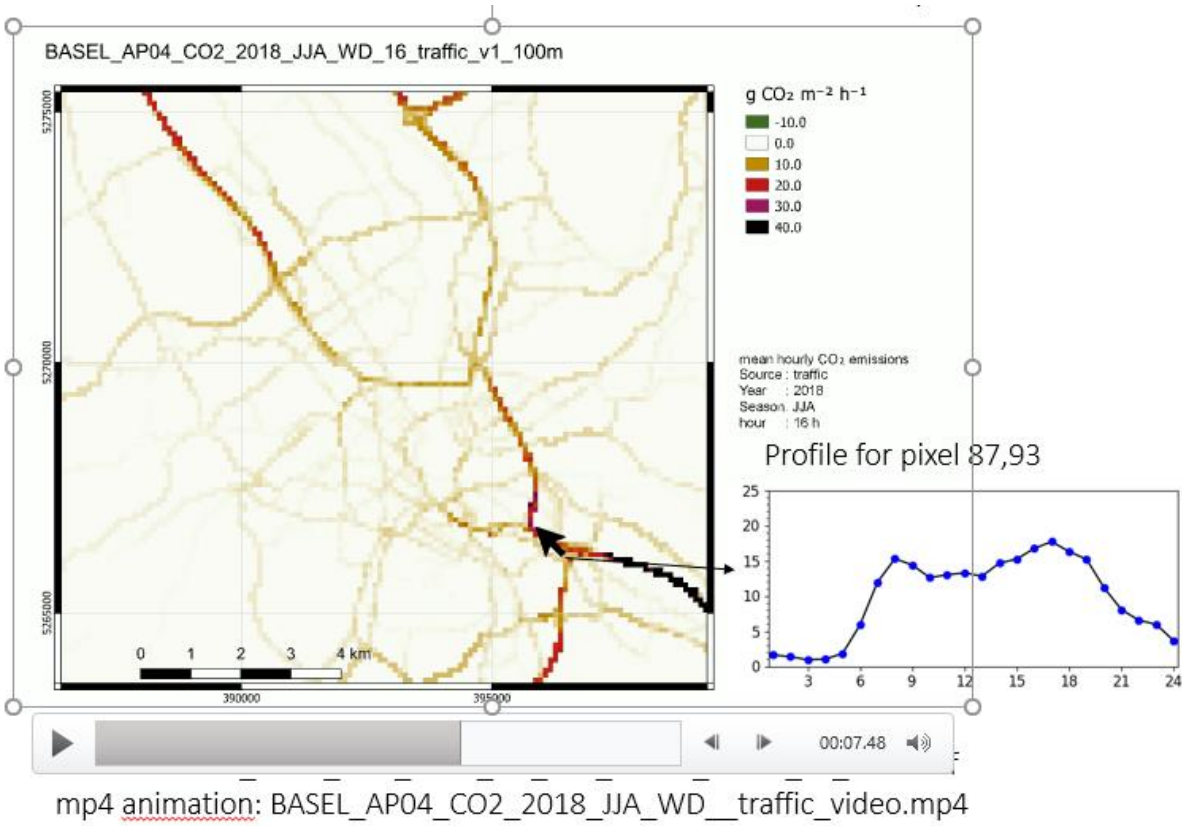

Figure 30. *Example for AP04 product for follower city BASEL: CURE system storyline screenshot at 16:00 of animation for mean hourly CO_2 emissions from traffic for workdays in summer season 2018.*

5.3 Evaluation

An evaluation of AP04 results with Copernicus data was not possible because the resolution of the Copernicus CAMS-surface CO_2-fluxes (biogenic, ocean, fossil) products is far too coarse compared with the Area of Interest (AOI) of AP04, as shown in Figure 31. Due to the lack of alternative CO_2 emission data, we therefore compared modelled CO_2 emissions in the source area of the flux tower with measured CO_2 emission at the flux towers. The results are shown in Figure 32 for the two flux towers BKLI and BAES in BASEL and the flux tower HEKOR in Heraklion.

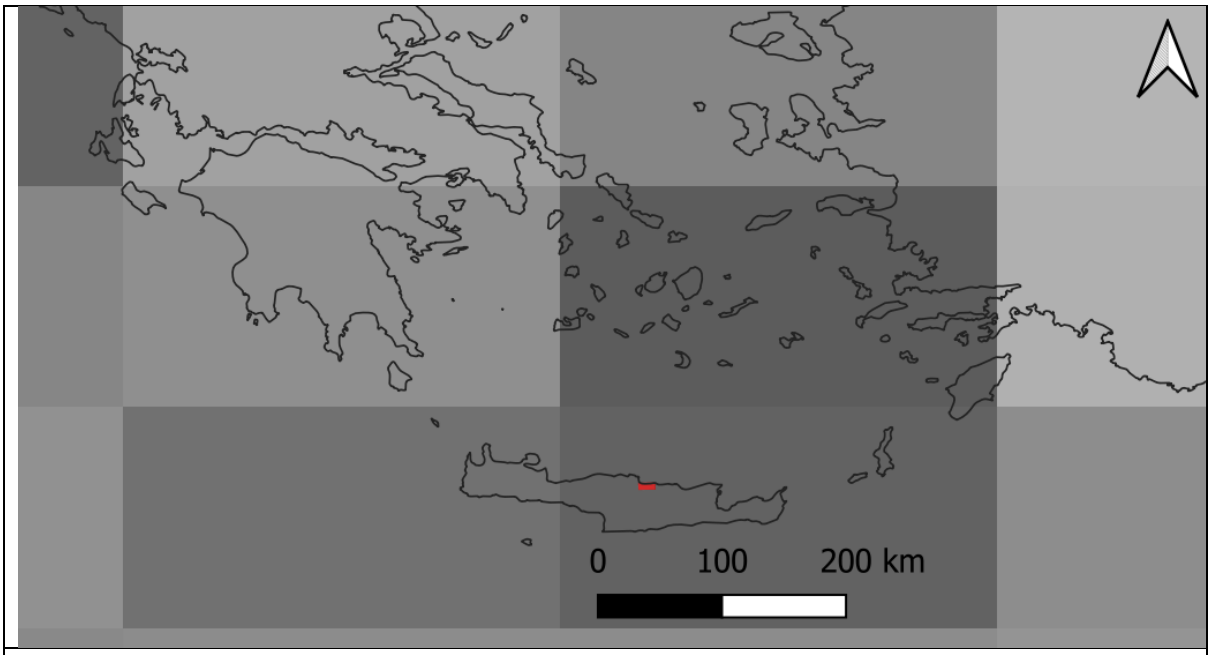

Figure 31. *AOI for HERAKLION (red) compared to the pixel size of CAMS-surface CO_2-fluxes (biogenic, ocean, fossil) products (gray).*

5.4 Application Dockerization

Does not apply, because AP04 in the current development stage provides only static maps. For a dynamic creation of the maps, updated traffic data is a requirement. This is currently not provided by Copernicus services.

Figure 32. *Comparison of modelled CO_2 emissions ("map") with flux tower data ("tower") for BASEL flux towers BKLI (top) and BAES (center) and HERAKLION flux tower HEKOR (bottom). Displayed are mean diurnal CO_2 emissions in g CO_2 m^{-2} d^{-1} for workdays (WD), weekends (WE) and all days for seasons DJF, MAM, JJA and SON, and the whole year, respectively.*

6 AP05 URBAN FLOOD RISK

6.1 Data & Methodology

The method is based on **combination of information about flood risk** depending on local terrain and hydrological characteristics and information about **spatial pattern**, **internal structure and temporal evolution of urban areas** and also about **distribution of population** in those areas.

The app adopts a **"scenario modelling" approach** – i.e. scenarios representing different intensities of flood events are modelled and compared as well as (potential) damage on urban assets and people in the cities caused by these events. This is done based on reference information about flood events in the past and simulations of estimated intensities of expected floods in the future also in relation with different potential climate change scenarios.

6.1.1 Data

The main type of input data for this app is represented by Copernicus Core Services datasets. This secures high replicability (scalability) potential of the service. The modelling method is using the EU-DEM and EU-Hydro River Network database as main data inputs. Additionally, other Copernicus datasets can be used to improve the estimation of flood event intensity as well as of expected frequency of such events in the future.

Table 8. *Input data for AP05 Urban Flood Risk*

CCS	Dataset	Information on
CLMS	EU-DEM	Terrain characteristics/geomorphology
CLMS	European Image Mosaic - High Resolution	Reference information about land surface characteristics in very high resolution
CLMS	Urban Atlas	Distribution, typology and change of the urban land use units
CLMS	EU-Hydro - River Network Database	River network
C3S	E-OBS daily gridded meteorological data for Europe from 1950 to present derived from in-situ observations	Reference information about extreme rainfall events in the past
EMS	Flash flood indicators	Hydrological predictions/scenarios
EMS	Real-time river discharge forecasts	Hydrological predictions/scenarios
EMS	River discharge thresholds	Hydrological predictions/scenarios
EMS	Flood forecasts	Hydrological predictions/scenarios
EMS	River discharge reforecasts	Hydrological predictions/scenarios

These datasets are supplemented by the Copernicus Urban Atlas layer and the World Surface Footprint Evolution (WSF-E) layer in order to obtain detailed information about the structure and development of urban land units .

These datasets are integrated with local city information, or replaced by more precise local data where available and requested by the user. This may include following types of local city data/information:

- Detailed river geometry in vector format
- Detailed terrain model (DTM)/ Digital Surface Model (DSM) e.g. 0,4m DSM/DTM
- Local meteo and hydrological data (river network, runoff, discharge data, sea level)
- Reference data (information) on previous flood events – frequency, extent, inundation depth, incl. corresponding intensity of precipitation, damage on buildings, infrastructure, agricultural land etc.
- Geomorphology/Geology/Infiltration properties of local terrain/landscape
- City plans/urban planning maps - location of buildings, infrastructure, flood-vulnerable units etc.

Also, the local city dataset about the flood events in the past are used as reference information to evaluate the quality of modelling results or to calibrate these results.

6.1.2 Methodology

6.1.2.1 Information about flood hazard

First part of the method is dedicated to obtaining information about flood itself. Information about flood hazard is achieved by combination of various means:

- reference information about flood inundation extent and frequency from historical EO data or other local sources
- geomorphic analysis using DEM/DSM for estimation of flood susceptibility and modelling inundation extent and depth using runoff and discharge patterns, morphology and land cover.

For the first type of analysis, the historical Earth Observation (EO) data serve as the input, in particular dataset from Copernicus programme (DWH). This not only allows for evaluation of the extent and impact of past flood events, but also the Near Real Time (NRT) imageries from Copernicus service will help to include a service with a “rapid response” character, serving for monitoring and evaluation of potential ongoing flood events.

Second, the geomorphic analysis approach (the HAND - high-above-nearest-drainage approach was applied) leading to quantification of flood susceptibility using in particular the digital surface model in combination with the river network data, and information about basic

hydrological characteristics of that area – in particular quantification of runoff representing different precipitation intensities.

These can be supplemented by more advanced types of analysis will be based on sophisticated hydrologic and hydro-dynamic modelling approaches leading not only to modelling inundation extent and depth using runoff and discharge patterns, morphology and land cover, but also other advanced hydro-dynamic analysis, e.g. to compute water surface profiles for steady and unsteady flow models. For this type of analysis, the already existing hydro-dynamic modelling SWs can be exploited. At this moment, HEC-RAS [1] /GeoHECRAS [2], Telemac 2D [3] and Flo-2D[4] can be used for this purpose.

As a result of this first part of the analysis, raster maps representing flood susceptibility, frequency or flood extent and inundation depth for different flooding scenarios are generated, which can either be used on their own or combined with datasets describing urban areas in the next step, to obtain meaningful information about flood risk exposure of urban units.

The app is able to generate results for different flooding scenarios, corresponding with different intensities of rainfall, which can then be compared by the user. The user can modify this parameter to generate flood masks for his own scenarios.

6.1.2.2 Urban flood risk exposure evaluation and modelling

In this second step, the information about (potential) flood intensity is combined with information about the land use, in particular about distribution, typology and changes of urban areas. Maps of flood susceptibility or frequency and estimations of inundation extent and depth for different flood intensities in the future are integrated with the Copernicus Urban Atlas layer (can be supplemented or replaced by local land use maps if requested by the user) to get information about flood hazard to urban assets. Zonal statistics are applied to evaluate flood risk level for each particular land use block from the Urban Atlas. This is combined with the classification of the Urban Atlas block, to derive information about typology of the endangered urban units (residential, commercial, transportation etc. units). Moreover, data on temporal evolution of urban areas (from Urban Atlas or WSF-Evolution layer) are combined with those about flood risk in order to gather (early-warning) information about new constructions in flood-prone areas.

6.1.2.3 Universal character of the application

The app is implemented in maximally universal and automated manner, maximally exploiting the Copernicus data which are harmonized for all (larger) European cities. Thanks to this, the application is easily replicable for most of the European cities (there could be some specificities

[1] https://www.hec.usace.army.mil/software/hec-ras/
[2] https://www.civilgeo.com/products/geo-hec-ras/
[3] http://www.opentelemac.org/index.php/presentation?id=17
[4] https://flo-2d.com/

which may limit replicability potential for some of the European cities, like specific terrain characteristics etc.) Second, the main added value of the application consists of combination of the hydrological modelling (dealing with terrain morphology, river network characteristics, intensity of precipitation) with the (harmonized, for all European cities) information about spatial distribution (incl. typology as by distinguished in Copernicus Urban Atlas) and temporal evolution (UA and WSF-Evolution) of urban units.

General statistics (e.g. area of residential/commercial units endangered by flood risk per city) can be calculated and compared for different cities. However, taking into consideration sensitive character of such information, it should be carefully assessed which information will be presented and how it will be published (the access to such information may be restricted to several users, recruited either from administrations of particular cities for which the modelling is performed, or from European institutions). Same is fact is valid for the AP06 dedicated to urban land movements monitoring.

6.1.2.4 Link between flood risk (AP05) and land subsidence (AP06)

For effective urban planning, the integrated approach is crucial. Therefore, also for the CURE project, it is important to combine information acquired by means of different applications in a meaningful way. Moreover, in case of two applications to be developed by GISAT (AP05 and 06), there can be direct link between these two types of natural hazards. The urban (or sub-urban) land subsidence can occur or intensify as a consequence of previous urban flood. On the other hand, the flood risk to particular areas in the city can increase in time, in case a land subsidence process is present at that spot.

Therefore, we are combining information acquired from the AP05 and 06, to enable the end-users to follow potential link (consequences) between floods and terrain subsidence. This integration can be done in following ways:

- First, for each land use block of Copernicus Urban Atlas layer, information about both subsidence and flood risk exposure is evaluated and presented.
- Second, we plan is still to visualise the results of these two apps in the same interactive web-based map application, so the user can easily follow and evaluate potential links between these two types of hazards.

6.2 Results

The first result generated by AP05 is a raster map showing a distribution and levels of flood hazard over the AOI. The hazard is estimated using the HAND-index based approach (high above nearest drainage), where the level of hazard depends mostly on distance to nearest drainage and local terrain properties. Example of results for the front runner city of Heraklion is presented in Figure 33 below. The approach is parameterizable so the result can be adjusted depending on expected intensity of rainfall event and resulting flood as well as on specific conditions in local area.

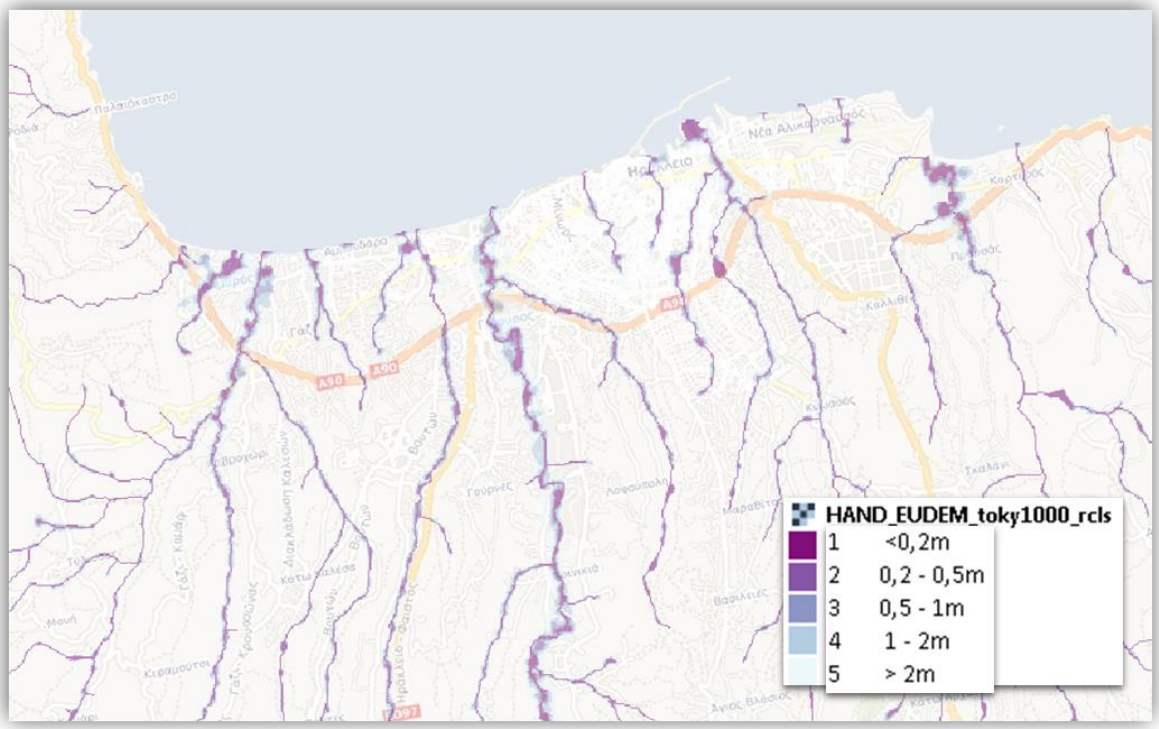

Figure 33. *Example for AP05 basic product for front-runner city Heraklion. Distribution of areas endangered by flood hazard, classified based on level of this hazard from highest to lowest (but still present).*

Based on the above presented basic product of the AP05, the flood hazard is than estimated for urban assets. These may be represented by building blocks or even particular buildings, which are the use cases prepared in the frame of this project, however, they may be represented by any type of object in general, which may be endangered by flood hazard. This hazard to urban assets is evaluated simply by overlaying the above presented raster layer of flood hazard distribution with delineation of the urban assets of interest. Then, the level of flood hazard is quantified for each analytical unit (urban block from Urban Atlas or single building). Examples of such analysis for front-runner city of Heraklion are provided in the figures below.

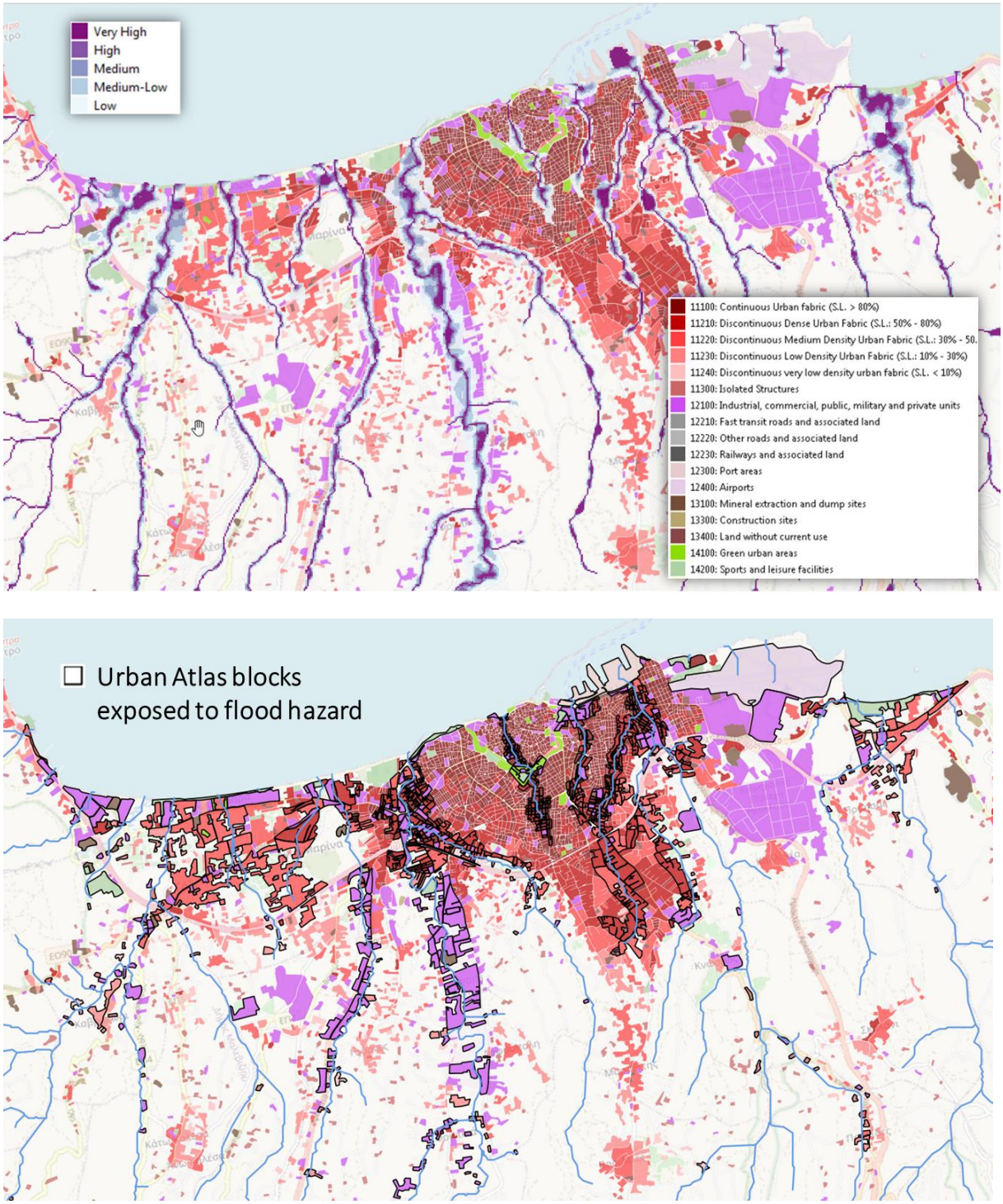

Figure 34. Evaluation of flood hazard for Urban Atlas functional blocks – example Heraklion city.

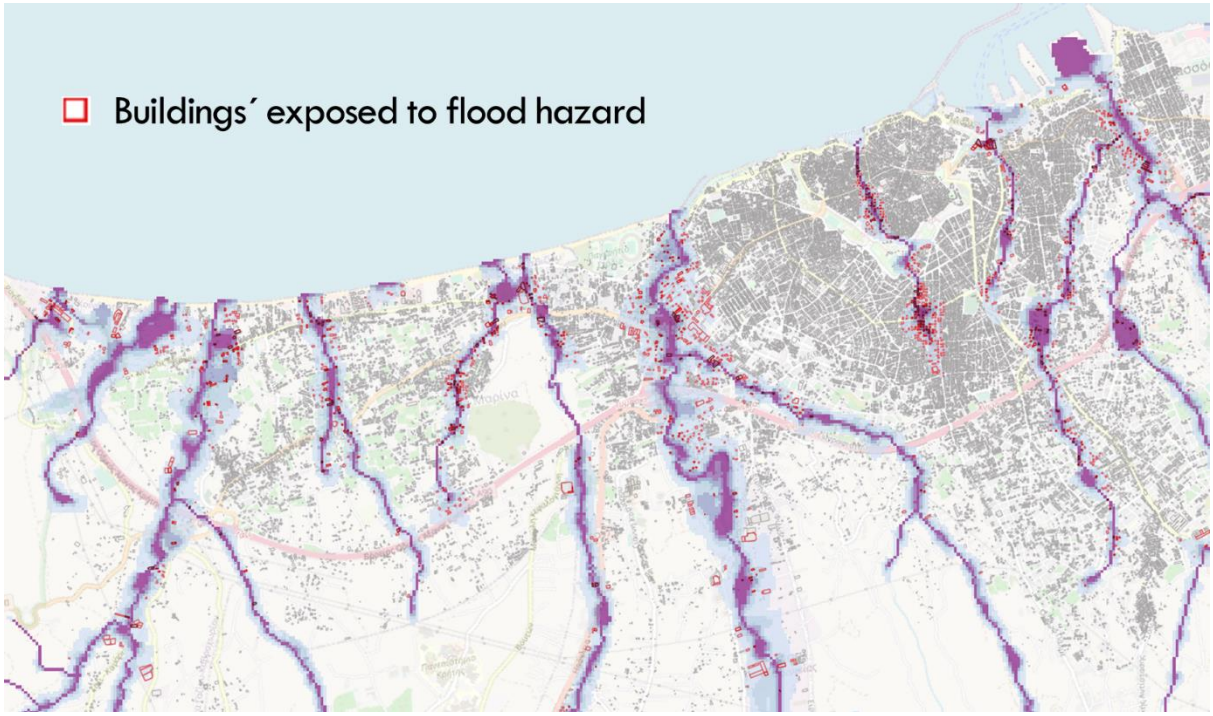

Figure 35. *Evaluation of flood hazard for buildings – example Heraklion city.*

In the next step, we focused on assessment of vulnerability of buildings exposed to flood hazard. There could be many additional criteria helping to evaluate vulnerability of each building exposed to flood hazard, as the age of building, high of building, construction material, type of building use etc. Consideration of all these aspects can help to evaluate the vulnerability of the building exposed to flood hazard. Moreover, an estimation of maximum cost in case of flood event can be made at the city level or in any given sub-city area. Example of such analysis, calculating the numbers, area and volume of buildings endangered by flood hazard in the city in total and by land use type of those buildings (information gathered from Urban Atlas) is illustrated in Figure 36 below. To make more accurate analysis, more detailed and precise local data about buildings´ characteristics would be needed.

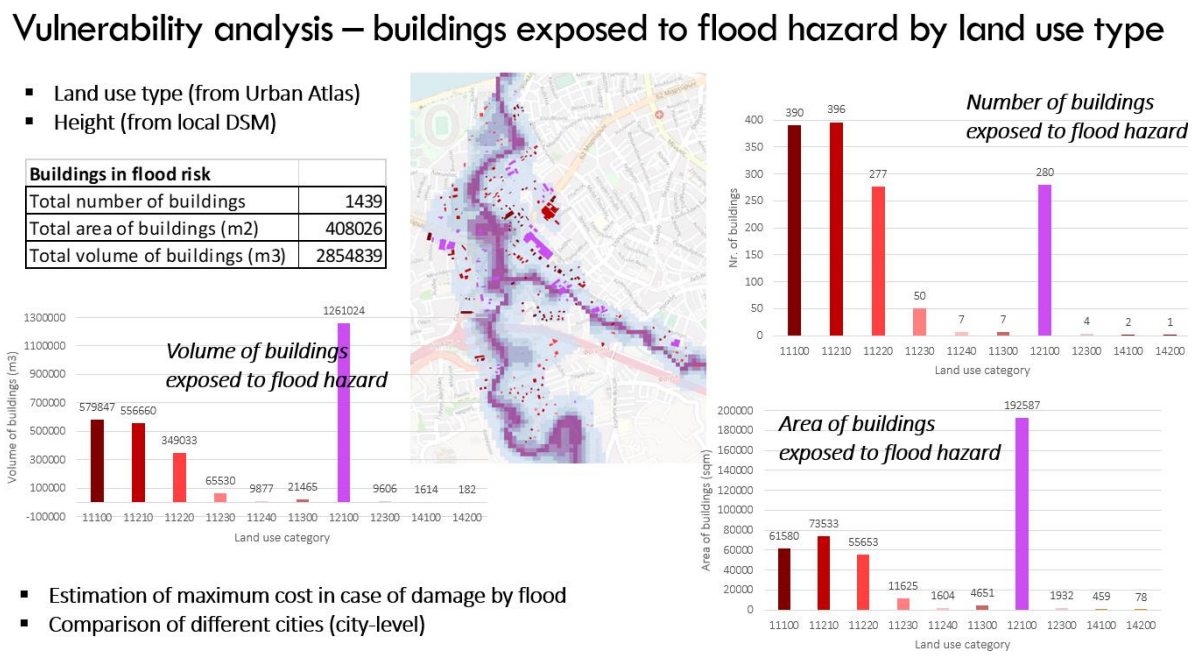

Figure 36. Simple vulnerability analysis – exposure of buildings to flood hazard, by land use type of the building block – example Heraklion city.

For the Ostrava city-region, representing the follower user of the AP05 Flood risk monitoring service, the same type of analysis has been prepared, including statistical evaluation. Again, the results of this flood hazard assessment were combined with the results of AP06 Subsidence monitoring service for the same area. Figure 37 shows an example of such advanced analysis assessing both types of natural hazards.

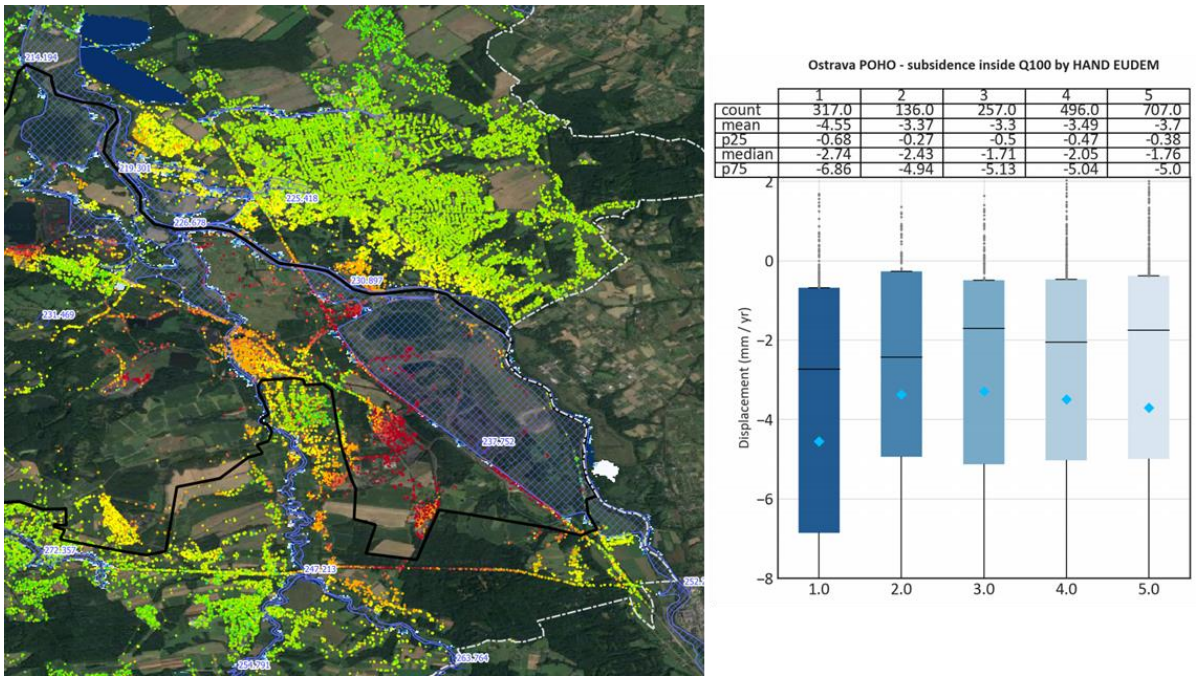

Figure 37. Example of flood hazard assessment in Ostrava city region combined with information about subsidence hazard (AP06). In this case, the statistical evaluation shows highest level of subsidence in zones which are most endangered by flood hazard.

In addition to this type of the analysis, dealing with flood hazard estimation by modelling based on Copernicus data (DEM, river network, Urban Atlas etc.), we also made an assessment of potentially visible consequences of a flash flood event which occurred in Heraklion area in October 2020. This assessment was based on visual interpretation and comparison of pre- and post-flood VHR imageries (obtained from DWH). This analysis and its results are described in detail in the D3.8.

Figure 38. *Assessment of consequences of a flash flood event in Heraklion area, based on comparison of pre-post- flood VHR imageries from DWH.*

6.3 Evaluation

An evaluation of AP05 results with local reference data was not possible only partially. As discussed above, the CURE AP05 results has two parts (i) flood delineation by HAND index and (ii) calculation of flood risk for buildings and urban blocks.

AP05 results were evaluated for the case of Heraklion, Greece, where historical records about flood incidents are available. A total of 20 historical flood records were found for the AOI in which the flood delineation was calculated. In 12 cases, they fall within the calculated flood extent, in 8 ones, they lie outside this extent. Flood extent based on HAND index calculation therefore covers 60% of localities that were affected by floods in the past and for which there is a record.

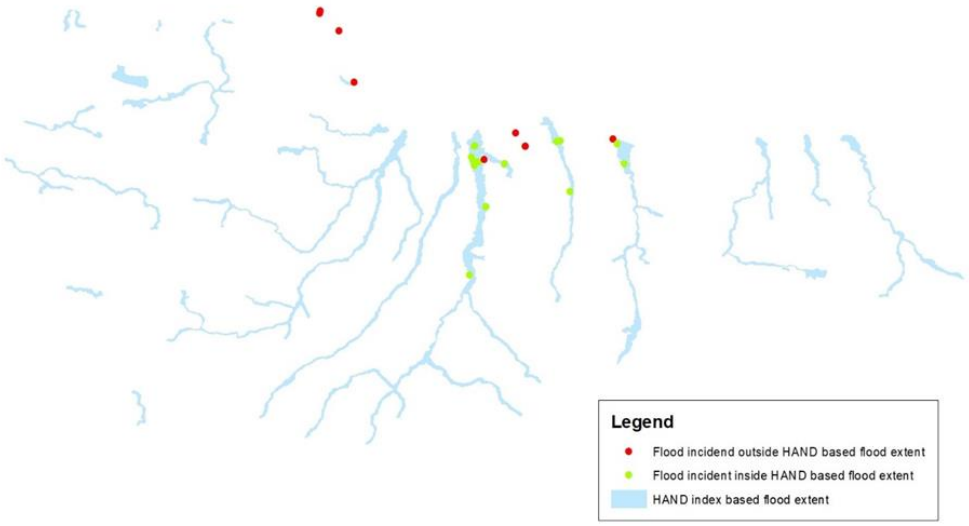

Figure 39. *Example of flood hazard assessment in Heraklion compared with local data.*

The results are shown in Figure 39 for Heraklion. The flood risk calculation for buildings and urban blocks is new in this area and there were no existing products which would provide comparable values available to our knowledge.

6.4 Application Dockerization

AP05 has been implemented with Python and GDAL. It has been packaged in a Docker image with all the required libraries including GRASS GIS libraries (https://grass.osgeo.org). The Docker can run AP05 as a standard Python script along with all the parameters needed as input depending on the user inputs. Processing can be coupled with AP06 docker into multi-criteria hazard and risk analysis.

In order for the Docker to be able to receive the input data and deliver the output data, both input and output folders should be mounted with the Docker container where AP05 is running.

7 AP06 URBAN SUBSIDENCE, MOVEMENT AND DEFORMATION RISK

7.1 Data & Methodology

Analysis of spatial patterns of subsidence phenomena brings insights into hazard distribution and its magnitude. Essential is identification of clusters of subsiding measurement points attributed to similar behaviour and outlying points or clusters dissimilar to behaviour of points in surroundings. Furthermore, given complex nature of potential drivers and size of observable objects in the urban environment multi-scale approach will be adopted.

To understand drivers and impacts of land subsidence at city and sub-city level the intensity of terrain deformation hazard derived by means of MT InSAR technology needs to be integrated with additional supportive information. Distribution and chronology of urban evolution (expansion, densification) may affect (among other factors) both spatial and temporal patterns of land subsidence and should be assessed in relation to observed deformation rate. The module consists of series of Python scripts responsible for spatial-temporal analytics and data fusion. Spatial associations are analysed within results from Copernicus EGMS, or from custom MT InSAR processing chain deployed on DIAS infrastructure. Next, the results are integrated with temporal patterns derived from pan-European and global open datasets describing urban structure (Copernicus Urban Atlas) and long-term built-up evolution (DLR's World Settlements Footprint-Evolution). Output from module is represented by standardized analytics providing added value derived from fusion of scalable inputs.

7.1.1 Data

There are two main types of information needed for this app. First, the **information about the subsidence** measured at stable points (permanent scatterers) distributed over the city and city-region needs to be obtained. For this purpose, the **Sentinel-1 SAR imageries** from Copernicus programme are exploited, allowing to identify potential movements at those points and to follow the pattern of their velocity and direction in time. This is allowed by comparison of the situation with a help of dense time-series of Sentinel-1 imageries. This input data source will – in near future – be replaced by the outcomes of the **Copernicus European Ground Motion Service (EMGS)** (https://land.copernicus.eu/pan-european/european-ground-motion-service) , which should become operational next year (2022).

The second type of information needed by the AP06 is the **information about the spatial pattern of urbanized areas and their development in time**. The first – spatial pattern of urbanized areas - is derived in particular from the **Copernicus Urban Atlas**, which brings highly accurate information about internal structure of the cities - distribution of different types of land use in the cities. If not available, this dataset can be replaced by local city planning maps with Urban Atlas-like nomenclature. This could be relevant in particular in case of potential replications of

the service in outside-European cities. The information about the chronology and spatial pattern of the city development is obtained primarily from the **World Settlements Footprint-Evolution** dataset.

7.1.2 Methodology

7.1.2.1 Measuring terrain movements by means of MT InSAR

The first step in methodology focuses on **acquisition of information about the subsidence itself.** For this purpose, the **Synthetic Aperture Radar Interferometry** (**InSAR**) method is exploited. For over than 20 years, this method has been providing ground deformation data at centimeter precision. In the past decade, new ways of processing satellite radar images have been developed using **Persistent Scatterer Interferometry** (**PSI**) that allow ground movements over wide areas to be detected and monitored with even greater sensitivity. Free and routinely-available SAR data collected by Sentinel-1 sensors' constellation within Copernicus programme represent a unique opportunity for applying these methods on operational level on a global scale (Pepe and Calò 2017). The technique is based on processing of time series of high or very-high resolution satellite SAR imagery which enable detection of up to millimetre displacements. This method has been demonstrated in number of national (Hlavacova et al. 2016; Lazecky et al. 2010) and global EMS related activations and also used for recently awarded state-of-the-art service (TACR Governance Award 2018, CZ) developed by GISAT (Kolomaznik et al. 2016).

By applying multi-temporal InSAR techniques to a series of satellite SAR images over the same region, it is possible to detect movements of the structure systems on the ground in the millimeter/centimeter range and, therefore, to identify abnormal or excessive movement indicating potential problems requiring detailed ground investigation. (Lazecky et al. 2015)

Principles of InSAR measurement techniques and their use for monitoring of deformations in urban areas are illustrated by the two figures below.

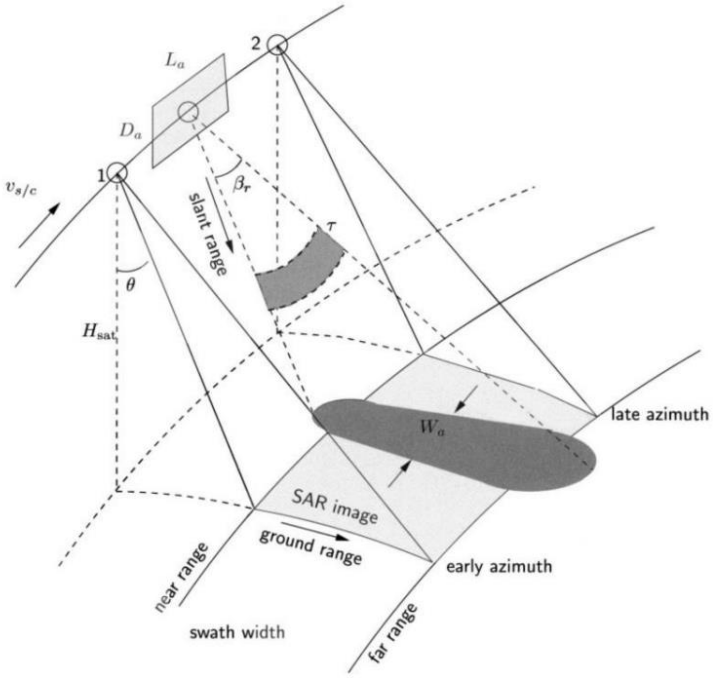

Figure 40. Side-looking image geometry of a spaceborne SAR acquisition. The satellite velocity vs is approximately 7 km/s. The dark gray area indicates the footprint of a single pulse. The total coverage of a SAR scene, between early and late azimuth direction, and near and far range, is depicted in light gray source: EGMS specification and Implementation EEA 2020 https://land.copernicus.eu/user-corner/technical-library/egms-specification-and-implementation-plan)

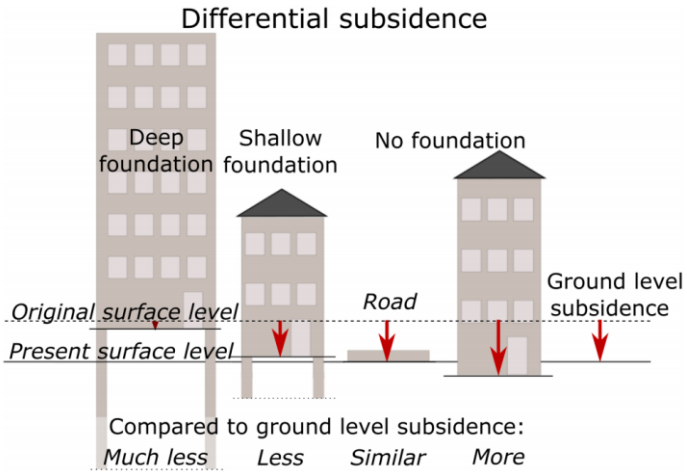

Figure 41. Differential subsidence of individual objects and their relation between foundation depth and weight. Combining this relation with the PSI-estimated subsidence rates can be used to investigate and quantify depth-dependent subsidence rates. (source: Minderhoud et al. 2020)

The subsidence processes are identified and monitored in a multi-temporal manner. The dense time-serie of SAR images (Sentinel-1) allows to follow displacements of selected coherent targets - permanent scatterers points by measuring phase differences between time-series of acquisitions and to estimate average displacement rate.

Figure 42. Stable points with terrain/surface movements subsidence measurements, classified by velocity of movements in urban area.

For each of measurement points the temporal profile is generated, showing the trend of displacements over the observation period as detected in satellite's line-of-sight direction, or as converted into vertical or horizantal (East-West) planes.

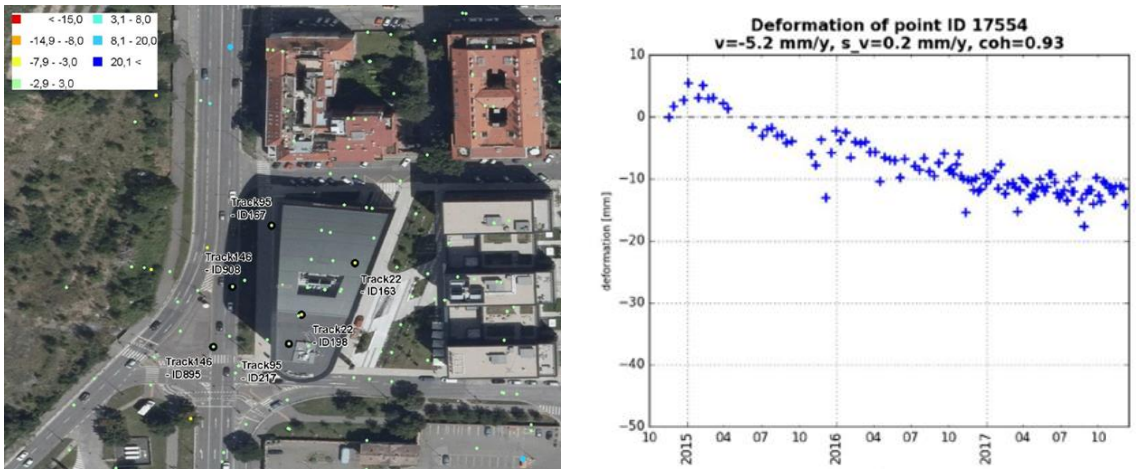

Figure 43. Subsidence measurements for selected stable points in the city area classified by velocity of movements (left), temporal profile of subsidence for selected point.

With a help of these techniques, the displacement rate (average annual velocity) is estimated for each point. Using this method, the points with ongoing subsidence (or other types of surface movements) can be detected. The points are categorized based on velocity of ongoing subsidence to be able to identify the most intensive subsidence processes in the city.

7.1.2.2 Integration with information on urban land structure and evolution

The second step of the methodology consists of **integration of the information about the subsidence with relevant additional data and information** in order to derive meaningful intelligence and understanding about the ongoing subsidence-related processes in the city and surrounding areas. This includes clustering of stable points with subsidence information and spatial overlay analysis (in particular zonal statistics) with the layers representing the structure and development of the city structure.

First, the information about the subsidence is converted to the level of meaningful (functional) urban units using primarily the geometry of the Urban Atlas layer (or building footprints), applying the zonal statistics, in order to obtain information about potential subsidence per each particular land use block. In this step, the Urban Atlas layer can be complemented by custom layers, representing different types of functional urban units, for which the information about subsidence should be derived (e.g. in the Moravian-Silesian region, this analysis can be done for brownfields or undermined areas). Also, similar type of analysis can be done with linear data representing street segments or underground infrastructure like pipelines.

Next, the information about terrain movements is combined with the WSF-Evolution dataset representing chronology of urban expansion of the cities (example in Figure 44). Based on this, temporal profiles of subsidence processes showing their timing (after the building block construction) can be prepared for each of the newly constructed units in the city area.

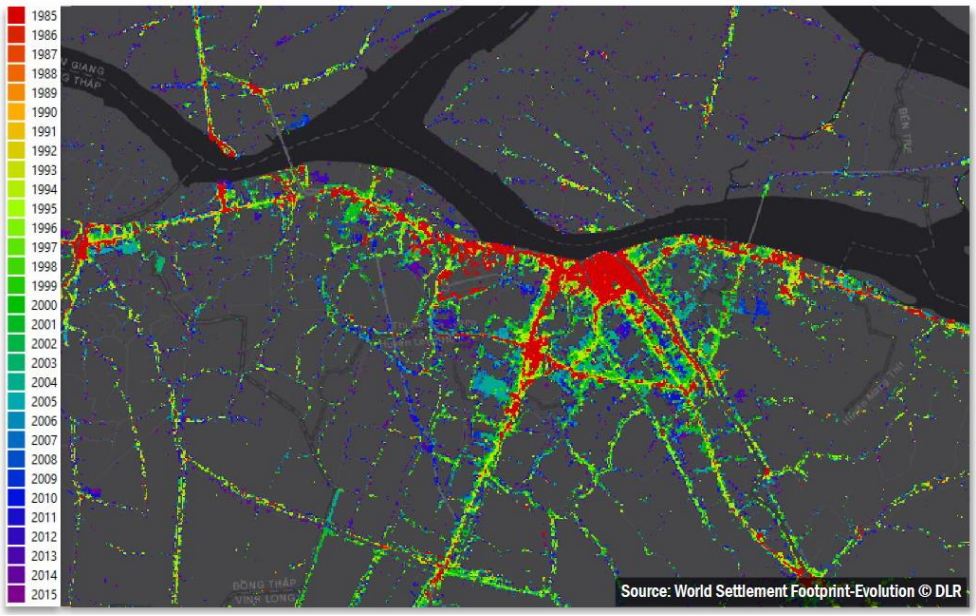

Figure 44. *Spatial-temporal pattern of built-up expansion for selected city as depicted by World Settlement Footprint-Evolution (Marconcini et al. 2018). Colors represent year when built-up was detected for the first time in time series of satellite data. ((Source: EO4SD report, 2020)*

Last, the presentation of the results of these analysis to the end-users will be secured by integration of the data-results into an interactive web-based analytical platform and visualised in an attractive and easy-to-understand manner. The app is based on open-source components and programming languages. Custom GIS layers can be integrated into this application as WMS or WFS, in order to combine these analytical results of the AP06 with the local-city data and information also in sense of visualisation.

7.2 Results

The approach for generation of results of this service AP06 is similar to the one applied in case of the previous flood risk service (AP05). First, the initial estimation of subsidence-related hazard is prepared, using the above described multi-temporal InSAR method, to generate a layer quantifying annual subsidence velocity of on each of permanent scatterer points inside the AOI. Second, this layer is overlayed with Urban Atlas geometry, in order to obtain information about subsidence hazard for urban assets, here represented by functional urban blocks. This is physically the same dataset for which the flood hazard is evaluated, so as a result it combines information about both types of natural hazards - subsidence and flood - at the level of each Urban Atlas block (or Urban Atlas change layer block which contains all areas of change in land use between 2012 and 2018). Moreover, this natural hazard related information is combined with the information about the land use or about the character of local change, coming either directly from Urban Atlas (land use classification, in case of change layer for both 2012 and 2018, which allows for identification of the type of change) or from World Settlement Footprint layer, produced by DLR, which gives temporal information about the year of built-up. Again, as in case of AP05, information about subsidence hazard was collected also at the level of single buildings, distributed over the Heraklion city area (local third-party dataset).

These types of resulting layers (as well as various types of analysis based on these layers) are illustrated by the figures below.

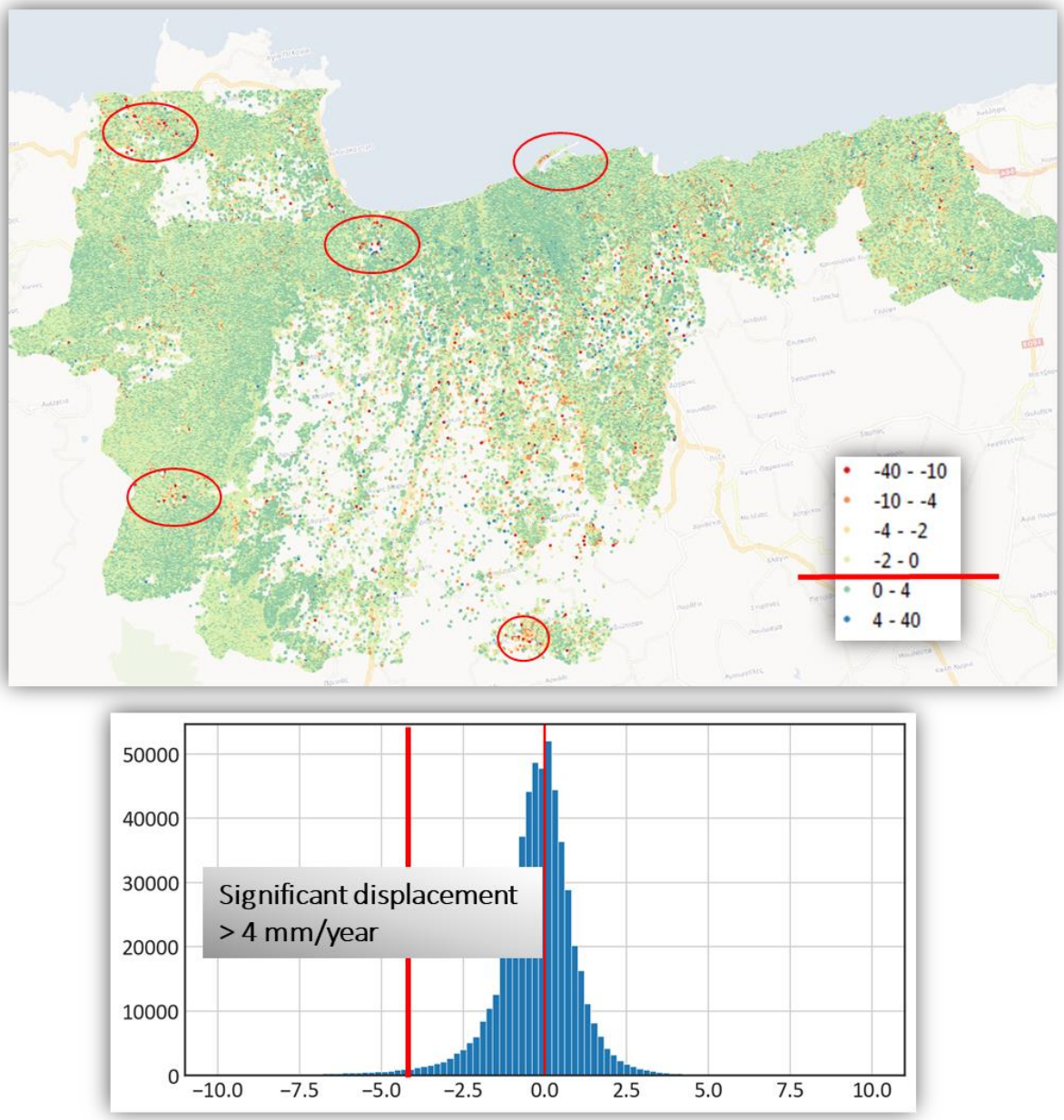

Figure 45. Annual displacement rate (subsidence) on permanent scatterer points distributed over Heraklion city and surrounding area. The red lines/circles indicate locations with significant level of subsidence, with annual displacement rate higher than 4mm.

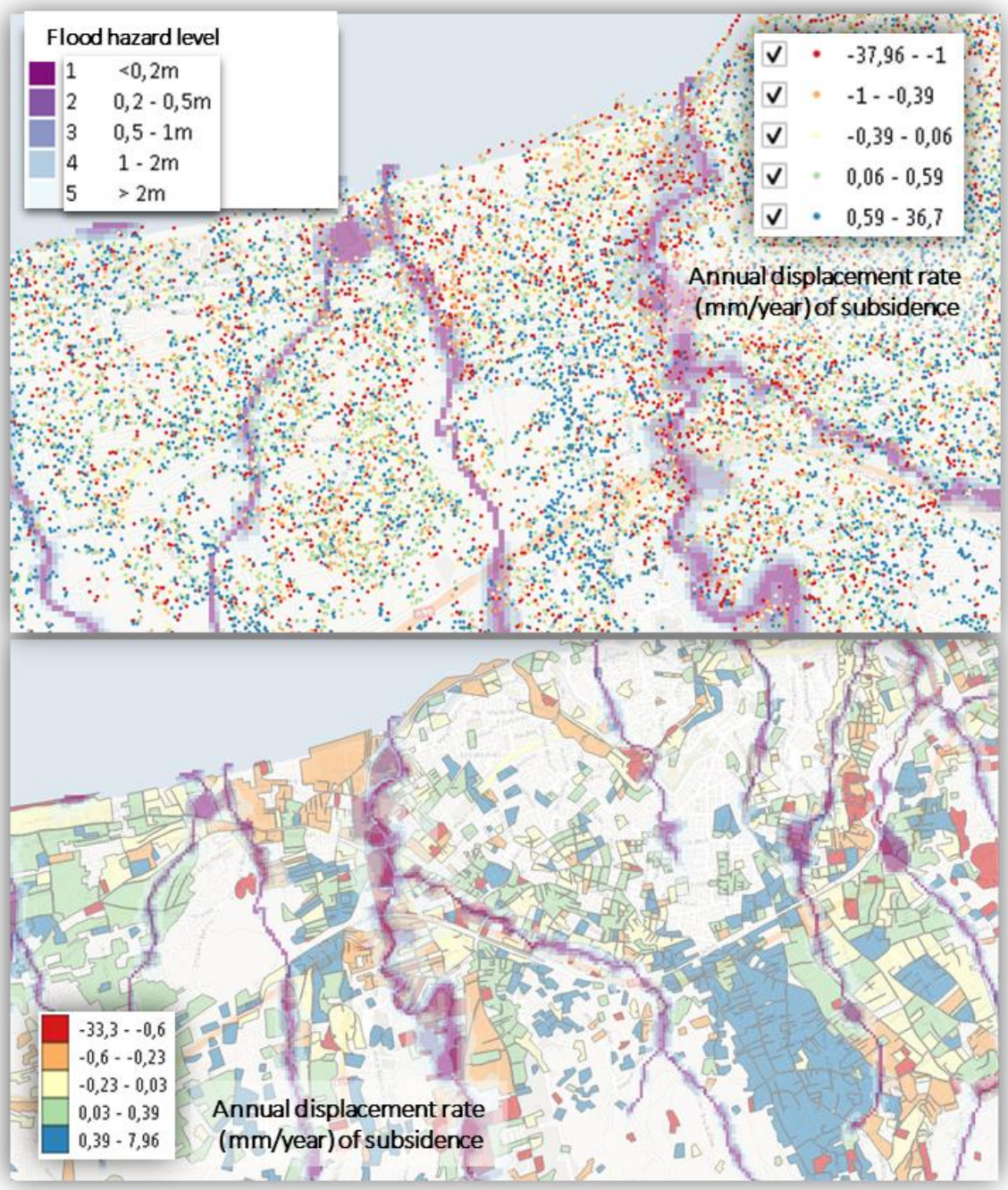

Figure 46. Annual displacement rates (subsidence) on permanent scatterer points and per Urban Atlas blocks, distributed over Heraklion city and surrounding area, combined with information about flood hazard zones.

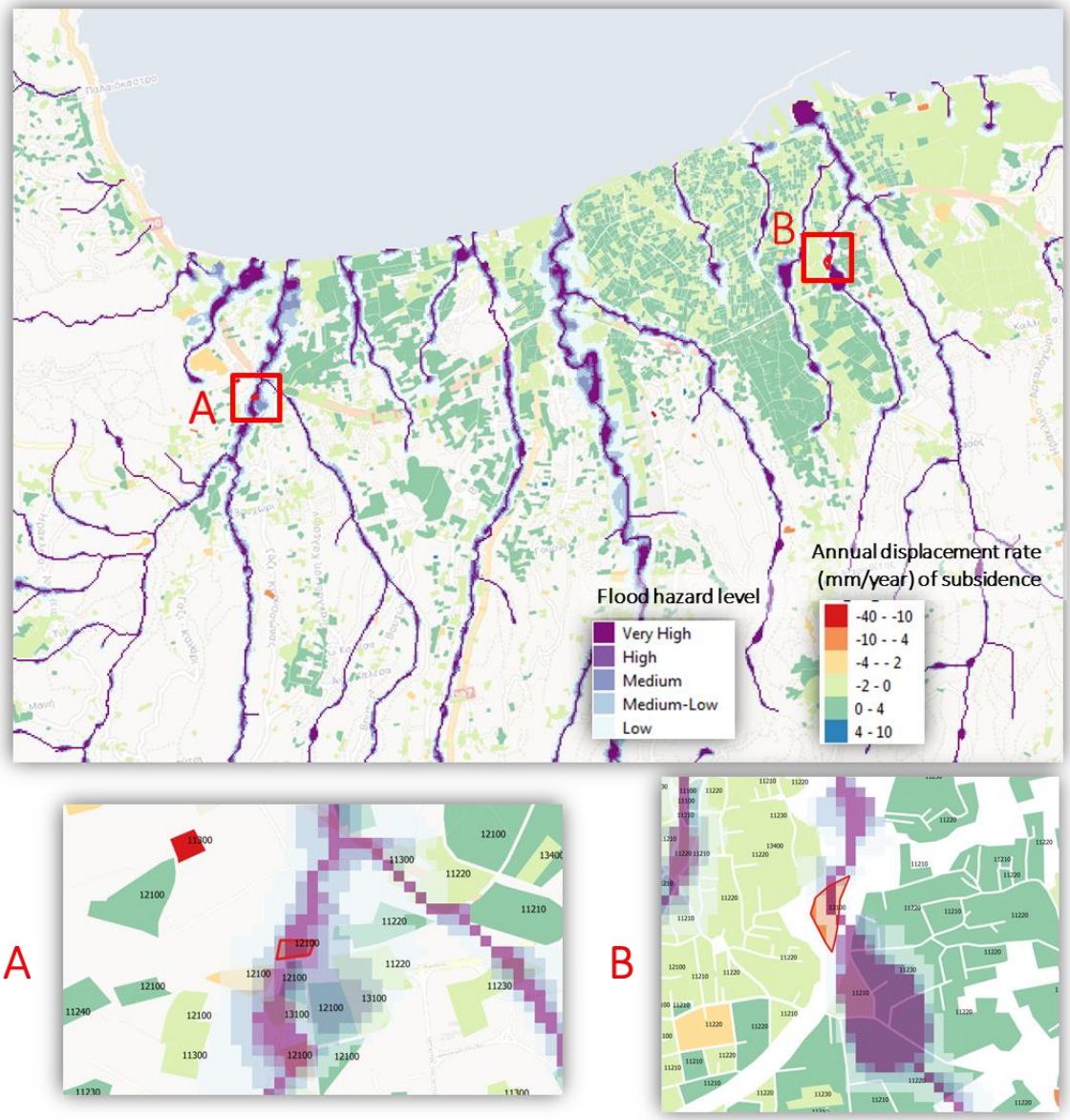

Figure 47. *Example of analysis based on combined AP05 and AP06 product – identification of urban blocks endangered by both flood and subsidence in the Heraklion city area.*

The application not only focused on geographical distribution of the hazard, but also on statistical evaluation of the hazard in context with other characteristics of the AOI. Following figure shows examples of such statistical evaluation. These statistics are generated automatically by the application so it can be prepared for any area of interest. Such statistics may be helpful to identify some interesting subsidence-related trends in the AOI.

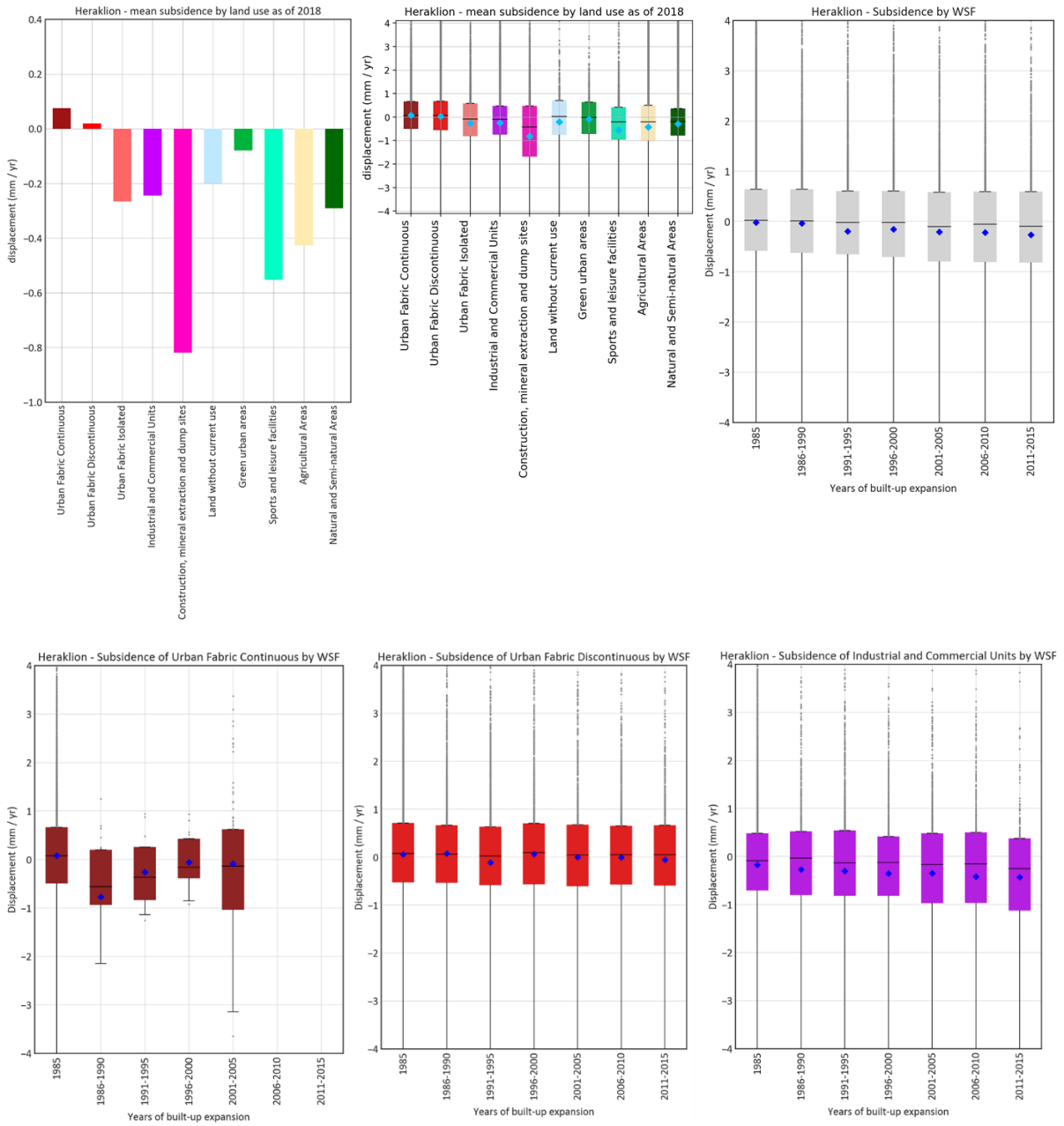

Figure 48. *Example of statistical evaluation of the subsidence hazard – for Urban Atlas blocks of different land use types and built-up in different years (according to WSF-based information).*

In case of follower city, we focused on particular on an undermined area (as a residual of coal mining activity in the Moravian-Silesian Region). This assessment was done on request of the local service end-user – regional authority. This area is called "POHO" and is intended for significant (re)development in the near future, therefore the assessment of subsidence-related hazard in this area is of crucial importance.

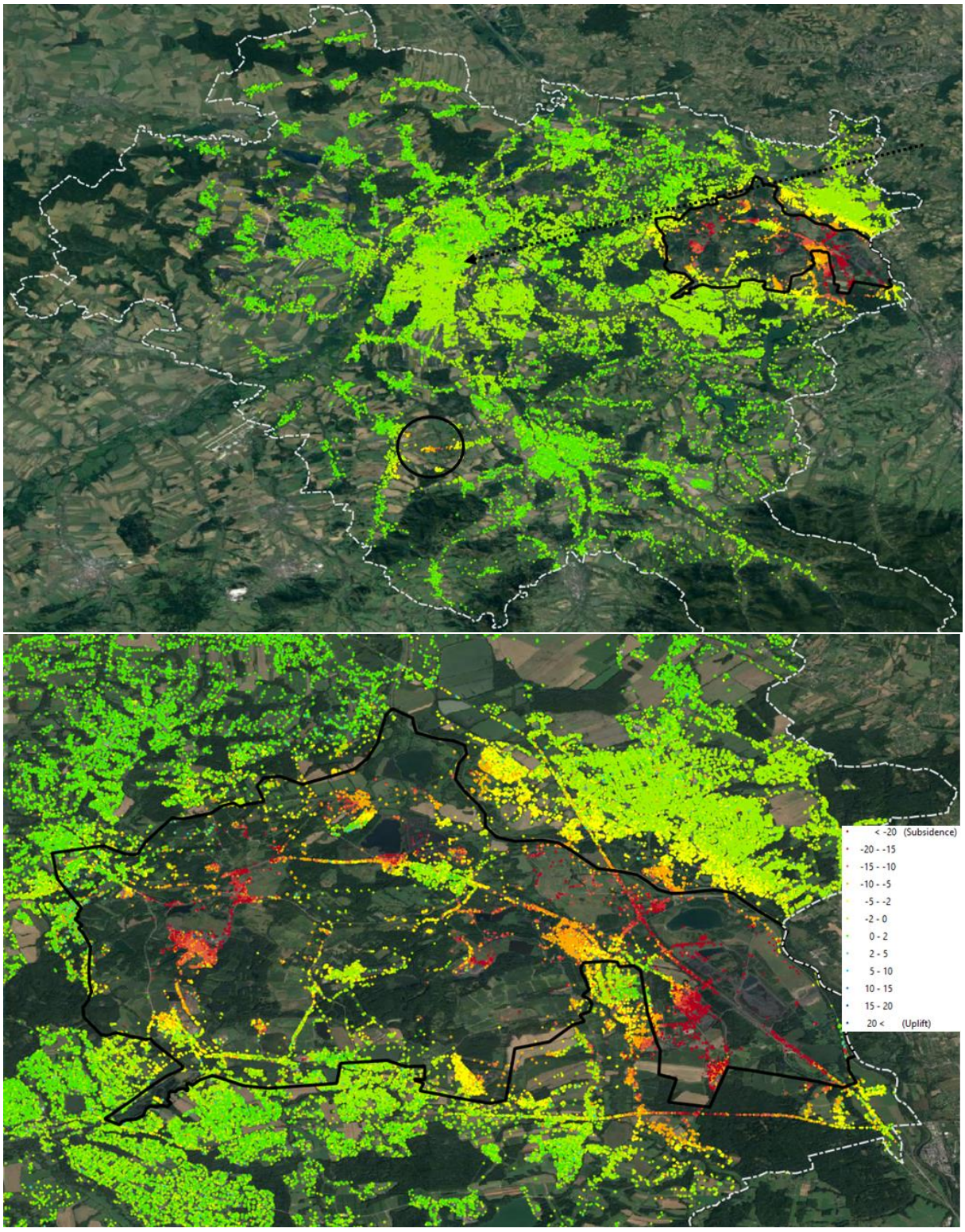

Figure 49. *Results of AP06 (vertical terrain movements) for the follower city-region Ostrava, with particular focus on POHO mining area with significant subsidence processes.*

Figure 50. *Results of AP06 (horizontal terrain movements) for POHO mining area in Ostrava follower city region.*

Moreover, we also prepared an assessment of the surface faulting hazard in the same area. Such analysis helps to identify not only subsidence on permanent scatterer points or their clusters, but more importantly also linear surface faulting, the which represents the biggest hazard related to subsidence processes, leading to high probability of real damage to building or infrastructure in the near future.

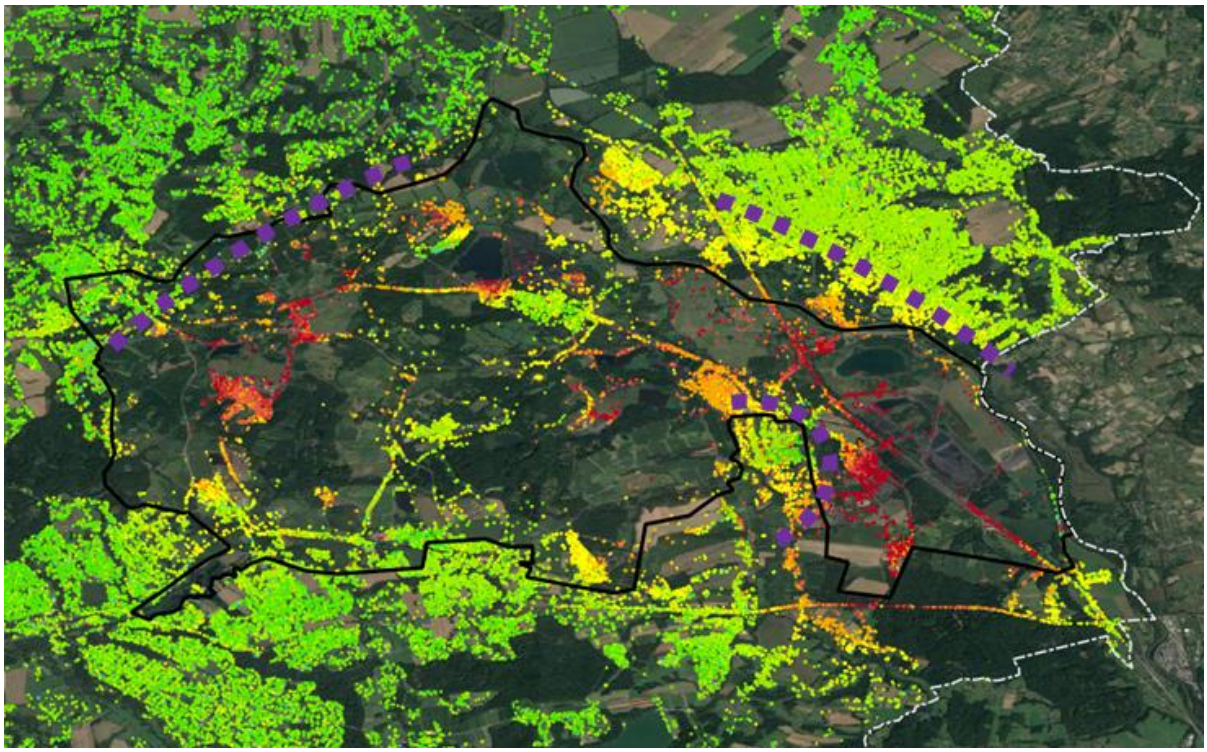

Figure 51. *Identification of linear surface faulting hazards caused by subsidence processes in the POHO area in Ostrava follower city-region.*

Again, based on overlay with Urban Atlas layer, statistical assessment has been prepared for the POHO region to identify differences in intensity of subsidence processes for different types of land use and for areas built-up in different years (according to WSF).

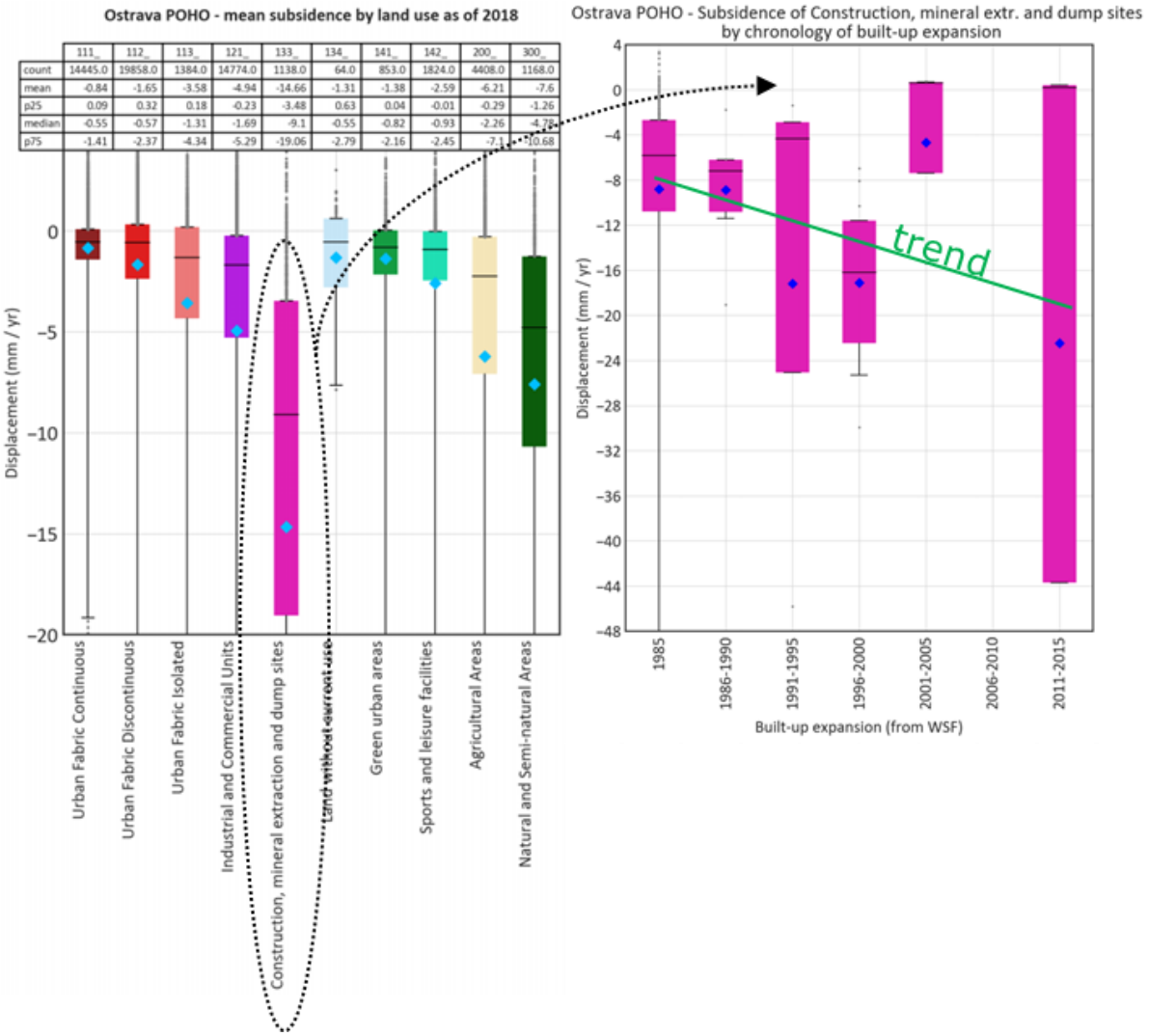

Figure 52. *Example of statistical evaluation of the subsidence hazard – for Urban Atlas blocks of different land use types and built-up in different years (according to WSF-based information). POHO region in Ostrava – highest level of subsidence detected for under-mined areas, with an increasing intensity trend.*

7.3 Evaluation

The MT-InSAR technique and underlying algorithms for the detection of millimetric surface motions are being considered verified and validated by a wealth of operational applications and benchmark campaigns (Minh et al., 2020). Validation depends on the availability of independent reference data obtained by traditional measurement techniques such as GNSS or by geodesy (trigonometry, levelling). In the absence of direct spatially or temporally comparable measurements, the detected deformation patterns may be correlated in space or time with known potential explanatory variables related to (causal) hazard process or event. It must be noted that InSAR techniques often bring valuable insights also for scenarios when no other measurements or reference data are available.

The InSAR outputs from the CURE service could have been validated only partly for the use case focus on the Ostrava-Karvina mining region in the Czech Republic. Here, a reference validation dataset from trigonometric geodetic measurements was provided at the courtesy of OKD mining enterprise / Jiránková, E. from the Institute of Geonics. The temporal range of reference data matches one from interferometric datasets obtained by analysis of Sentinel-1 imagery (2015-2022).

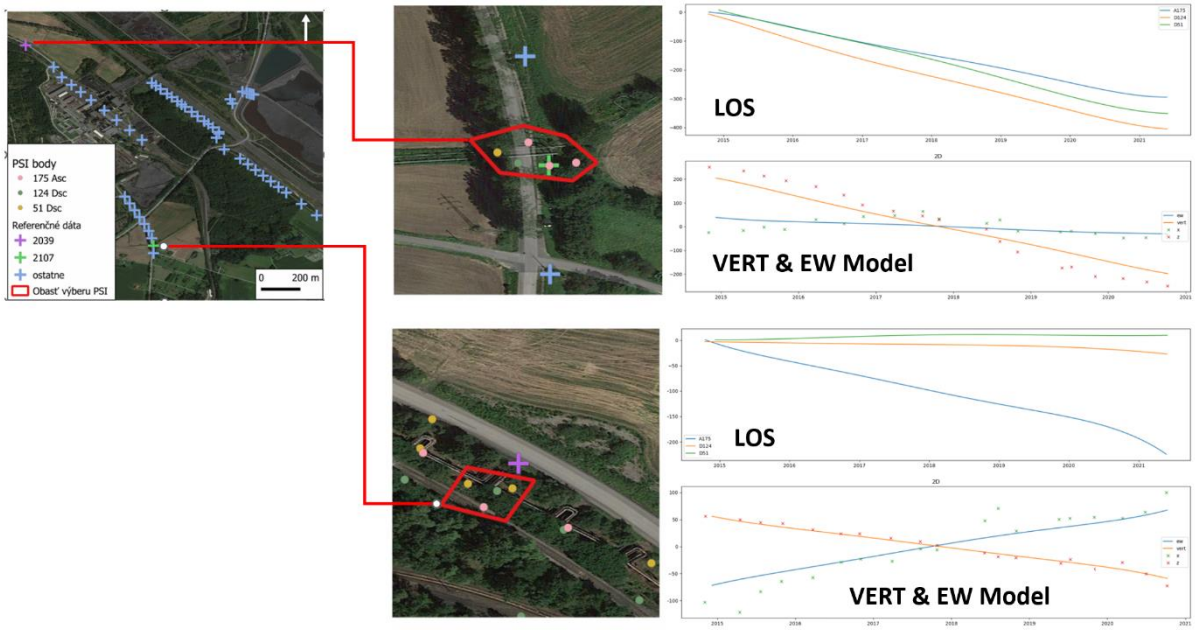

Figure 53. *Comparison of LOS and VERT&EW model between geodetic and InSAR measurements.*

From the several geodetic points on the profile were selected two points with InSAR PS points from all 3 satellite orbital tracks detected in the near vicinity. Displacements detected at the PS points were decomposed and projected from radar Line-of-sight geometry (LOS) to Vertical and horizontal (East-West) directions. Geodetic measurements (in X, Y, Z coordinates) were converted into Vertical and E-W motion fields to be comparable with InSAR measurements. The model based on geodetic measurements fits well with decomposed reprojected InSAR measurements.

InSAR measurements cover the Ostrava-Karvina mining area with heterogeneous density and achieve variable reliability represented by interferometric coherence indicator. However, due to non-linear displacements frequently occurring in areas affected by deep mining (acceleration, deceleration), some results are subject to errors from phase unwrapping. In these cases, estimated displacement velocity and cumulative displacement are misestimated. On the other hand, the error can be identified by the assessment of time series plots. It is assumed that the phase unwrapping errors are present in the results provided by GISAT in the frame of CURE as well as in EGMS results.

In addition, a comparison between GISAT and EGMS L3 products could be accomplished after EGMS results were made available to download in November 2022.

Preliminary analysis shows that in areas not affected by phase unwrapping errors, there is a good match between the two datasets. Match (expressed as % of rejected null hypothesis about match between the velocity at nearest points from two datasets) is considerably lower in areas with known displacement dynamics and the presence of unwrapping errors.

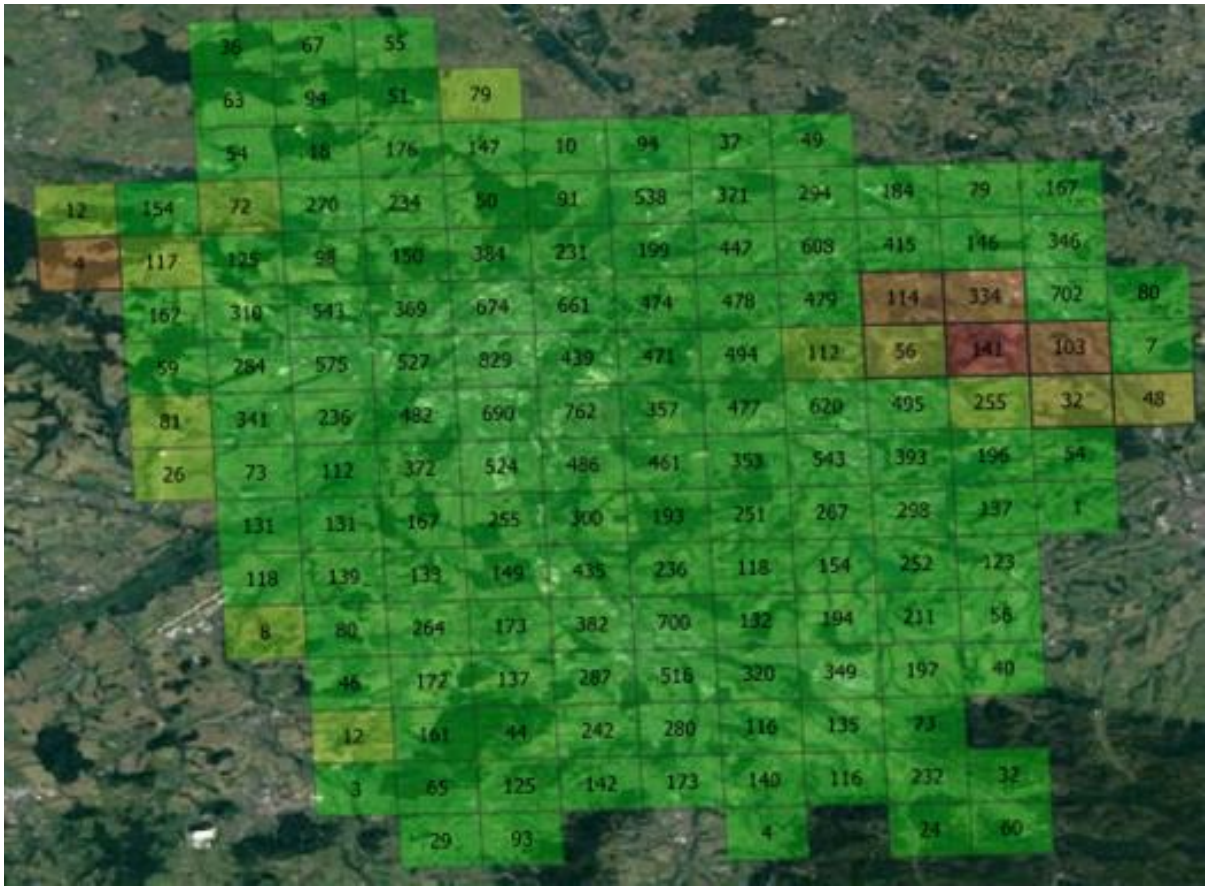

Figure 54. *Comparison between Gisat MT-InSAR outputs and EGMS outputs (both at l3 product level – velocity in vertical direction). Share of matching measurement couples within each grid cell.*

Results from differential InSAR for Arkalochory could not be validated as no reference datasets were available. On the other hand, it may be noted that the outputs from DInSAR analysis correspond well with outputs from other authors (Triantafillou et al., 2021) both visually and in terms of displacement maxima position and quantity. Displacement maxima detected by Gisat and other authors exceeded -20 cm in the vertical direction and well below +/-10 cm in the Eastward and westward directions.

7.4 Application Dockerization

AP06 has been implemented with Python and GDAL. It has been packaged in a Docker image with all the required libraries. The Docker can run AP06 as a standard Python script along with all the parameters needed as input depending on the user inputs. Processing can be coupled with AP05 docker into multi-criteria hazard and risk analysis.

In order for the Docker to be able to receive the input data and deliver the output data, both input and output folders should be mounted with the Docker container where AP06 is running.

8 AP07 URBAN AIR QUALITY

8.1 Data & Methodology

8.1.1 Urban air quality

Urban air quality is a multi-scale problem. Pollutant concentrations on a street-level scale are influenced by regional background concentrations, urban increments due to local industrial, traffic and residential heating sources, and an additional contribution coming from recirculation in narrow streets with high rise buildings adjacent to it (the so-called street-canyons). Only when the contribution of all three scales is taken into account, the urban air quality exposure can be correctly determined. As illustrated in Figure 55, monitoring the compliancy of limit values also requires the combination of the three scales, as otherwise local exceedances could be overlooked.

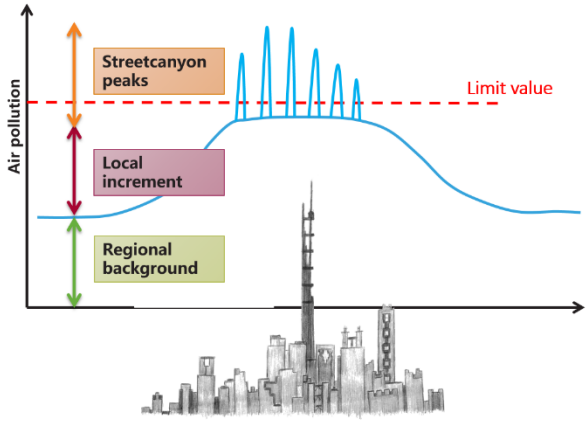

Figure 55. Illustration of the different scales involved in urban air quality assessment.

8.1.2 ATMO-Street model chain

CURE Application 07 assesses the urban air quality using the ATMO-Street application. ATMO-Street is an integrated air quality model chain (Lefebvre et al. 2013a), designed to correctly assess and combine the different scales of urban air quality. The model chain relies on several underlying models and input datasets to compute the air pollution at street-level scale (10m) for an urban area. The flowchart of the model chain is provided in Figure 56. In the next paragraph, we provide a general description of the model chain. Section 8.1.3 describes the model components and their interlinkage more in detail.

The ATMO-Street model chain starts from datasets describing the most important local emissions in the domain under consideration. For urban areas in Europe, road traffic, industrial and residential heating emissions are generally considered. Preferably, all three emission datasets are provided at a high resolution: residential and industrial sources are typically represented by a point source for each company / house with stove, while line sources (i.e.

one value per road segment) are used for road traffic emissions. If industrial and residential sources are not available at this high resolution, surface sources with a somewhat lower resolution (e.g. 5 by 5 km) can be used as an alternative. Based on the high-resolution emissions data, two core models compute the local contribution to the air pollution at a resolution of 10m: the bi-gaussian plume dispersion model IFDM accounts for the impact of local emissions from traffic and industry (Lefebvre et al. 2013b), while the street-canyon module OSPM calculates the in-street increment resulting from street-canyon effects (Berkowicz et al. 1997). To correctly assess the local contribution, these models require two additional datasets. Meteorological data (vectorial wind speed and temperature) is required to correctly assess the dispersion, while a detailed 3D building dataset (relying on building layouts using polygons) is required to correctly assess the recirculation in street canyons. In a final step, the total air pollution is computed by combining the local contribution with the regional background concentrations. These background concentrations contain the pollution caused by all the sources outside the model domain, and the sources that are not explicitly considered in the emission data (e.g. emissions for other sectors, such as shipping and non-road transport). This data is either based on results of regional background models or measurements (possibly combined with spatial interpolation using e.g. land use regression models).

The ATMO-Street model chain is the official air quality model chain in Flanders. It is used by the Flemish Environmental Agency for the assessment of current and future air quality, and its output is reported to the European Commission. The model chain has recently also been used in many other countries, including Poland, Slovakia, Hungary, Croatia and China. The model chain has been validated using several measurement campaigns, focusing on spatial patterns and time series alike (Lefebvre et al. 2011, Lefebvre et al. 2013a). Most of these validation campaigns focused on a relatively small number of sampling locations, with at most a few dozens of locations distributed among a single urban region. Recently, however, the Curieuzeneuzen Citizen Science air quality measurements have been used to validate the model using measurements for 20.000 sampling locations in Flanders (Hooyberghs et al. 2020). The validation highlights the capability of the model chain to correctly assess the spatial variation of the air pollution in Flanders.

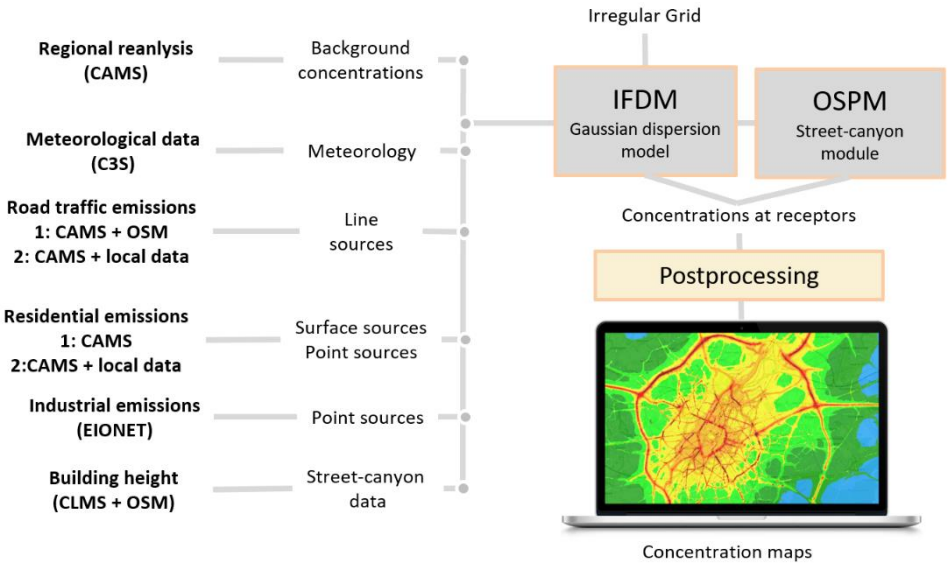

Figure 56. *Flowchart of the ATMO-Street model. The numbers refer to the two options for downscaling used in the current project (fully Copernicus or Copernicus combined with local data for downscaling). More details: see text.*

In CURE, the (raw) input data for the ATMO-Streets model chain stems as much as possible from Copernicus datasets. Emissions are retrieved from the Copernicus Atmosphere Monitoring Services (CAMS), meteorological data from the Copernicus Climate Change Service (C3S), and building information from the Copernicus Land Monitoring Service (CLMS). Additionally, industrial emissions of the European Environment Information and Observation Network (EIONET) have been used.

Although the resolution of the CAMS emission inventories for Europe has increased in recent years, there is still a significant gap between the resolution of the inventories and the resolution required in street-level scale urban air quality modelling. The emission data has therefore been combined with higher resolution proxy data to downscale the CAMS emissions to the requested resolutions (point sources / surface sources for residential emissions, and line sources for traffic emissions). For the frontrunner city Sofia, two options for the downscaling are considered. In the first set-up, we have relied on the global open-source roadmap OpenStreetMaps (www.openstreetmaps.org) to downscale the emissions to line sources, and used the residential emissions of CAMS at their native resolution (0.05 by 0.1 degrees). This first option is therefore transferable to any location in the European Union. In the second setup, a local bottom-up roadmap (with information on the road capacity) and a local dataset describing the location of heaters are as well considered. We expect that the final downscaled emissions of this second method are more in line with the real-life situation, but the method is no longer transferable to other cities.

To highlight the transferability of the former, open-source based methodology, this downscaling procedure is also applied for two follower cities, Bristol and Ostrava. For both cities, only this method solely based on open-source datasets is applied.

Table 9 provides an overview of the datasets used in the urban air application. Section 8.1.4 describes the input datasets and the downscaling of the emissions for both set-ups in more detail.

Table 9. *Overview of the input datasets.*

Copernicus service	*Dataset*	*Type*	*Usage*	*Cities*
CAMS	Regional air quality reanalyis	Air quality data	Background concentrations	Sofia, Ostrava and Bristol
CAMS	Regional Emissions for Air Pollutants (REG-AP), v3.1	Emissions	Road traffic and residential emissions	Sofia, Ostrava and Bristol
C3S	ERA5	Meteorological data	Meteorological data	Sofia, Ostrava and Bristol
CLMS	Urban Atlas	Building Height	Building height	Sofia
-	OpenStreetMaps	Building layout	Building layout	Sofia, Ostrava and Bristol
-	OpenStreetMaps	Road map	Downscaling traffic emissions	Sofia, Ostrava and Bristol
-	Road map Sofia	Road map	Downscaling traffic Emissions	Sofia
-	EIONET Large Point Source data	Point source data	Industrial emissions	Sofia, Ostrava and Bristol
-	Inventory of wood and coal burning heaters in Sofia	Location of heaters	Downscaling residential emissions	Sofia

8.1.3 Building blocks of the ATMO-Street model chain

Local open-street concentrations due to traffic emissions and point sources are modelled by the bi-Gaussian plume model IFDM (Immission Frequency Distribution Model) (Lefebvre et al. 2013b). IFDM is a receptor grid model: air pollutant concentrations are computed for an abundance of receptor locations. Instead of a regular grid, we use a pointsource- and road-following grid. This approach ensures that more receptor points are available where the largest concentration gradients are expected (Lefebvre et al. 2011). The chemical equilibrium in the

NOx-O3 reaction is determined on the basis of temperature and solar height and is based on the fast-ozone-chemistry scheme (Berkowicz et al. 2008).

To take the effect of buildings on the street level concentrations into account, the IFDM model is coupled to the Operational Street Pollution Model (OSPM) (Jensen et al. 2017). OSPM models street level concentrations due to traffic emissions using a combination of a plume model for the direct contribution and a box model for the recirculating part of the pollutants in the street. In the current set-up for OSPM, a receptor location is placed every 20m on each road with a row of buildings adjacent to the road (i.e. at a maximum distance of 50m to the middle of the road).

The concentrations at the receptor locations of the IFDM and OSPM model are combined and gridded in a three-step postprocessing module. At first, IFDM results are gridded using Delaunay triangulation to obtain gridded open street concentrations. Secondly, we grid the OSPM results using nearest-neighbour interpolation. In the last step, both gridded maps are combined into a map with a 10m resolution, by using the OSPM results at locations where buildings are adjacent to the road, and the IFDM results at all other locations.

8.1.4 Data for the city Sofia

Table 9 provides an overview of the datasets used in the urban air quality application. In the following paragraph the datasets and the required processing are described in more detail. In this paragraph, we describe the model input for the frontrunner city Sofia, while the next paragraph focuses on the modifications applied for the follower cities Bristol and Ostrava.

8.1.4.1 Meteorological data

ATMO-Street requires hourly (vectorial) wind speed and temperature data. Both parameters are taken from the ERA5 reanalysis dataset of the Copernicus Climate Change Service (C3S). ERA5 provides surface temperature and wind speed with a resolution of 30 kilometre. We interpolate the data to the centre of the domain using bilinear interpolation.

8.1.4.2 3D building model

To correctly assess the street-canyon contributions, ATMO-Street requires a 3D model of the city under consideration. The 3D model requires at least the following two parameters:

- Building height
- Ground plan of the building, preferably described using a polygon (sub-meter resolution is required).

Building heights are available in the CLMS Urban Atlas for all European capitals. Although the dataset is already a few years old (dating from 2012), we assume that the urban fabric has not changed too much in the European capitals.

The Urban Atlas provides building heights at a resolution of 10m, but it does not provide a building layout. Since the façade-to-façade distance is one of the most important parameters

in street-canyon models, an additional dataset is required to build a full 3D model of a city. We make use of the open-source OpenStreetMaps dataset, which includes a polygon layer with the exact location of the buildings. Figure 57 further visualizes the gridded CLMS data and the polygon of OpenStreetMaps.

Figure 57. Illustrations of the two datasets used for the 3d building model. The blue lines indicate the ground plan of the buildings according to OpenStreetMaps data, while the yellow-to-red colors indicate the building height according to the 10m resolution UrbanAtlas dataset. Background image: OpenStreetMaps.org.

As OpenStreetMaps is a crowd-sourced project, the quality and completeness of the data varies greatly between different areas. We have controlled the completeness for Sofia using a visual comparison with satellite data, and with the (lower resolution) building height of Urban Atlas. Most buildings in the inner-city are correctly represented, and only some residential neighbourhoods in the outskirts are missing a considerable number of buildings. These locations are however not important for the air quality applications, as the highest concentrations are expected in the inner-city.

The CLMS and OpenStreetMaps data are combined using geospatial tools. For each building polygon in OpenStreetMaps, we determine the mean height of the overlapping grid cells from the CLMS Building Height layer.

8.1.4.3 Background concentrations

ATMO-Street's components IFDM and OSPM only explicitly take the concentrations due to traffic, residential and industrial emissions in the city into account. Concentrations due to other emissions in the city (e.g. rail transport, trade and services etc) and emissions outside the city are not taken into account. These 'background' concentrations vary over a longer spatial scale (order of kilometres rather than order of metres), and are therefore not explicitly modelled in the urban air quality applications. They are, however, added to the final concentrations field using a regional background concentration from CAMS.

CAMS provides hourly regional background concentrations for Europe in the 'Regional reanalysis datasets.' This dataset assimilates the output of regional air quality models (so-called chemical transport models, CTMs) with measurements of the official measurement networks of the EU-countries. The resulting dataset comprises gridded hourly concentrations for Europe with a resolution of 0.1 degree, for nitrogen dioxide, ozone, and particulate matter. The most recent dataset contains concentrations for 2018.

Directly coupling the background concentrations to the local concentrations field would give rise to sharp gradients at the edges of the CAMS grid cells. Therefore, the CAMS data are resampled to a concentration field with a 2000m resolution using bilinear interpolation.

8.1.4.4 Emissions

ATMO-Street requires high resolution emission data for road traffic, industry (including powerplants), and residential heating. In the following paragraphs, these three sectors are discussed in detail.

Industrial emissions

For industrial emissions, we rely on the figures reported by the member states of the European Union to the Central Data Repository (CDR) of the European Environment Information and Observation Network (EIONET). According to directive 2016/2284/EU the member states must every four years report the air pollutant emissions of large point sources (LPS), which the EU subsequently reports to the United Nations Economic Commission for Europe (UNECE) Environment and Human Settlements Division under the Convention on Long-range Transboundary Air Pollution (CLRTAP).

The data for Bulgaria is publicly available on http://cdr.eionet.europa.eu/bg/un/clrtap/lps/envwqsyda/. We use the data reported in 2017 (which refers to the situation in 2015). For Sofia, the dataset contains emissions for four powerplants and one industrial plant. In all five cases, a high stack is present (ranging from 70 to over 130m high), and it is therefore expected that the influence of these industrial emissions on the ground concentrations is rather limited.

Road traffic emissions

Several global and regional emissions datasets have recently been developed under the CAMS umbrella (CAMS 2019). In the current set-up, we use the CAMS regional anthropogenic emissions for Europe, using the CAMS–REG-v3.1 dataset developed by TNO. This dataset provides gridded emissions on a 0.1 by 0.05 degree resolution for several sectors (including road traffic and residential combustion) and several air pollutants (including NO2 and PM10). Version 3.1 of the dataset provides total annual emissions for 2016. Monthly profiles are provided by the CAMS-TEMPO dataset.

ATMO-Street requires emission data for all the line segments in the domain. The total CAMS emissions in Sofia have therefore been combined with higher resolution proxy data to

downscale the CAMS emissions to the requested resolutions. As mentioned above, two options have been considered: a first option relying on pan-European datasets, and a second option relying on local datasets. More in detail, the downscaling uses the following proxy data:

1. In the pan-European methodology, the road map of OpenStreetMaps is used. The emissions are spread over all the roads in the domain according to the number of lanes for each road (thus assuming that more vehicles are using roads with a larger number of lanes). Moreover, we assume that the emissions on a highway segment (roadtype trunk or motorway in OSM) are twice as large as the emissions on other types of roads, because vehicle speeds and vehicle numbers are in general larger on highways. Note that is method is rather crude, and does not use any local knowledge.
2. The local method uses a bottom-up dataset of the Sofia municipality. The dataset indicates for each road the maximal capacity of the road. We assume that the emissions can be spread over all the roads according to their maximal hourly capacity. Note that this method is less crude than the pan-European methodology, but it is still far from perfect. In an ideal situation, the CAMS emissions are either spread over the domain according to realistic traffic flows, which consider the morphology of the city (e.g. some roads link residential and office areas, and are therefore much more used during rush hours etc). Alternatively, the road traffic emissions could by calculated using a traffic emission model, which combines the traffic flows with the traffic fleet and bottom-up emission factors.

Residential emissions

For the residential emissions, we anew start from the CAMS REG-AP-v3.1 dataset, but this time we use the data for the residential combustion sector. The rest of the processing differs for both set-ups:

1. When only using pan-European datasets, there is no decent proxy data to further downscale the emissions to individual houses or wood / coal burning devices. We therefore use the emissions on a 0.05 by 0.1 degree resolution. The emissions are therefore spread over the entire urban area, and we will certainly miss some important PM hotspots in neighbourhoods with a large share of wood and coal burning.
2. The Sofia municipality has compiled a large dataset containing the location of all coal and wood burning heaters. In the second method, we spread the total emissions in Sofia uniformly over all these devices. Note that this entails an important assumption, and will cause some uncertainty. After all, in real-life, the emissions of individual heaters strongly depend on the characteristics of the heater (type, age, maintenance...), and the way in which the heaters are used. This type of data is, however, not available at the level of individual heaters in the entire city.

8.1.5 Data for the Bristol and Ostrava

The methodology to gather the input data for Bristol and Ostrava mimics the one for the frontrunner city Sofia. However, as some datasets are unavailable for follower cities, we have to modify the roadmap a little. In this section, we provide an overview of the updates to the methodology. Datasets that are not mentioned in the following paragraphs, are composed in exactly the same way as the ones for Sofia.

The only pan-European dataset that is unavailable for Bristol and Ostrava is the Building Heights dataset of CLMS, which is currently only available for the European capitals. For the follower cities, we therefore use a rough estimate for the building heights: we assume a fixed building height of 15m for each building in the domain. This rough estimate will have an influence on the quality of the model results for street-canyon locations.

The local datasets for Sofia (location of coal and wood burners and road capacity) are also unavailable for the follower cities. For these cities, we will hence only use the downscaling method based on the pan-European OpenStreetMaps dataset for the traffic sector, and only use the CAMS residential emissions at their native resolution (0.05 by 0.1 degree).

8.1.6 Limitations and validation

As mentioned in the earlier paragraphs, there are several limitations and uncertainties related to the methodology applied for the urban air quality application. Most of the uncertainties are related to the Copernicus datasets and the downscaling of these data to the required resolution, but there is an additional uncertainty related to the model core (IFDM-OSPM). We for instance observe the following limitations:

- The background concentrations are based on the CAMS regional reanalysis data, which are the result of an air quality model on a regional scale. Although the results have been assimilated with measurements, we have observed underestimations of the background concentrations by CAMS in other cities (e.g. Bratislava).
- Similarly, wind and temperature input data are an assimilation of model data and measurements. Although the quality of these type of reanalysis products has been greatly improved recently (e.g. with the update from ERA-Interim to ERA5), there could be some deviations from the actual local data.
- Downscaling the emissions to individual point sources and road segments comes with an important uncertainty. The quality of the downscaling greatly depends on the quality of the proxy data that have been used. We thus expect better results if we rely on a combination of local data and pan-European / global proxy datasets. Note, however, that although the local datasets are the best available proxy data, they are not the ideal proxy data (e.g. capacity instead of traffic volumes / no information on wood / coal burning heaters).
- For the follower cities, only a rough estimate for the building heights is used (fixed buildings height of 15m). This assumption will cause large uncertainties for the street-

canyon concentrations, which are very sensitive to minor changes in the building heights.

- The model has initially been developed to model the air quality in Flanders, and therefore relies on a stability scheme based on measurements in Flanders.

8.2 Results

8.2.1 Total annual mean concentrations

The primary outcome of the air quality application are air quality maps describing the yearly mean concentrations of nitrogen dioxide (NO_2) and particulate matter ($PM_{25)}$ with a resolution of 10 by 10 meters. We focus on the year 2018, as it is the most recent year for which background concentrations are available.

The figures below show sample results for Sofia, Ostrava and Bristol. For Sofia, we show the results of both set-ups described in the previous paragraph. The maps highlight how the urban air quality varies strongly over short distances. For NO_2, the highest concentrations are observed near the most important roads, with the highest concentrations occurring in busy street canyons in the city centre. The highest concentrations for particulate matter are, on the other hand, observed in the neighbourhoods with an abundance of residential emissions, especially when considering the runs in which the Copernicus data has been supplemented with local data.

The results for the frontrunner city Sofia moreover highlight the major differences between both set-ups. Although the total emissions in the domain are the same for both set-ups, the spatial pattern of the air pollution is markedly different. The contribution of the residential sector is much more homogeneous for the set-up only relying on open-source datasets, which is caused by the emissions being spread over the entire metropolitan area (instead of being focussed on the areas in which most heat burners are located). These differences are due to the large gap in resolution between the input Copernicus data and the high-resolution model chain, and highlight the need for local data to improve the final concentration maps.

The maps allow stakeholders to identify the neighbourhoods and districts with the worst air quality, and to decide in an informed manner for which areas action should be prioritized. Moreover, the maps can be used for compliance checking. The EU Ambient Air Quality Directive sets a threshold of 40 $\mu g/m^3$ respectively 20 $\mu g/m^3$ for the yearly mean NO_2- and $PM_{2.5}$-concentrations. We thus observe a breach of the standards for NO2 in the busiest street canyons, while the standards for $PM_{2.5}$ are breached at most locations in the city centre. The more stringent updated WHO guidelines (10 $\mu g/m^3$ for NO_2, and 5 $\mu g/m^3$ for $PM_{2.5}$) are exceeded at all locations in the model domain, both for NO_2 and $PM_{2.5}$, indicating that significant negative health impacts are observed everywhere in the metropolitan area.

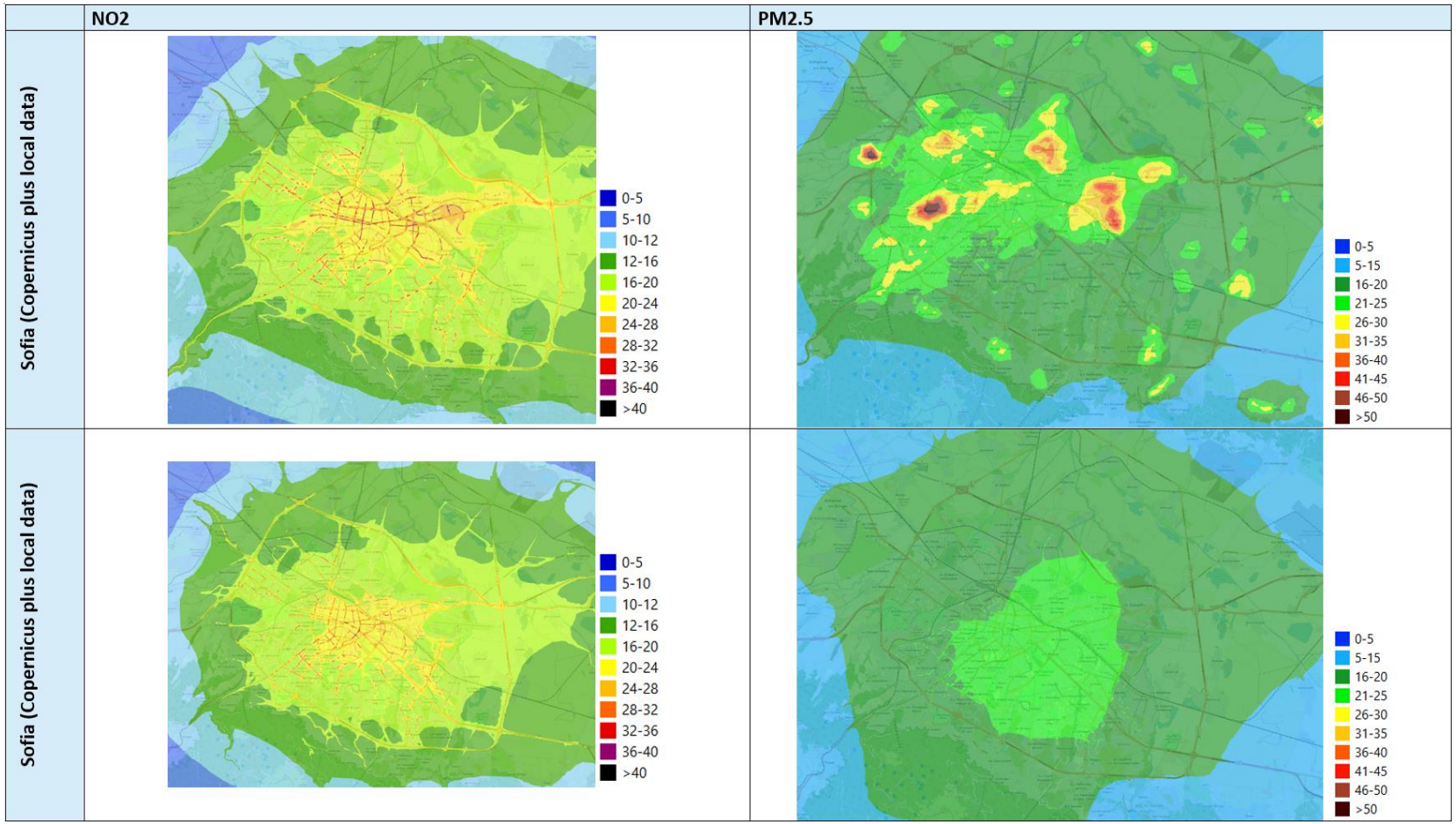

Figure 58. *Total annual mean concentrations in µg/m^3 for the core city Sofia. The left figures show the NO_2-pollution, while the right figures provide the results for $PM_{2.5}$. We show both the results for the methodology using only Copernicus data (bottom row), and the methodology in which the downscaling of the emissions is complemented with local data (top row).*

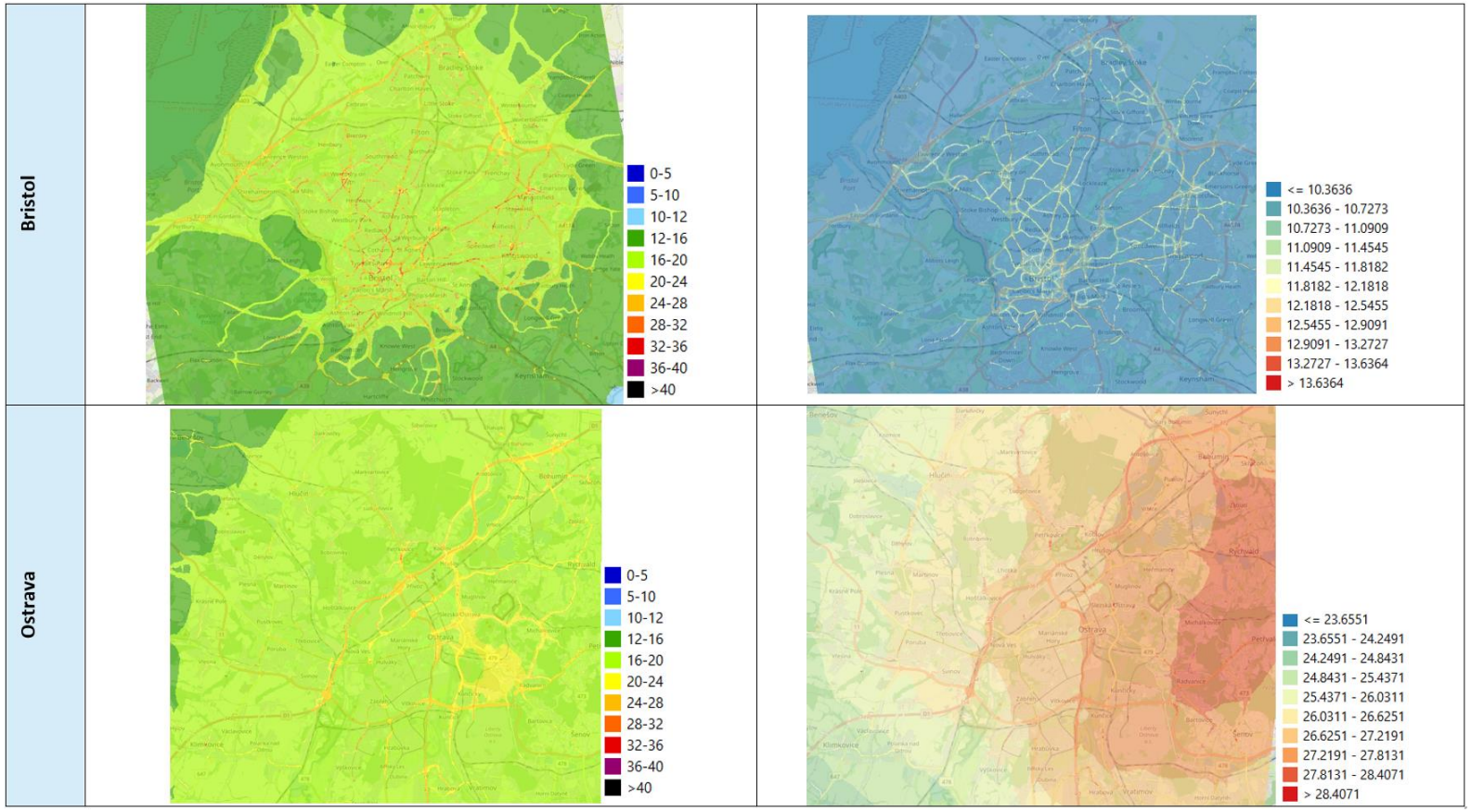

Figure 59. Total annual mean concentrations in µg/m3 for the follower cities Bristol and Ostrava. The left figures show the NO_2-pollution, while the right figures provide the results for $PM_{2.5}$.

8.2.2 Sector contribution

A second output of the urban air application concerns the sector contribution. For each of the sectors that are explicitly considered in the local modelling (road traffic, industry, power plants and residential heating), also the approximate contribution of the individual sector to the total concentration is provided[5]. Using these results, stakeholders can identify key sectors for which measures are prioritized. The sector contribution also provides a rough estimate for the (theoretical) maximal pollution reduction due to local measures for the sector under consideration. Sample results for Sofia (based on the air quality modelling relying on Copernicus data supplemented with local datasets for the emission downscaling) are shown in the figure below, both for NO_2 and $PM_{2.5}$. The sample results for particulate matter for instance highlight the importance of the urban residential emissions at this specific location. Also, the urban traffic emissions contribute a significant fraction to the total concentrations, whereas the urban power plant and industrial emissions are responsible for only a negligible fraction of the total pollution. Approximately a third of the pollution at this specific location is emitted outside the domain, or by sectors that are not explicitly considered in the modelling. The results for NO_2 can be interpreted in a similar way, indicating the importance of the traffic emissions at this specific location.

5 For particulate matter, the sector contribution is the exact contribution. For nitrogen dioxide, providing an exact contribution is impossible because of the chemical interaction with ozone.

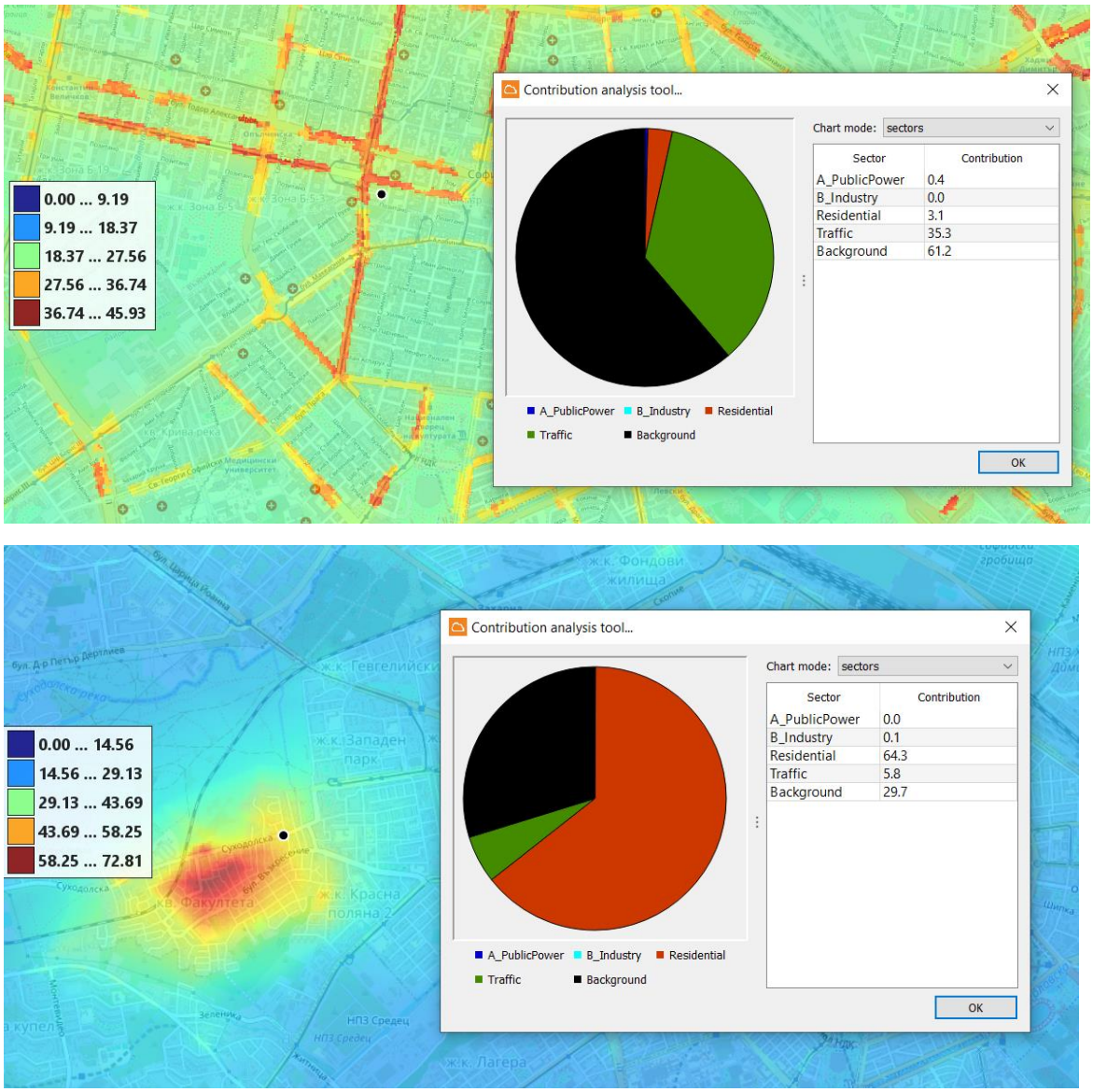

Figure 60: Sector contribution in Sofia (based on the air pollution model chain relying on the Copernicus data, supplemented with local data for the downscaling of the emissions). The figures show the relative contribution of the different emission sectors to the total concentration at the location of the black dot on the map, for NO_2 (top figure) and $PM_{2.5}$ (bottom figure). The following sectors are considered: traffic (green), public power (blue), industry (light blue, no contribution at the locations shown), residential (red) and the background concentration (black).

8.3 Evaluation

8.3.1 Validation of the results

We have evaluated the quality of the air quality application for the three cities under consideration, by comparing the modeled concentrations with air pollutant measurements.

We use the measurements of the official air pollution monitoring networks6 that have to be operated by all European countries according to the Ambient Air Quality Directive (Directive 2008/50/EC). The measurements are reported to the European Environmental Agency, which provides open access to the measurements on its portal (viewer on https://www.eea.europa.eu/data-and-maps/dashboards/air-quality-statistics, data access via http://aidef.apps.eea.europa.eu/). Because the Directive anchors the techniques and quality control of these measurements, the time series contains only validated results, for which the maximal measurement uncertainty has been fixed.

We focus on the validation of the annual mean concentrations of nitrogen dioxide and particulate matter, and, in addition, we also consider the time profiles of the nitrogen dioxide concentrations for the front-runner city Sofia.

8.3.1.1 Annual mean concentrations

The scatterplots with validation results for the official EEA measurement locations are provided in the figures below, and the accompanying validation statistics are provided in the table below. Note that the measurement network in the three cities is vastly different, which might also influence the validation results. Especially the network in Sofia is very scarce, as all stations are located at urban background locations that are not heavily influenced by the emissions sources explicitly treated in the modelling. A clear-cut street canyon and /or traffic measurement stations is for instance missing, and therefore we can only validate the results of the CAMS-IFDM model chain, and not of the street canyon module OSPM. The network for nitrogen dioxide is somewhat more extensive in Bristol and Ostrava, as the network in these cities has a much larger variety in type of measurement locations (urban background, open location at a major road, street-canyon location). On the other hand, the network for particulate matter in Bristol is very small, as there are only two measurement stations.

6 In addition, we have done some test using the measurements of local networks, when available. These networks are mostly using less expensive and less accurate sensors. The uncertainty of these measurements is therefore much higher, which makes them less suited for a validation campaign. Within the current study, we considered additional measurements for Bristol, for which passive sampler measurements for NO2 are available via the open data portal of the city (https://opendata.bristol.gov.uk/explore/?q=air+quality&sort=modified), and for Sofia. Although the scatter is (even) larger for the validation using these local networks, the concluding remarks do not change.

The quality of the air quality application clearly differs across the three cities. Best results are obtained for Ostrava, while the model results clearly underestimate the concentrations and the spatial gradient for both pollutants in Sofia and Bristol.

In Ostrava, the CAMS results only provide a correct estimate for the urban background measurement station (both for nitrogen dioxide and particulate matter), while these CAMS results clearly underestimate the stations located in areas with high residential emissions (for particulate matter) and traffic emissions (for nitrogen dioxide, and, to a lesser extent, for particulate matter). These results are to be expected, because the CAMS model only provides concentrations on a relatively low resolution, and because it does not include the local sources with a high resolution, which in the end leads to an underestimation of local pollution peaks. Adding the Gaussian dispersion model IFDM improves the validation results, but there is still an underestimation, especially for the measurement location in a narrow street-canyon. For that specific location, adding the street-canyon module OSPM further improves the model results, mostly for nitrogen dioxide. These results indicate that simulation air pollution on a street-level resolution requires a model chain that includes a street-canyon module, a finding that has been echoed before in the air quality modelling community.

Even with the inclusion of a street-canyon module, the model chain is still underestimating the concentrations near measurements stations that are heavily influenced by traffic emissions, and it is still underestimating the spatial gradient in the domain. For this specific domain, the main issue seems to be an underestimation of the emissions, with especially underestimations of the traffic emissions near the measurement stations.

Similar effects are observed in the Sofia and Bristol, but they are much more pronounced. In Sofia, the model chain is underestimating the measurements at all locations, and it is clearly underestimating the spatial gradients as well, both for particulate matter and nitrogen dioxide. The results point at issues both with the urban background concentration of CAMS, which clearly underestimates the actual background concentration, and with the traffic and residential emissions, which clearly do not catch the spatial gradient observed in Sofia. It is furthermore difficult to assess the quality of the model chain, as there is no street canyon measurement station. The results for Bristol are very similar to the results for Sofia, with a large underestimation of the background concentrations and traffic emissions, especially for the locations with the highest measured concentrations.

These results are also backed up by the validation statistics in the table below. We therefore conclude that the accuracy of the CURE air quality maps is rather low, especially for Sofia and Bristol, whereas the accuracy will be somewhat better for Ostrava. Policy information (health impact, sector contribution) based on the maps hence comes with a substantial uncertainty, and should be treated with great care.

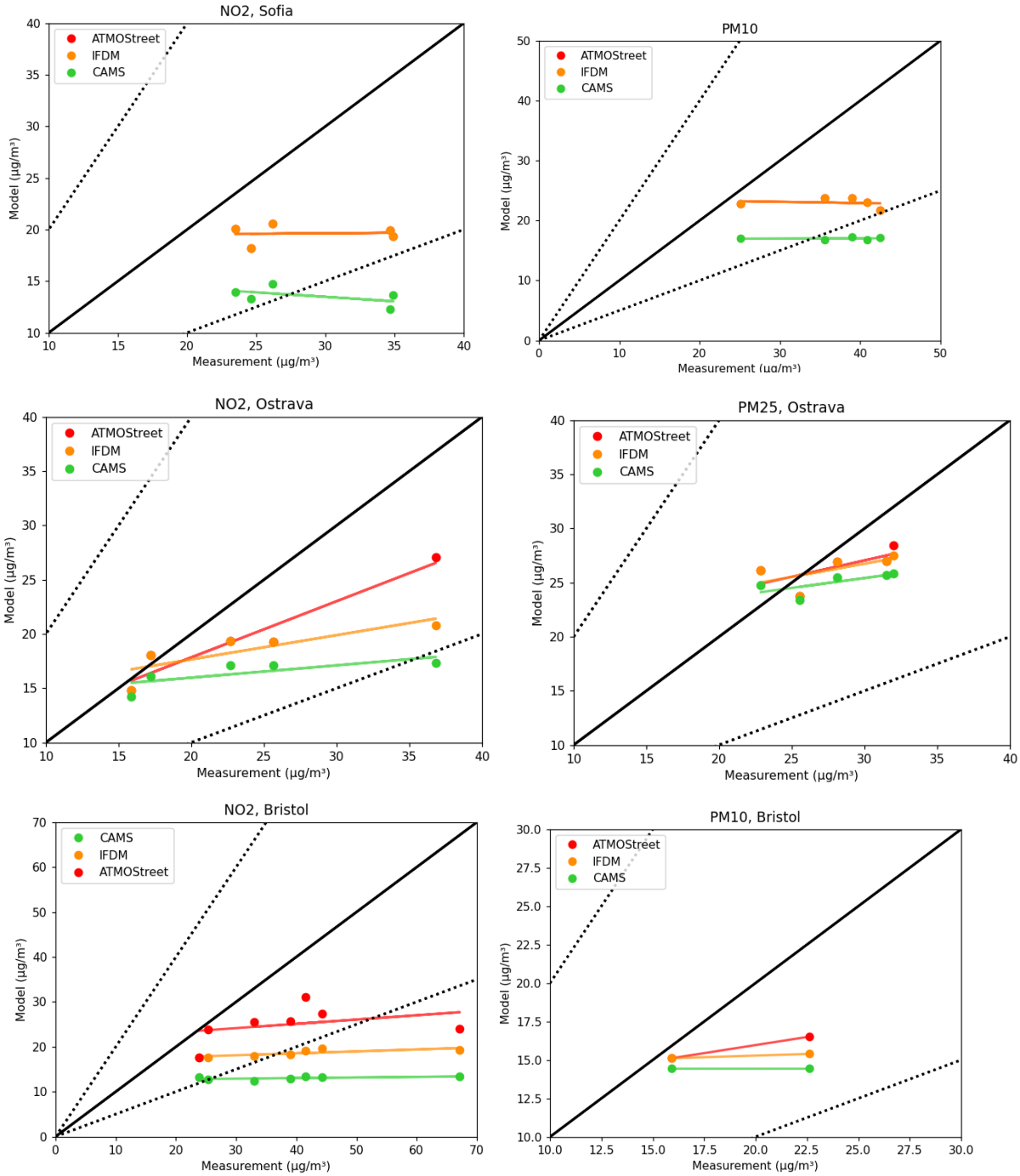

*Figure 61. Scatterplot showing the modeled concentration as a function of the measured concentrations for all sampling locations for NO2 (left figure) and particulate matter (right figures, either PM2.5 or PM10, depending on availability). Different colors depict the CAMS background model (green), the CAMS-IFDM model which combines the background model with a Gaussian dispersion model (orange) and the ATMO-Street model which also includes street-canyons (red, only shown for locations for which ATMO-Street differs from CAMS-IFDM). Figures are provided for Sofia (top row), Ostrava (middle row) and Bristol (bottom row). Note that there are no street-canyon measurement stations in Sofia, and hence the results of ATMO-Street always coincide with the IFDM results. The colored lines indicate the linear regression, the black line indicates the 1-1 resolution, and the dotted lines indicate the interval [0.5 * measurements; 2 * measurements].*

Table 10. Validation statistics for the ATMO-Street model chain (including the street-canyon module, if applicable) for the three cities under consideration.

	Sofia		Ostrava		Bristol	
	NO2	**PM**	**NO2**	**PM**	**NO2**	**PM**
R^2	0	0.03	0.92	0.61	0.25	0.21
Bias (µg/m³)	-9.1	-13.6	-3.9	-6	-26	-3.5
RMSE (µg/m³)	10.4	15	5.4	3.9	29	4.3
Linear Coefficient of regression	0.0	0.0	0.51	0.34	0.01	0.2

8.3.1.2 Temporal cycles in Sofia

The cycle analysis checks the time profiles modeled by the ATMO-Street model chain. We only consider NO_2, and focus on yearly, weekly and daily cycles. We provide cycles for four distinct locations in Sofia. The results however indicate that the temporal cycles are more or less the same for all the stations under consideration.

Figure xx shows the daily, weekly and monthly cycles. The results anew indicate significant bias (as explained in the previous section), as the model results clearly underestimate the measurements for all locations. On the other hand, the models correctly catch the general trends in the measured cycles. The agreement is the best for hourly cycles, for which both the height and the timestamp of the bidaily peak (owing to traffic emissions and meteorology) are correctly modeled. For the monthly profiles, the general trend is correctly modeled (higher concentrations in the winter), but the extent of the seasonality is underestimated. Finally, the weekly pattern is rather small in both the measured and the modeled concentrations, but the model correctly catches the general trend (lower concentrations in the weekends compared to the weekdays).

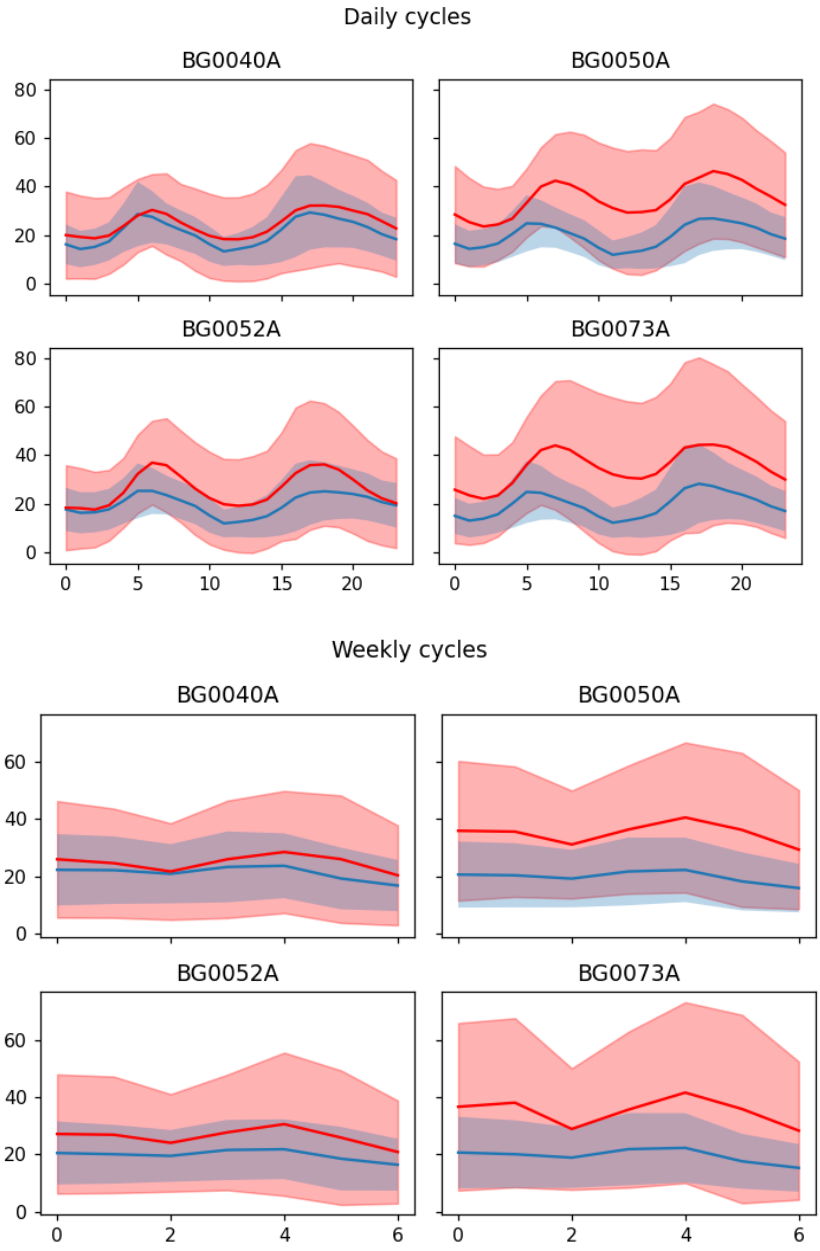
Daily cycles
BG0040A
BG0050A
BG0052A
BG0073A
Weekly cycles
BG0040A
BG0050A
BG0052A
BG0073A

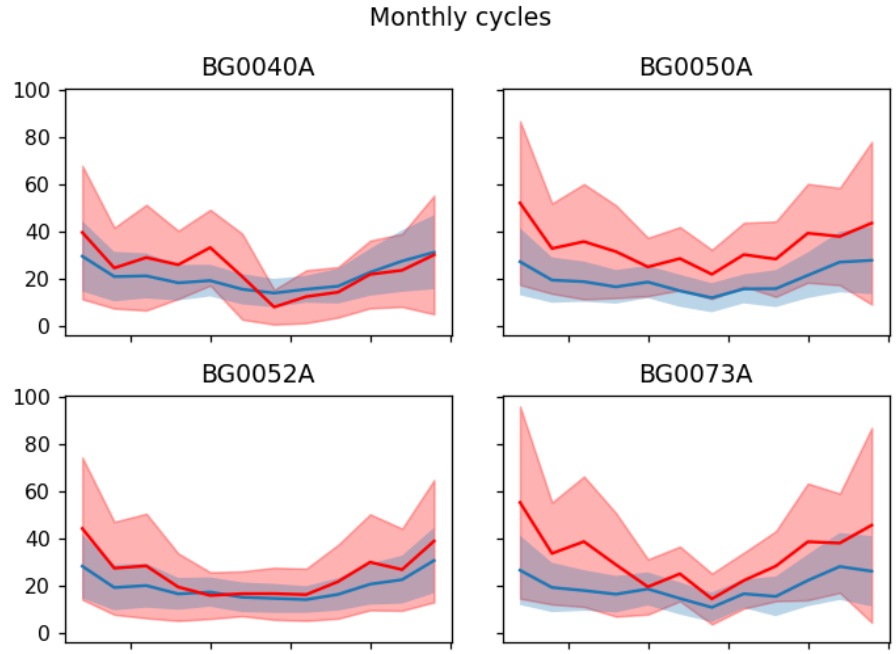

Figure 62. Validation of the hourly, daily and weekly cycles for selected stations in Sofia. The plots show the mean concentration (in µg/m³) as a function of the hour of the day (upper figure), as a function of the day of the week (middle figure, from Monday (day 0) to Sunday (day 6)) and as a function of the month of the year (bottom figure, from January to December). The figures show the concentration for the model data (blue) and the measurements (red). The lines indicate the average concentration per month, while the shading indicates the range [mean – standard deviation; mean + standard deviation].

8.3.2 General conclusions on the use of Copernicus products for high resolution air quality mapping

Based on the evaluation provided in the previous section, we can draw the following general conclusions regarding the use of the Copernicus products for high resolution air quality modelling.

First and foremost, it is very difficult to bridge the gap in resolution between the Copernicus data and the input data required for air quality modelling on a street-level scale. The resolution gap is especially problematic for emission data. Traffic and industrial emissions are provided on a resolution of 0.05 degree by 0.1 degree (approximately 5 by 10 kilometers) in the latest CAMS products, whereas high resolution air quality models require data per street for traffic emissions, and per neighborhood or per house (at least 1km by 1km) for residential emissions, to correctly model the impact of the local emissions. We have attempted to bridge the resolution gap using downscaling routines based on open-source data (such as OpenStreetMaps), but the validation indicates that the gap has only partially been bridged. The gap in resolution is, to a lesser extent, also present for background concentrations, as highlighted by the validations, as for all three cities the background concentrations are underestimated by the CAMS reanalysis results. No resolution gap is observed for

meteorological data, as, for the three cities under consideration, both the temporal and the spatial the resolution of ERA5 data suffices7.

The impact of this resolution gap becomes especially apparent when the validations of the CURE air quality maps (described in the previous section) are compared with validations in which the high-resolution air quality model has been set-up using local bottom-up datasets. VITO has been using the ATMO-Street air quality model chain for several countries and regions in Europe (Croatia, Slovakia, Poland, Hungary, Ireland, Walloon Region, Flanders...). In each of these cases, the model set-up is based on the best local datasets (e.g. traffic data from a traffic model, residential data from a bottom-up residential emission inventory). Validation campaigns for these bottom-up air quality maps clearly outperform the validation studies for the CURE maps. An outstanding example is the Curieuzeneuzen validation in Flanders, in which the model results are compared with the measurements of an extensive, citizen science validation campaign using 20.000 passive sampler8.

Apart from the resolution, some important datasets are missing in the Copernicus inventories. A detailed dataset with the ground plans of buildings (in Polygon format) is currently missing. OpenStreetMaps provides an open-source alternative, but the data quality of this collaborative dataset varies strongly across Europe (and even within a single country there might be a large variation in quality). Additionally, building heights are available at a sufficient resolution in the Urban Atlas of the CLMS, but only for the capital cities in Europe. For other cities, one either has to use local data, or use a simple estimate of the building height.

A simple solution to the resolution gap might be including local datasets in the downscaling of the emissions (e.g. including traffic data or location of residential heating devices) and the background concentrations (e.g. including local, higher resolution chemical transport models). A prototype of this improved downscaling has been implemented for Sofia. Unfortunately, we have not been able to test this procedure in full detail, because better downscaling data is unavailable for the background concentrations and the traffic sector (no actual traffic data is available, only road capacity data), and because measurement stations close to the neighborhoods with a lot of gas heating devices are missing, which hinders the validation of the improved downscaling for the residential emissions in Sofia.

In general, we conclude that the resolution gap between the Copernicus products and the required input data for a street-level air quality model chain is currently very large, and that consequently the quality of the resulting air quality maps is rather low. Policy information (health impact, sector contribution) based on the maps hence comes with a substantial

7 For cities in mountainous areas or in steep valley, also meteorological data with a higher resolution might be required.

8 https://doi.org/10.1016/j.atmosenv.2022.118946

uncertainty, and should be treated with great care. To further improve the quality of the air pollution maps, either CAMS emission products with a higher resolution should become available, or more involved downscaling methodologies should be developed. Until these products are available, local datasets provide the best alternative for street-level model chains for specific cities. These datasets can however not be used to set-up a pan-European street-level air quality service, because there is no standardization amongst these datasets, and because the datasets might be missing for many locations in Europe. We hence conclude that a pan-European, street-level (i.e. including street canyons) air quality modeling service is currently out-of-scope, and that significant developments are required before such a service could provide accurate results.

9 AP08 URBAN THERMAL COMFORT

9.1 Data & Methodology

To study the urban microclimate, VITO has developed the urban boundary layer climate model "UrbClim", designed to cover individual cities and their nearby surroundings at a very high spatial resolution (De Ridder et al., 2015). UrbClim consists of a land surface scheme, coupled to a 3-D atmospheric boundary layer module. The land surface scheme is based on the soil–vegetation–atmosphere transfer scheme of De Ridder and Schayes (1997), but is extended to account for urban surface physics. The model has been applied to and validated for over 10 cities worldwide (De Ridder et al., 2015 ; Garcia-Diez et al., 2016 ; Lauwaet et al., 2015 ; Lauwaet et al., 2016 ; Zhou et al., 2016). The model operates at a typical horizontal resolution of 100m, and provides the local meteorological input variables for the high resolution thermal comfort module.

To set up the 100m resolution model simulations, several Copernicus input datasets are needed (Table 11). The spatial distribution of land cover types, needed for the specification of required land surface parameters, is taken from Urban Atlas (2018), and converted to relevant classes for the UrbClim model. Terrain height is specified by the EU-DEM map. The UrbClim model needs also information on the soil sealing and vegetation cover fraction in each grid cell. The percentage urban land cover is specified using the Imperviousness data from CLMS, and the vegetation cover fraction from the NDVI data set. More details about these data sets can be found in D2.1 of the CURE project. The model is driven by large-scale meteorological data from the C3S ERA5-reanalysis. The model output consists of hourly 2m air temperature, humidity and wind speed fields, as well as land surface temperatures.

Table 11. *Overview of the input datasets for the 100m resolution background UrbClim simulations.*

Copernicus service	*Dataset*	*Usage*
CLMS	Urban Atlas	Specification of land use classes
CLMS	EU-DEM	Specification of terrain height
CLMS	Imperviousness	Specification of soil sealing % in grid cell
CLMS	NDVI	Specification of vegetation % in grid cell
C3S	ERA5	Large-scale meteorological input data

These data give a good overview of the spatial distribution of air temperatures (which don't vary much over short distances) and the Urban Heat Island effect of a city. However, air

temperatures don't tell the complete story of heat stress experienced by citizens. Also the radiation load (both shortwave and longwave), humidity and wind speed are important factors to quantify human thermal comfort. An indicator that takes all these variables into account is the Wet Bulb Globe Temperature (WBGT), which is calculated as follows:

$$WBGT=0.7\times Tw+0.2\times Tg+0.1\times Ta$$

with Tw = the wet bulb temperature, Tg = the black globe temperature and Ta= the air temperature.

The Wet Bulb Globe Temperature has a long tradition of being used as a thermal comfort index and is the ISO standard for quantifying thermal comfort (ISO, 1989). It is currently in use by a number of bodies including the US and UK Military, civil engineers, sports associations and the Australian Bureau of Meteorology (Willett and Sherwood, 2012). It is the only heat index to have known thresholds based on a large number of observations, developed by the U.S. Army (2003) (Table 12). The WBGT can be measured easily with rather cheap equipment, making it an ideal indicator for model validation and citizen science campaigns to raise awareness about heat stress issues.

Table 12. *Heat stress category limits of the U.S. Army (2003).*

Heat Stress Category	WBGT [°C]
1	≤ 25.6-27.7
2	27.8-29.4
3	29.4-31.0
4	31.1-32.1
5	≥ 32.2

By combining the standard output of VITO's UrbClim model with detailed radiation calculations based on 3D building and vegetation data, it is possible to calculate the WBGT with a very high spatial resolution (Lauwaet et al. 2020). The methodology used by VITO is adopted from the paper by Liljegren et al. (2008), the recommended method to calculate outdoor WBGT values (Lemke and Kjellstrom 2012). As input for these calculations, additional Copernicus data sets are needed, which are listed in Table 13. Figure 63 shows an example of the high resolution input data for the city center of Copenhagen.

Table 13. Overview of the input datasets for the high resolution WBGT module.

Copernicus service	*Dataset*	*Usage*
CLMS	Urban Atlas Street Tree layer	Specification of tree locations in cities
Copernicus Data Warehouse	Very High Resolution land cover map	Specification of land use classes

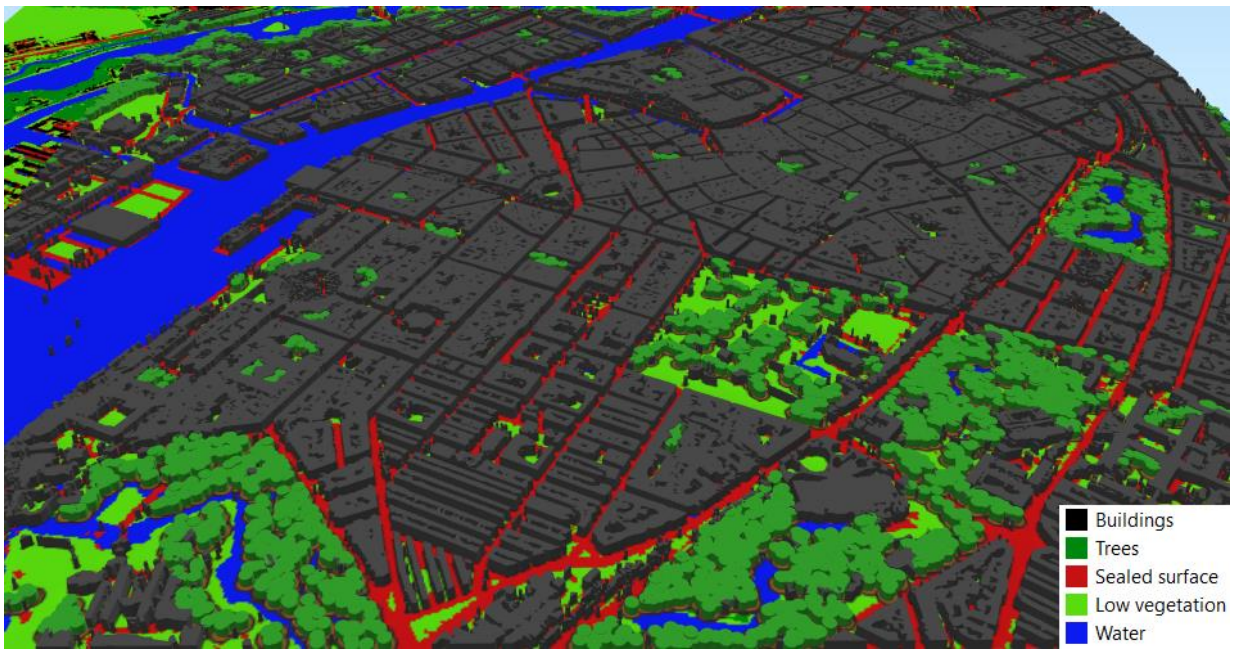

Figure 63. Detailed land cover input map for the city of Copenhagen. Buildings are assumed to have a height of 20m, and trees have a height of 15m.

When assessing WBGT values, it is best to focus on typical hot summer days, because it is during these type of days that people will suffer from heat stress issues. The CURE Thermal Comfort Application delivers WBGT maps for a selected hot summer day.

A complete overview of the whole modelling chain is shown in Figure 64.

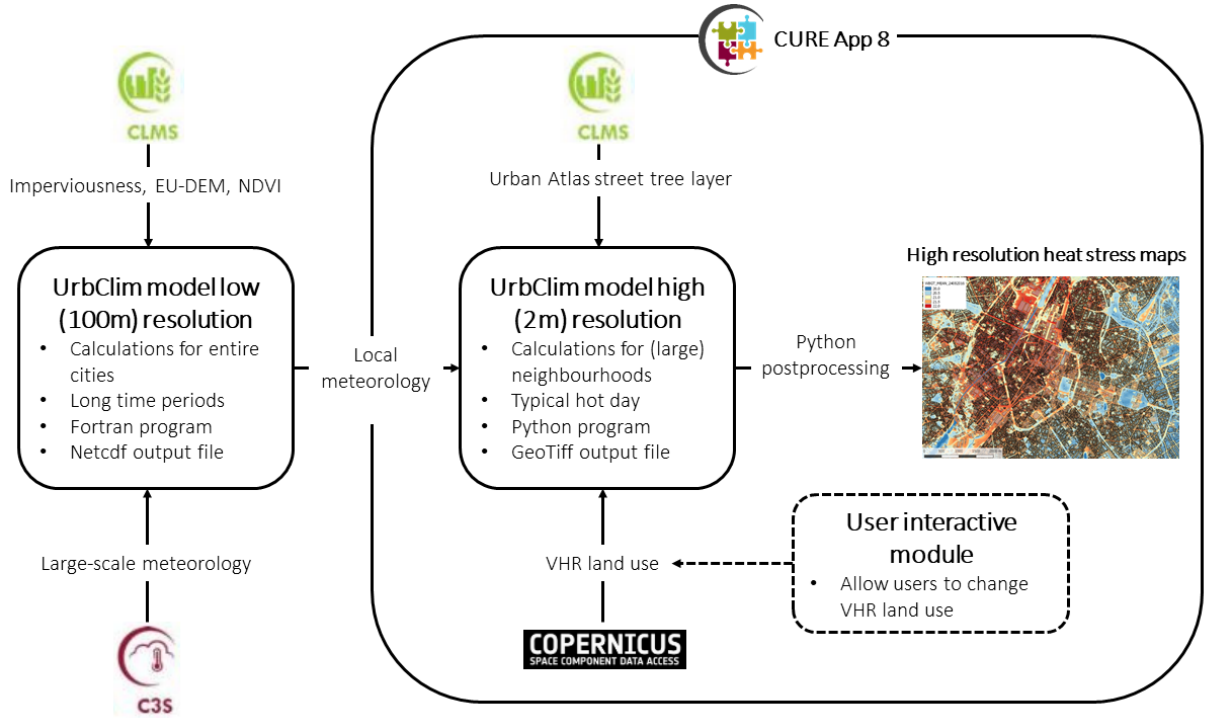

Figure 64. Overview of the Thermal Comfort Application.

The WBGT maps of this application will be made available to the users of the CURE system through the CURE portal. This will allow stakeholders (e.g. urban planners and city administrations) to identify hotspots and give them insight in the local variation of heat stress with a high level of spatial detail. From these maps, overview statistics can be calculated (e.g. city quarter averages, area above/below defined threshold values). Furthermore, a set of potential heat stress adaptation measures (e.g. green roofs, urban trees, soil unsealing,…) has been simulated with the application for each city, enabling the users to assess the effectiveness of these measures for their specific city. Finally, the dockerization of this application will potentially allow users to modify the input land cover map and upload their own land use scenarios (e.g. development plans) from which new WBGT maps will be calculated instantly. Working out an interactive user platform for AP08 is not foreseen in the CURE project, but having the docker container ready should allow to develop this update quickly and at a low cost in a post-project phase.

9.2 Results

9.2.1 Wet Bulb Globe Temperature maps

The CURE Urban Thermal Comfort Application delivers Wet Bulb Globe Temperature maps (Geotiff format) for a typical hot summer day for 4 European cities: Copenhagen, Ostrava, San Sebastian and Sofia. Daily maximum, minimum and daily mean WBGT maps are calculated from the hourly model output of the application. When assessing the WBGT values, it is good to keep in mind that the values are typically a few degrees lower than regular air temperature values, and a difference of a few degrees can already have a strong effect on human thermal comfort.

Daily maximum WBGT maps focus on the hottest hours of the day, when shading is crucial to lower the local heat stress. The variability in the temperatures is typically at least 3°C, up to 6°C (e.g. in San Sebastian) if there are large height differences. From the example maps shown below it is clear that forested areas are the coolest locations in cities, as the trees provide shade and cool the air through evapotranspiration. Water areas can also provide some cooling during the hottest hours of the day. Open areas without shade from trees or buildings are the hottest locations. There is typically not much difference in the maximum temperatures between the city center and the surrounding areas as the urban heat island effect is usually low during daytime.

The daily minimum WBGT maps focus on the nighttime temperatures, when the urban heat island effect is at its strongest. The variability in the temperatures is a bit lower than for the maximum temperatures, and is typically around 2 to 4°C. Open grassland areas and forested areas are the coolest locations during the night, and the bigger they are, the larger the cooling effect. Water areas often keep a high temperature during the night, aggravating the urban heat island problem. The sealed areas in the cities are the hottest locations.

Finally, the daily mean WBGT maps show a time-average of the heat stress situation. All the maps for the 4 cities that are covered by AP08 will be made available through the CURE portal.

Copenhagen – 30 June 2019

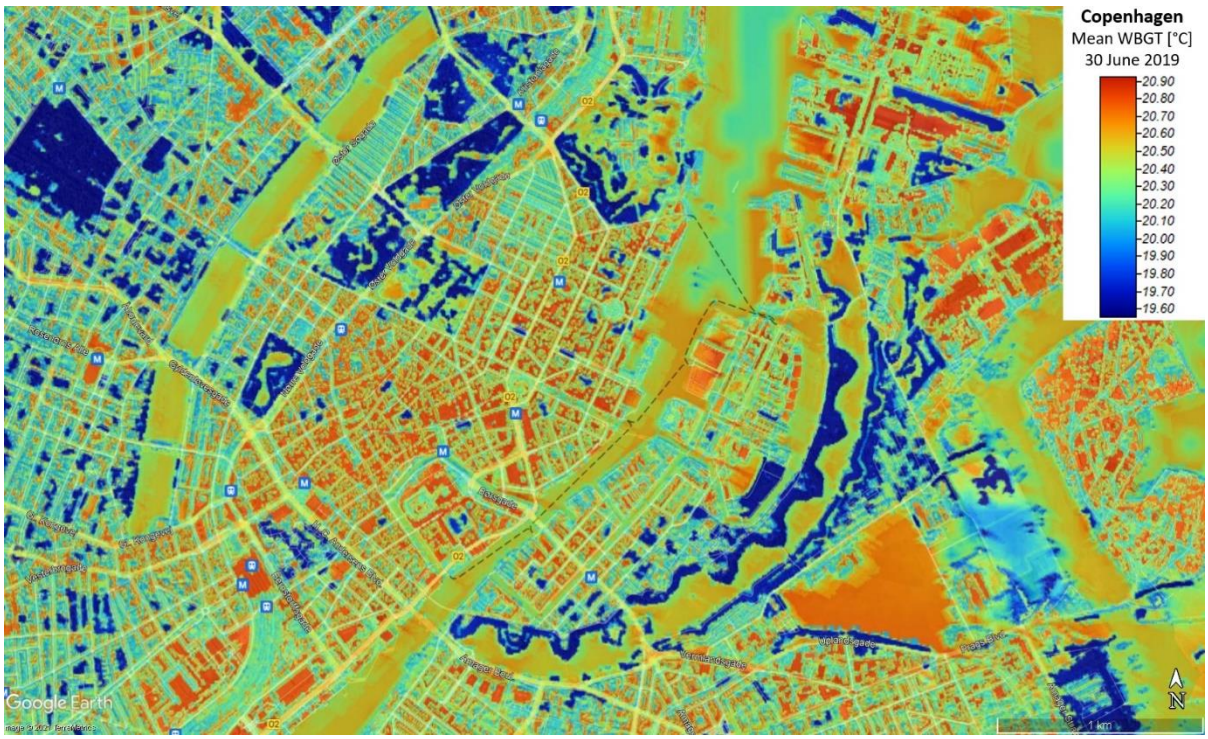

Figure 65. *Daily mean Wet Bulb Globe Temperature in Copenhagen (Denmark) for 30 June 2019.*

Sofia – 2 July 2019

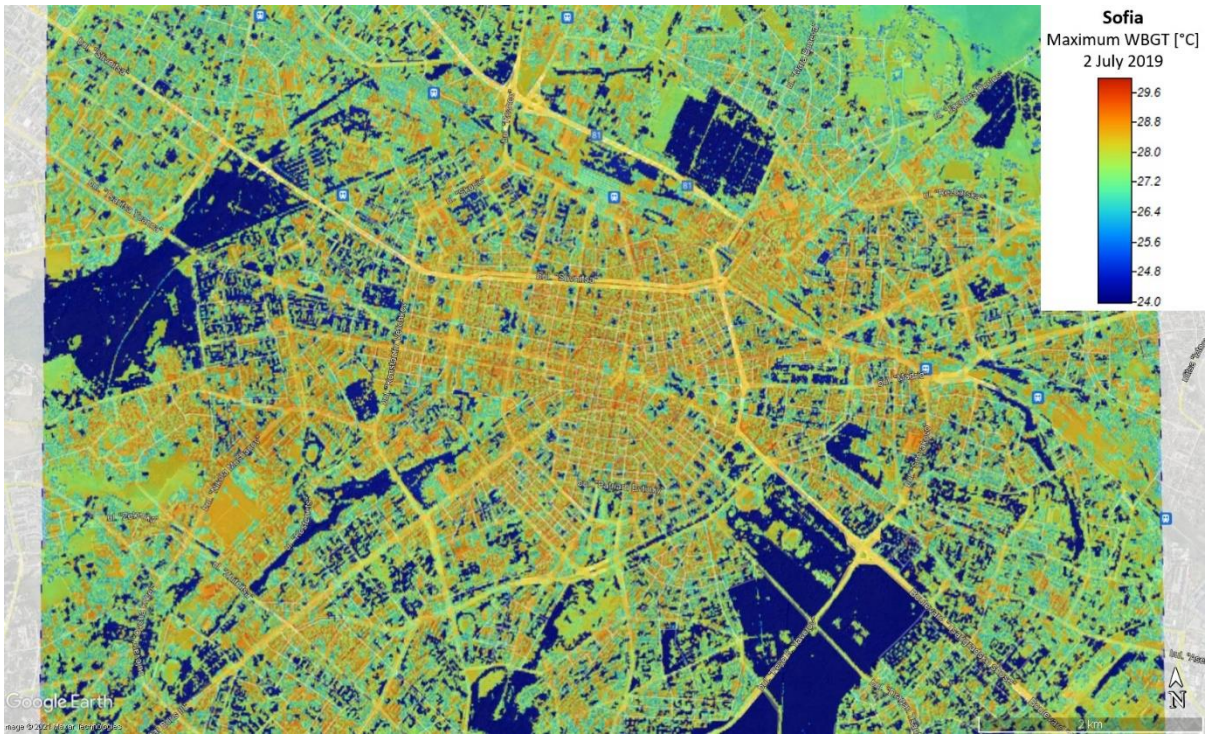

Figure 66. *Daily maximum Wet Bulb Globe Temperature in Sofia (Bulgaria) for 2 July 2019.*

Ostrava – 30 June 2019

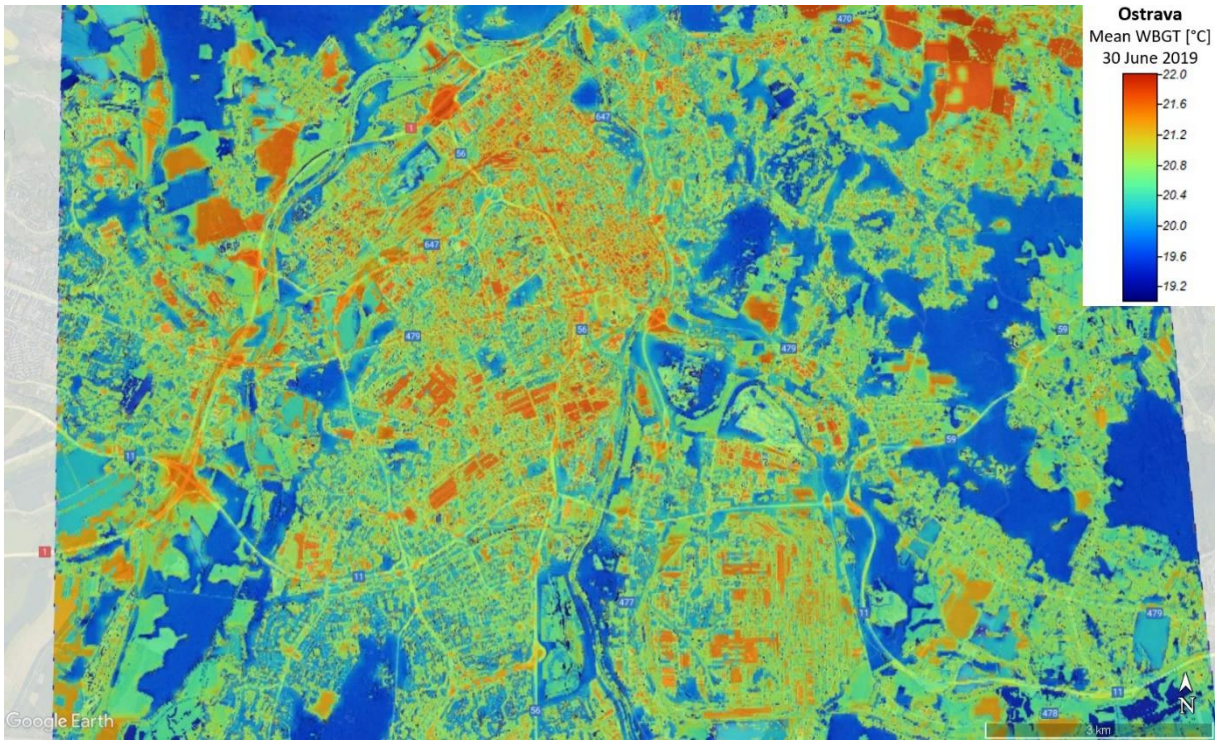

Figure 67. *Daily mean Wet Bulb Globe Temperature in Ostrava (Czech Republic) for 30 June 2019.*

San Sebastian – 23 July 2019

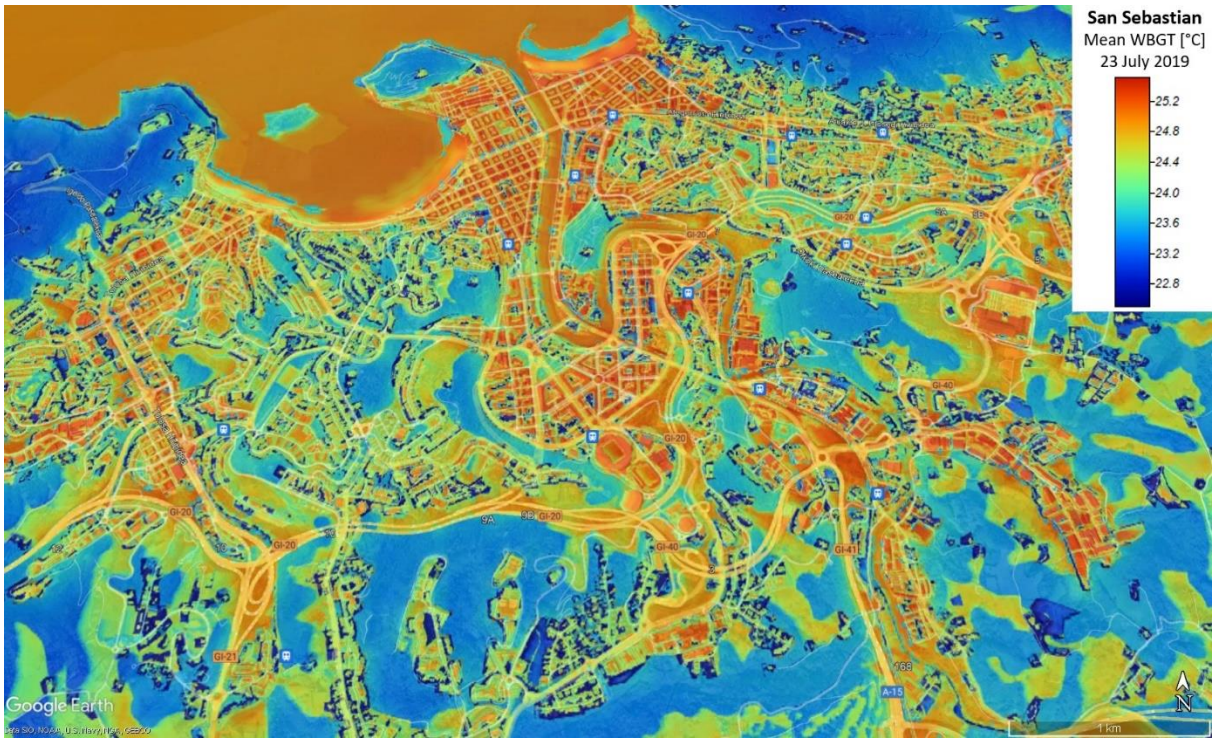

Figure 68. *Daily mean Wet Bulb Globe Temperature in San Sebastian (Spain) for 23 July 2019.*

9.2.2 Adaptation scenario analysis

The CURE Urban Thermal Comfort Application not only shows heat stress maps for the current situation, but also assesses the effect of a number of potential climate adaptation measures. We have made a selection of commonly used nature-based solutions to cool cities in Europe: green roofs, using white building materials (albedo of 0.3), unsealing the soil, planting trees and a combination of all these measures (maximum scenario). The measures have been applied in a drastic way to show the maximal potential impact. For the green roofs, all roofs in the urban area are assumed to be green, whereas all building materials are assumed white in the light materials scenario. The soil unsealing and tree cover are applied to 50% of the non-building urban area, by selecting the hottest locations based on the daily mean WBGT map. Furthermore, a 'no green' scenario is simulated by removing all green elements from the urban area, to assess the cooling effect of the current vegetation in the cities.

All these results will be made available through the CURE portal, where users will be able to select the city, indicator and scenario they want to visualize. Both the resulting WBGT map and a difference map, comparing the scenario to the reference situation, will be shown. The example below shows the effect of the maximum scenario on the daily maximum WBGT in San Sebastian. The impact of the scenarios is mainly local as the WBGT has a high spatial variability, but the local cooling can be very large (up to 5°C), especially for the daily maximum WBGT.

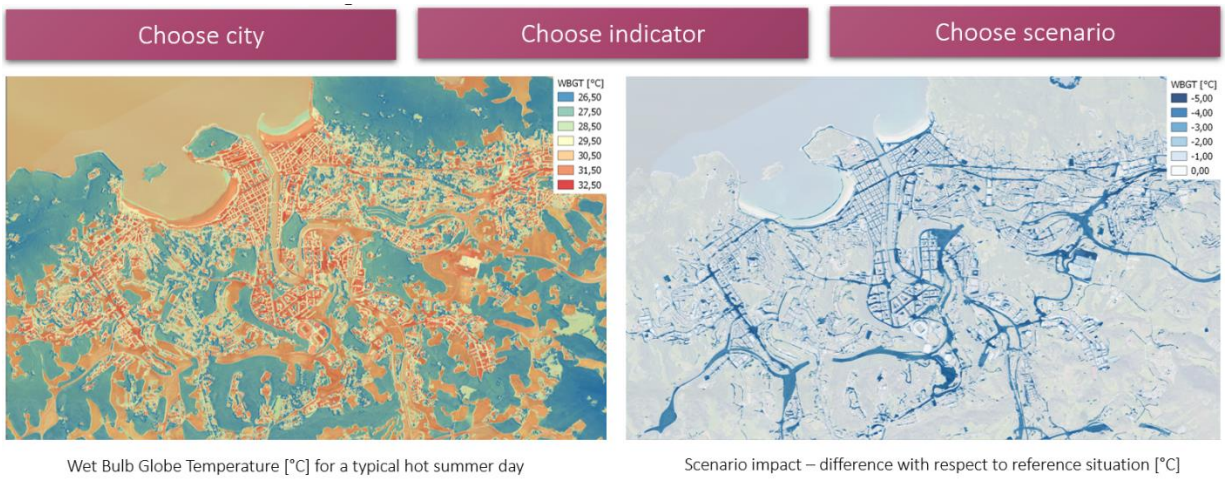

Figure 69. *Example results of AP08 showing the maximum scenario in San Sebastian for the daily maximum WBGT.*

Furthermore, a more in-depth analysis is performed by calculating and comparing statistics for all these scenarios. Average values for the urban area (defined by their Urban Atlas category) of each city are compared to the average rural (non-water) value. An example for the city of San Sebastian is shown below. The differences between the scenarios are typically small as the effects are averaged out over a large area, but they are nevertheless significant. Some measures (light materials, urban trees) mainly have an impact on the daily maximum WBGT, whereas others (green roofs, soil unsealing) mainly have an effect on the minimum temperatures. Overall, it is clear that these type of measures (when drastically implemented) have the potential to cool down cities towards or even below rural heat stress values.

Choose city

Adaptation scenario	Daily maximum WBGT [°C]	Daily minimum WBGT [°C]	Daily mean WBGT [°C]
Reference situation	29.32	20.10	24.19
No green	30.60	20.53	24.93
Green roofs	29.26	19.89	24.10
Light materials	29.19	20.09	24.14
Soil unsealing	29.27	19.90	24.10
Urban trees	28.43	20.15	23.99
Maximum	28.35	19.76	23.80
Rural reference	28.87	19.68	23.99

Figure 70. *Example statistics of AP08 showing the average WBGT values for all scenarios in San Sebastian.*

9.3 Evaluation

The WBGT model has already been validated with a number of dedicated measurement campaigns in Belgium (Lauwaet et al., 2020), and the UrbClim model that serves as the

backbone for the WBGT model has been validated extensively in the past for a large number of European cities (De Ridder et al., 2015 ; Garcia-Diez et al., 2016 ; Lauwaet et al., 2015 ; Lauwaet et al., 2016 ; Zhou et al., 2016). For the simulated cities and hot days in this project, no specific WBGT measurements were available, but we can compare the land surface temperatures of the UrbClim model (which are important for the WBGT calculation) with the LST products of AP01.

For each city, at least 3 LST maps at several moments of the selected hot day are available for the comparison. A visual comparison example for each of the cities is shown below. To perform a more in-depth analysis, the average LST value for different land use categories is calculated, as a pixel-by-pixel comparison between the images is difficult due to the different resolutions and background data of the maps.

For the city of Copenhagen, the LST values between the model and the observations show a good comparison, with a slight overestimation (up to 2°C) of the dense urban and industrial areas, and a slight underestimation (up to 2°C) of the suburban and rural areas. When all data points are plotted together, the results show a strong correlation between the model results and the observations.

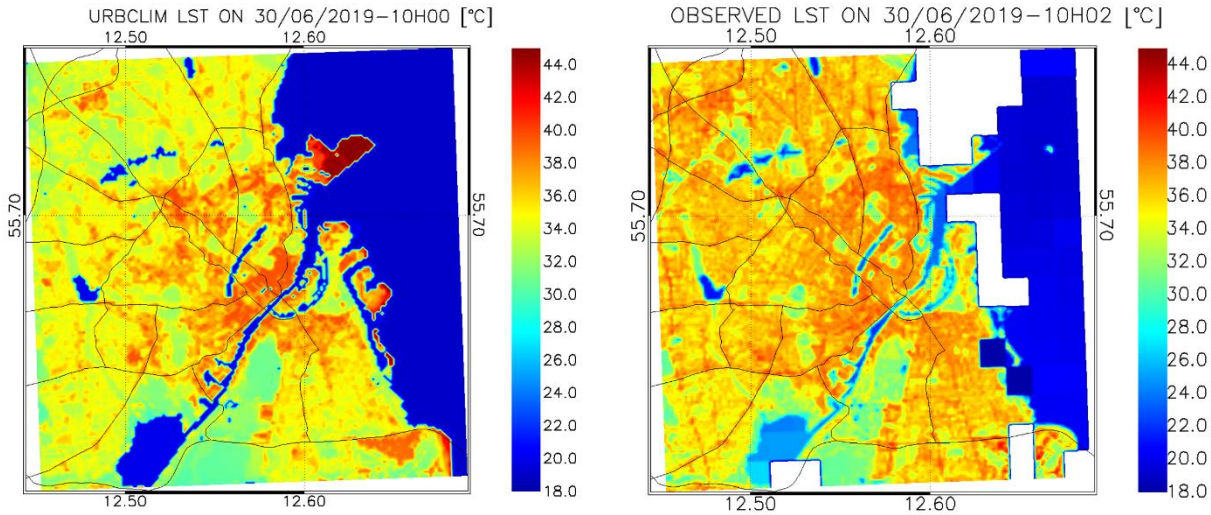

Figure 71. *Comparison between modelled (AP08) and observed (AP01) land surface temperatures in Copenhagen.*

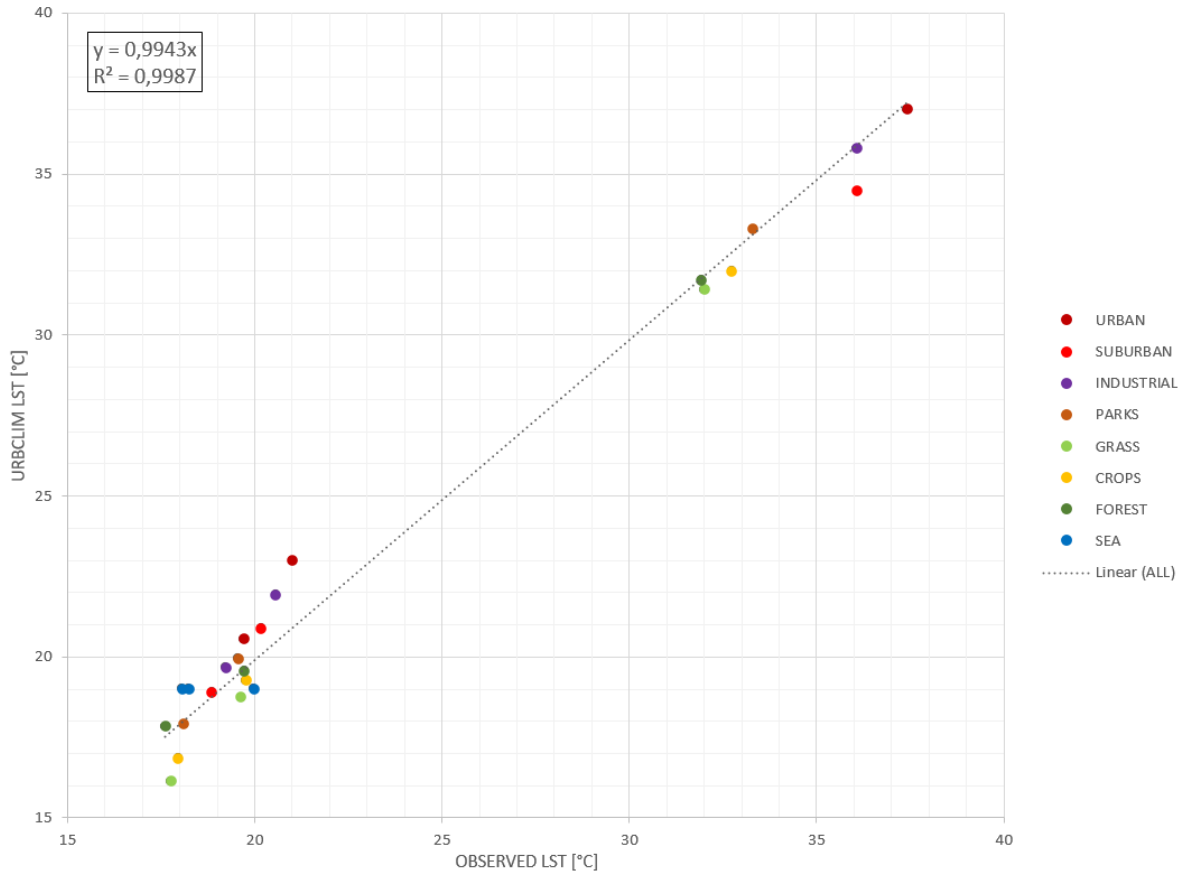

Figure 72. *Comparison between modelled (AP08) and observed (AP01) land surface temperatures per model land use category in Copenhagen.*

For the city of Sofia, a similar tendency to overestimate the dense urban and industrial temperatures and to underestimate the rural values is visible. The differences are in the same range as in Copenhagen (up to 2°C), except for the forest area, which is in the south of the model domain, where the underestimation is much larger. Here, the terrain height effect may play a role in the deviation of the model results. The overall correlation of all data points is still strong however.

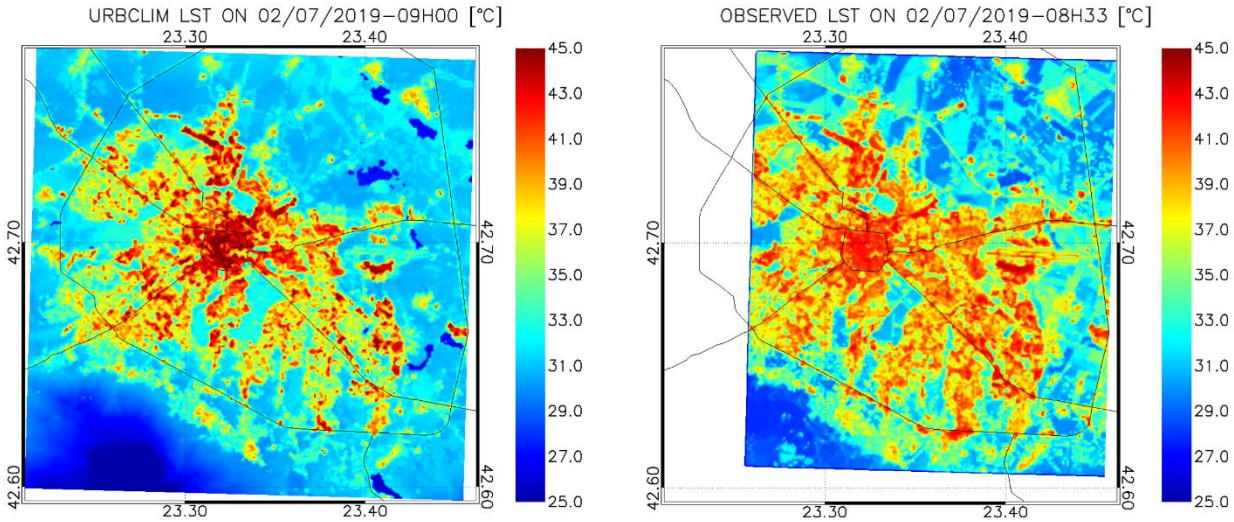

Figure 73. Comparison between modelled (AP08) and observed (AP01) land surface temperatures in Sofia.

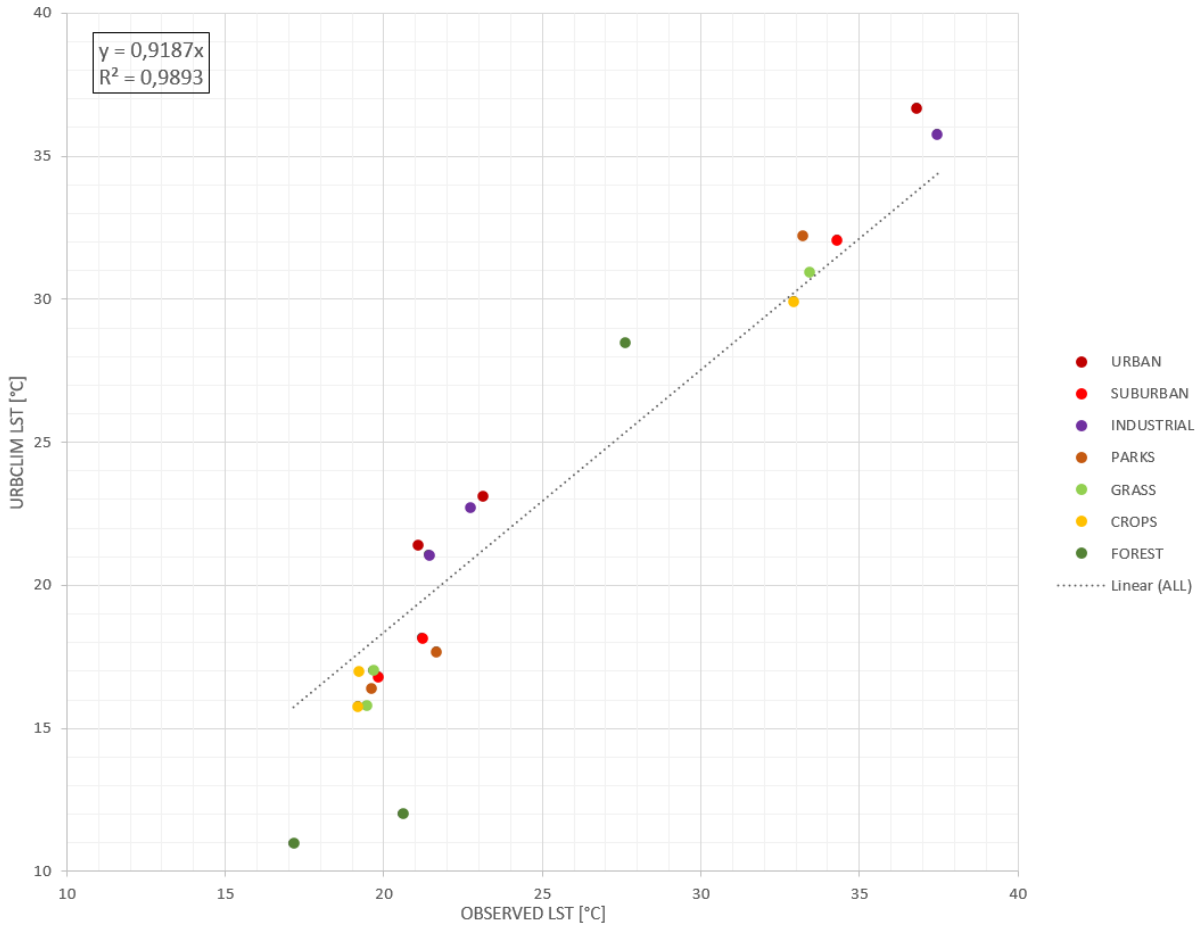

Figure 74. Comparison between modelled (AP08) and observed (AP01) land surface temperatures per model land use category in Sofia.

For San Sebastian, the comparison is somewhat hampered by the fact that the observed LST maps only cover a small part of the model domain, as shown in the example below. For this area, the model results compare well with the observations and the differences are in the same order as for the previous cities.

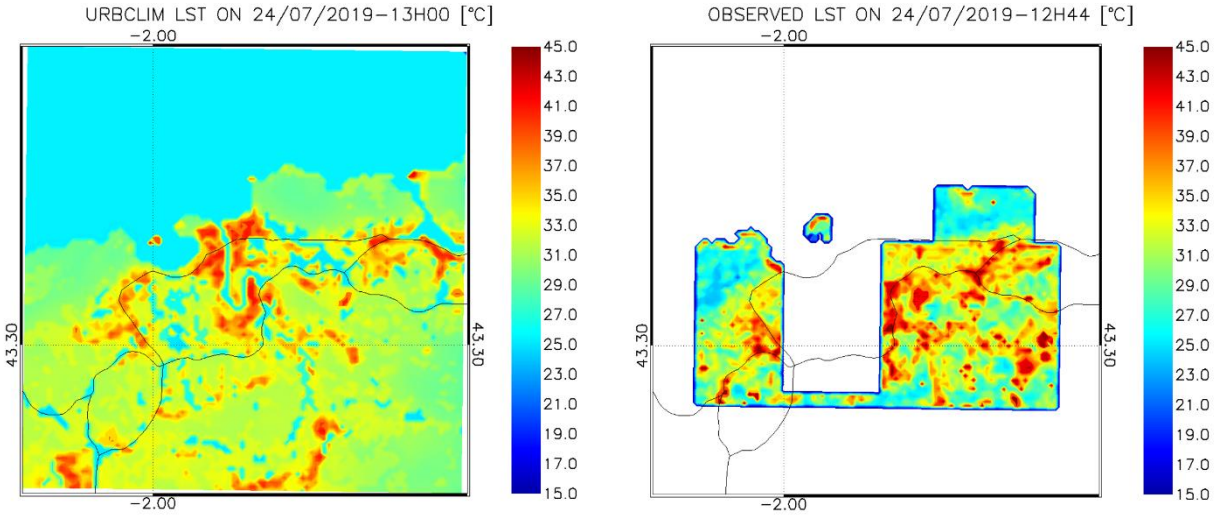

Figure 75. *Comparison between modelled (AP08) and observed (AP01) land surface temperatures in San Sebastian.*

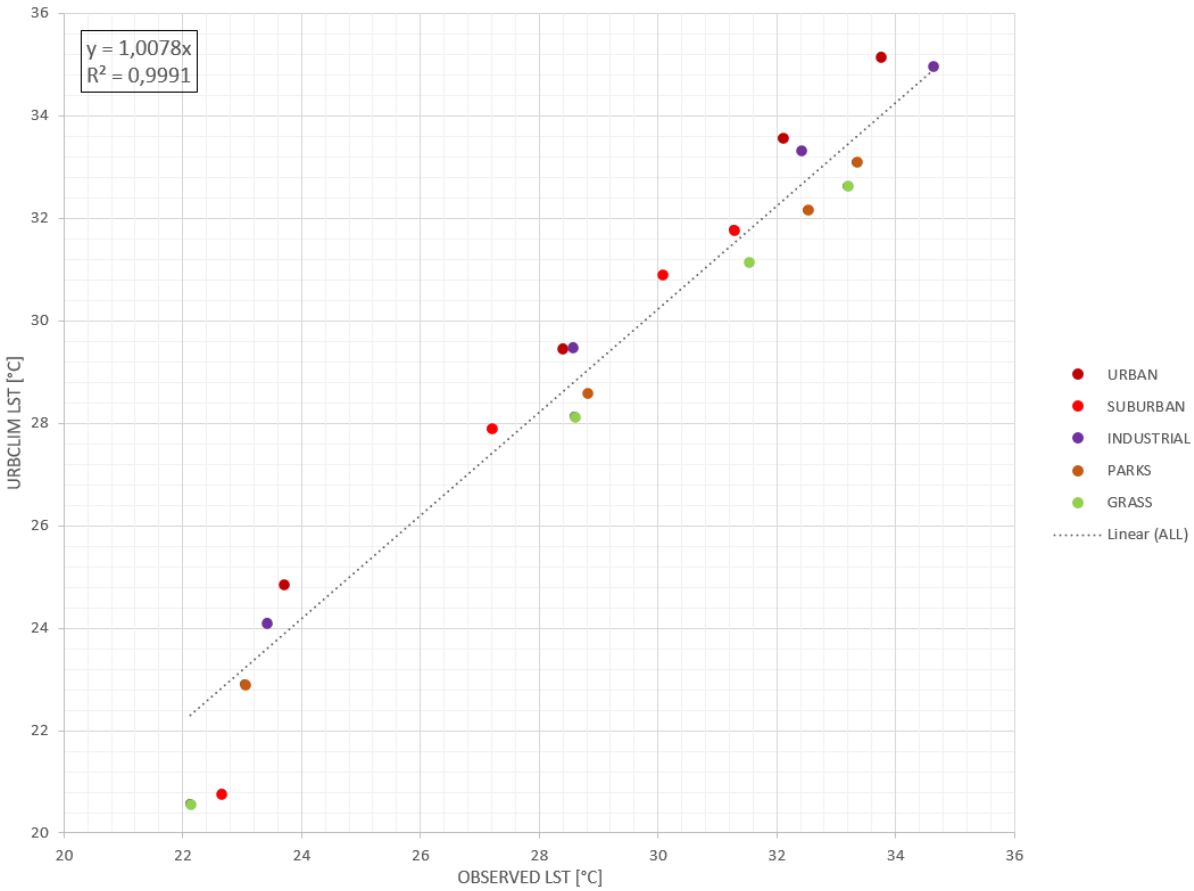

Figure 76. Comparison between modelled (AP08) and observed (AP01) land surface temperatures per model land use category in San Sebastian.

For the city of Ostrava, a similar tendency to overestimate the dense urban and industrial temperatures and to underestimate the rural values is visible. The differences are a little larger than for the other cities, especially the underestimation of the rural area.

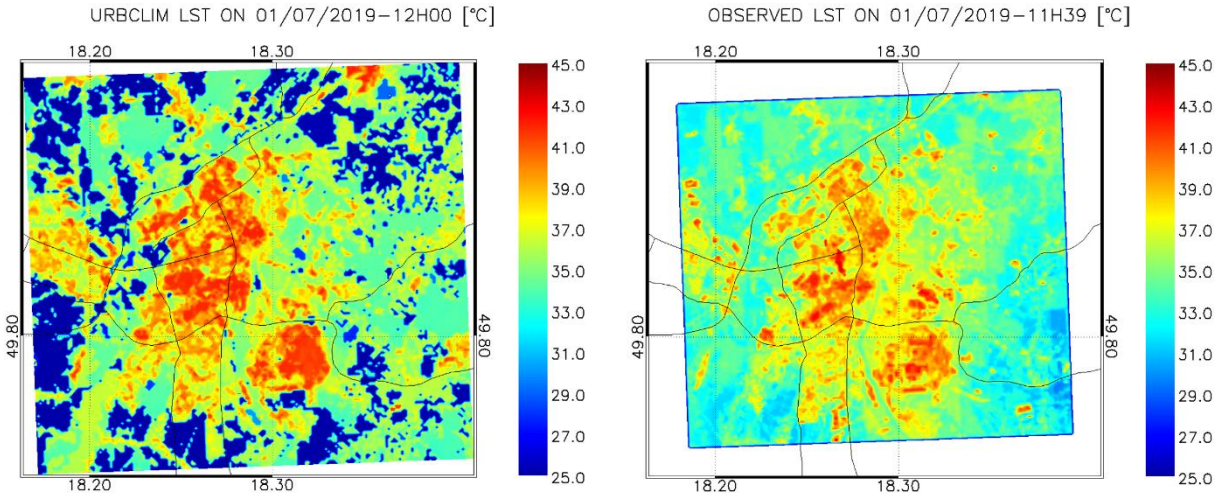

Figure 77. Comparison between modelled (AP08) and observed (AP01) land surface temperatures in Ostrava.

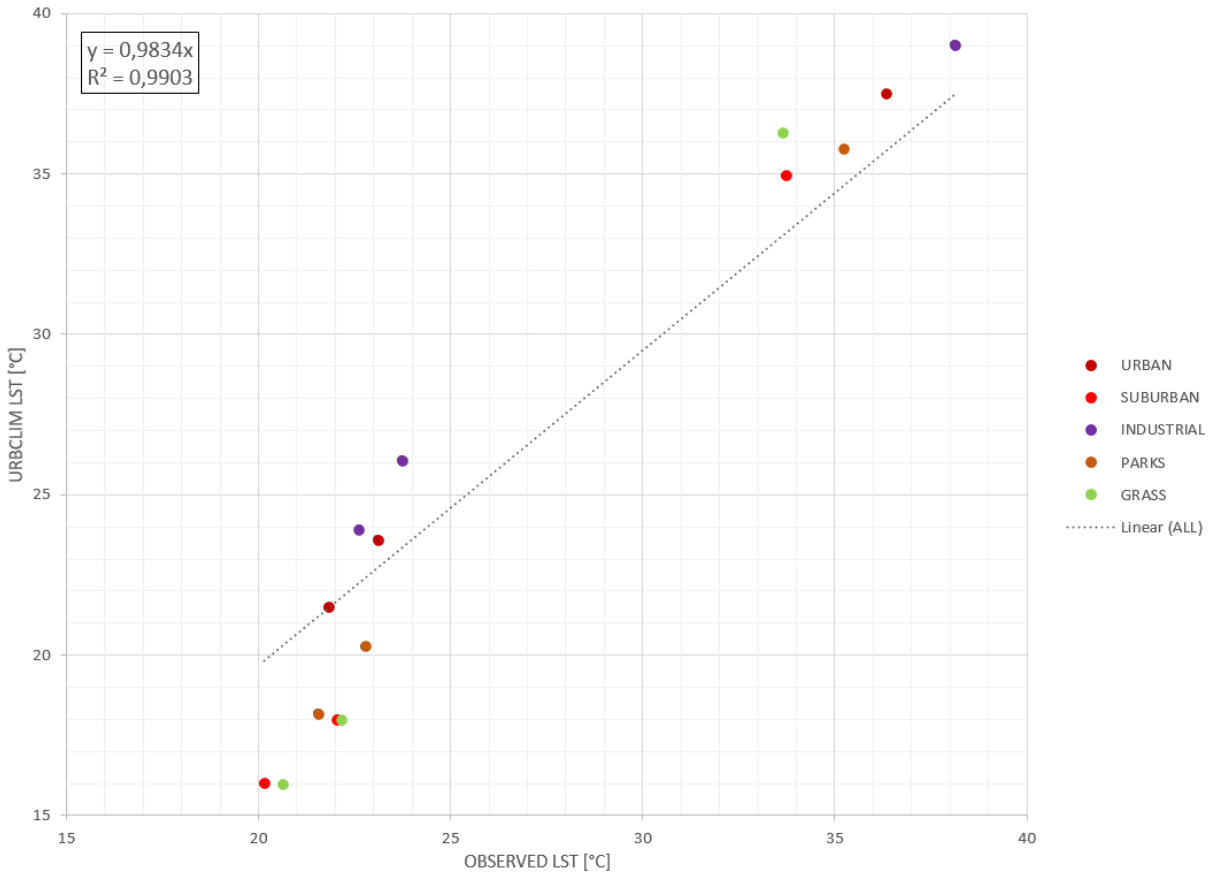

Figure 78. Comparison between modelled (AP08) and observed (AP01) land surface temperatures per model land use category in Ostrava.

In the figure below, the data points for the 4 cities are plotted together. Overall, there is a good correspondence between the model results and the observations. The model shows a general trend to slightly overestimate the LST in dense urban and industrial areas and to underestimate the LST in suburban and rural areas. This will cause a slight overestimation of the urban-rural WBGT differences in the output maps of this application, which needs to be taken into account when interpreting the maps and statistics.

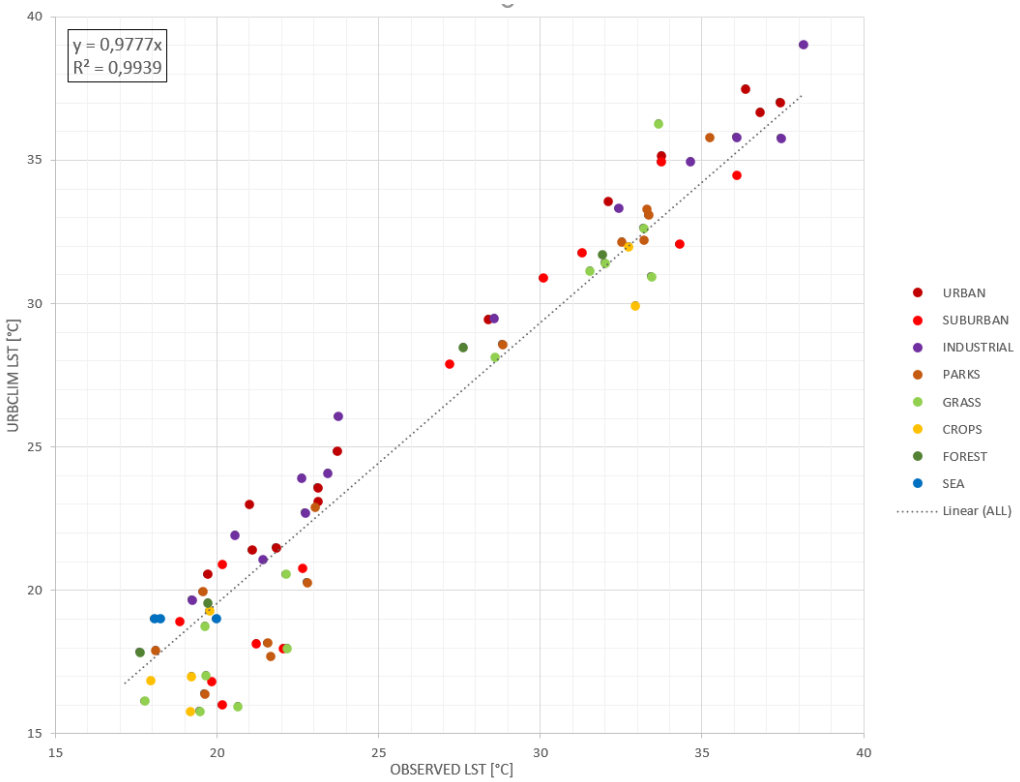

Figure 79.
Comparison between modelled (AP08) and observed (AP01) land surface temperatures per model land use category for all available data.

9.4 Application Dockerization

A stand-alone docker container of AP08 has been built, which calculates the daily maximum, minimum and mean WBGT maps for a given city, based only on a high resolution land cover input map in Geotiff format. No external Copernicus data are needed for the calculation, as all input data for the calculations are included in the docker. The source code (IP protected) of the WBGT model inside the docker container is in Python language. The rationale behind the dockerization of this application is that it will potentially allow users to modify the input land cover map and upload their own land use scenarios (e.g. development plans) from which new WBGT maps will be calculated by the AP08 docker. Working out an interactive user platform for AP08 is not foreseen in the CURE project, but having the docker container ready should allow to develop this update quickly and at a low cost in a post-project phase.

10 AP09 URBAN HEAT STORAGE MONITORING

10.1 Data & Methodology

10.1.1 Data

AP09 is implemented for Heraklion (front-runner) and Basel (follower) cities. Table 14 lists the data that are used for the AP09. AP09 is using data from three Copernicus Services (CLMS,CAMS and C3S), very high resolution optical third-party data from the Copernicus Contributing missions Data Warehouse (Copernicus, 2020) and data products from AP01.

Table 14. *Summary of data used for AP09.*

Data Source	Description of the Product
CAMS	Clear-sky surface solar irradiation
C3S	ERA5 Air Temperature
CLMS	Urban Atlas
CLMS	Urban Atlas: Building Heights
CLMS	EU-DEM
CLMS	High Resolution Vegetation Phenology and Productivity (Under Development)
Copernicus Satellite	Sentinel-2, Level-2A Bottom Of Atmosphere (BOA) reflectance images
Third-party	Baseline Land Cover from VHR (from the DWH)

10.1.2 Methodology

Heat storage flux (ΔQs) is the net flow of heat stored in urban canopy and represents all the mechanisms of energy storage within the volume, i.e., the air, on trees, in buildings constructed in the ground, etc. (Offerle et al. 2005). An updated version of the Objective Hysteresis Model (OHM) (Lindberg et al. 2018) is used in CURE to estimate heat storage at local scale (100 m). The method is adapted to Copernicus Core Services. The hysteresis effect on energy flux storage indicates how quickly the urban surface responds to the input of energy and its association with the diurnal evolution of the boundary layer, varying according to latitude, cloud cover, soil characteristics, wetness and vegetation cover. OHM is based on the following expression (Grimmond and Oke, 1999):

$$\Delta Q_S = \sum_{i}^{N}(f_i a_{1i})Q^* + \sum_{i}^{N}(f_i a_{2i})\frac{\partial Q^*}{\partial t} + \sum_{i}^{N}(f_i a_{3i})$$

where Q^* is the net all-wave radiation, $\vartheta Q^*/\vartheta t$ is the time rate of change for net all-wave radiation at the surface and f_i the fraction of each of the N surface components within each grid cell and a_1, a_2 and a_3 are coefficients associated to response of the surface cover due the energy input. Coefficient a_1 indicates the intensity of the relationship between the stored

energy flux and the net all-wave radiation. Coefficient a_2 quantifies the magnitude of hysteresis, indicating the direction and degree of the phase relationship between stored energy flux and net all-wave radiation. Coefficient a_3 is an intercept term and indicates the extent to which a negative storage energy flux occurs before the net all-wave radiation starts to become negative. The methodology followed in CURE is outlined in Figure 80.

The surface cover fractions f_i are estimated as in AP01, using VHR baseline land cover corrected with Urban Atlas CLMS information and using Sentinel-2 imagery and CLMS imperviousness and vegetation dynamics layers for monitoring the dynamic surface cover fraction change.

Coefficients a_1, a_2 and a_3 are approximated from CLMS Urban Atlas and Building Height information (Grimmond and Oke, 1999; Ward et al., 2016). Table 15 lists the coefficients, as these were determined for the city of Heraklion.

Table 15. *Coefficients used for the case study of Heraklion, Greece (buildings class: Yoshida et al., 1990, 1991; remaining: Ward et al., 2016).*

Class	a_1	a_2	a_3
Water	0.5	0.21	-39.1
Vegetation	0.336	0.313	-31.4
Bare soil	0.355	0.335	-35.275
Asphalt	0.64	0.32	-43.6
Buildings	0.71	0.04	-39.7

Q^* (W m^{-2}) is estimated using the Net All-Wave Radiation Parameterization (NARP) (Offerle et al., 2003):

$$Q^* = K_{\downarrow} - K_{\uparrow} + L_{\downarrow} - L_{\uparrow}$$

where $K_{\downarrow}$ is the incoming shortwave radiation (W m^{-2}), $K_{\uparrow}$ is the outgoing shortwave radiation (W m^{-2}), $L_{\downarrow}$ is the incoming longwave radiation (W m^{-2}) and $L_{\uparrow}$ is outgoing longwave radiation (W m^{-2}).

$K_{\downarrow}$ is given from the CAMS clear-sky surface solar irradiation product.

$K_{\uparrow}$ is estimated as:

$$K_{\uparrow} = a\, K_{\downarrow}$$

where a is the albedo provided in CURE from the blue-sky albedo product of rslab (Chrysoulakis et al., 2018).

$L_{\downarrow}$ is estimated as:

$$L_{\downarrow} = \varepsilon_a \sigma T_{\alpha}^4$$

where ε_a is the broadband atmospheric emissivity, σ is the Stefan's constant and T_{α} is the bulk atmospheric temperature (K) approximated by the air-temperature near the surface (2 m) as derived from the C3S ERA5 Air Temperature (2 m) product.

ε_a is estimated as:

$$\varepsilon_a = 1 - (1 + w)e^{-\sqrt{1.2+3w}}$$

where w is the precipitable water content (g cm^{-2}), derived from C3S ERA5.

$L_{\uparrow}$ is estimated as:

$$L_{\uparrow} = \varepsilon_s \sigma T_s^4 + 0.08 K_{\downarrow}(1 - \alpha) + (1 - \varepsilon_s) L_{\downarrow}$$

where ε_s is the surface emissivity and T_s is the LST, as derived from AP01.

The coefficients a_1, a_2 and a_3 are determined from CLMS, based on the land cover as explained earlier. The parameter $\partial Q^*/\partial t$ is calculated by assuming the Q* difference between two times instances t_1 and t_2, i.e. $\partial Q^*/\partial t = (Q_2^* - Q_1^*)/(t_2 - t_1)$, with time difference smaller than an hour. To achieve this, LST from more sources was necessary. Therefore, thermal images from MODIS (Moderate Resolution Imaging Spectroradiometer) were used in AP01 to produce LST maps with minor time difference to the Sentinel-3 ones.

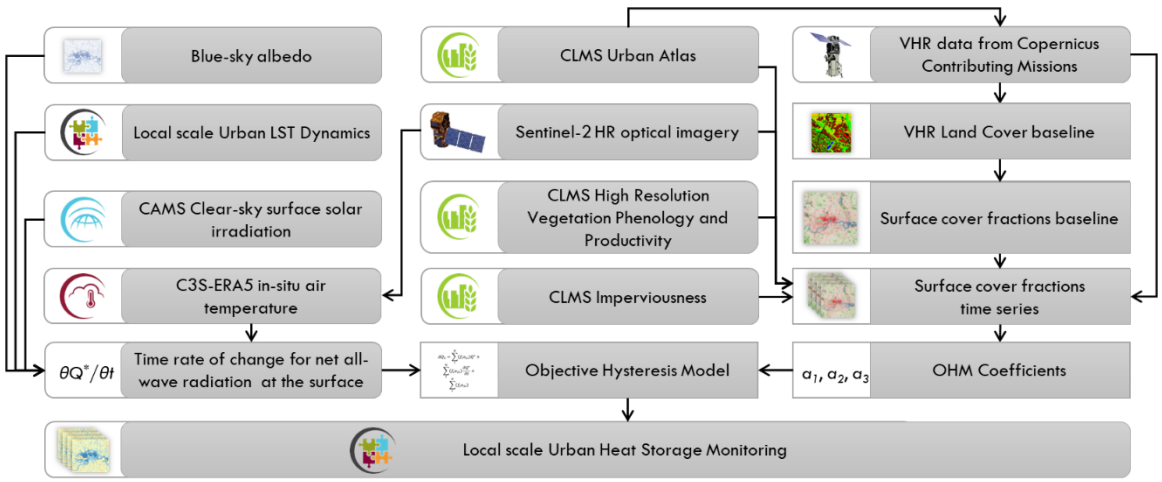

Figure 80. Methodology for the estimation of Urban Heat Storage at local scale.

10.2 Results

Figure 81 shows a sample result of AP09 for the front-runner city of Heraklion, Greece. A daytime and a nighttime map of heat storage flux ΔQS in W m^{-2} are displayed. The sea is masked out of the computations and therefore the area appears white. Missing values (also in white), i.e. in the coastline and some inside the images, are due to the cloud cover mask of Sentinel-3 and/or MODIS.

Resulting maps indicate high amount of energy stored inside the urban area of Heraklion during daytime. As expected, the energy from solar radiation during noon is trapped inside the city and it is stored particularly in buildings with an increased pace ranging from 350 to 500 W m^{-2}. While in the surrounding rural areas, energy is stored in a much lower pace (lower than 200 W m^{-2}). The opposite phenomenon is evident during nighttime in this example. This nighttime map corresponds to almost midnight, with sunset around 21.00 local time. The city has released most of the available energy stored during daytime and it is currently releasing in a lower pace (~30-50 W m^{-2}).

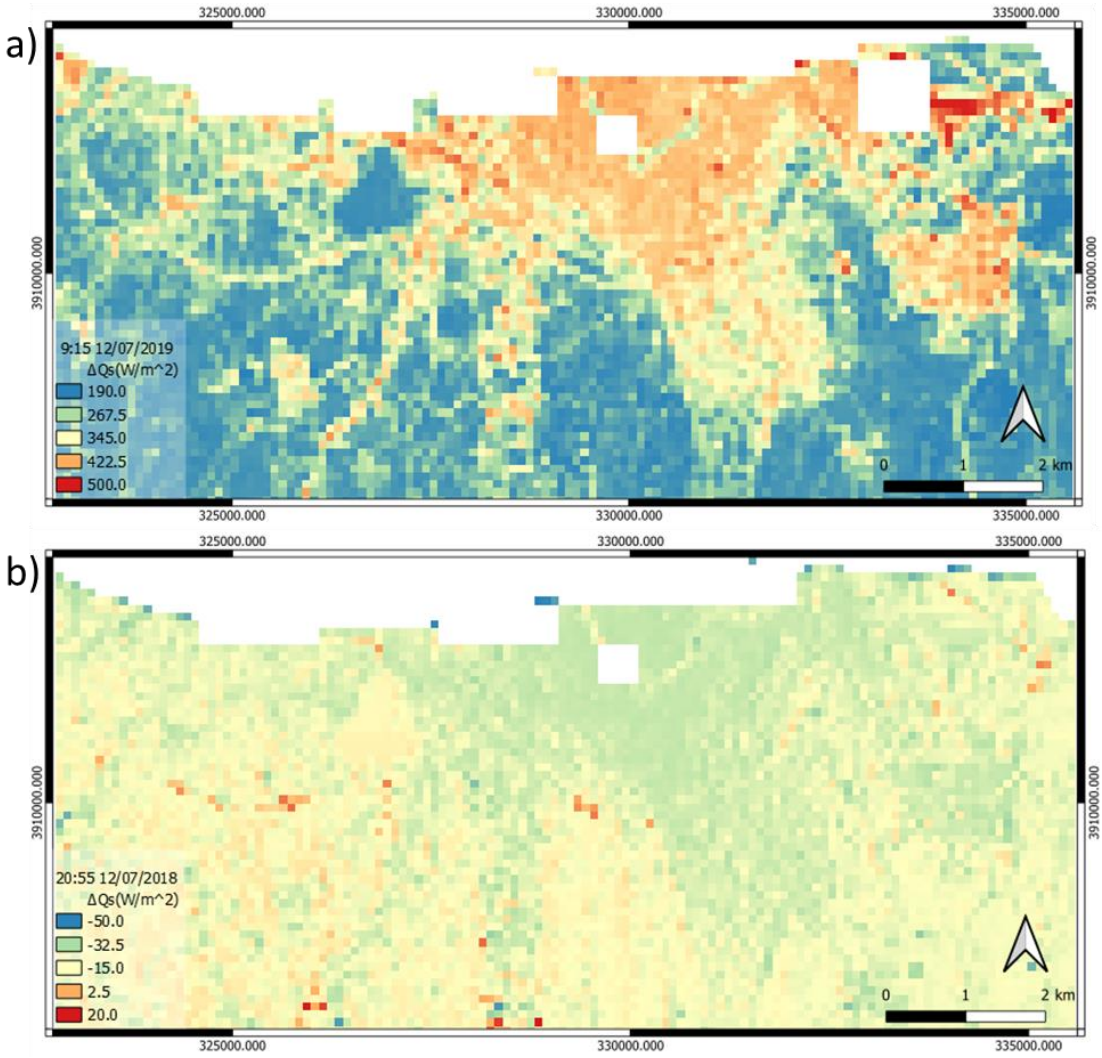

Figure 81. Sample AP09 product: Spatial distribution of the heat storage flux ΔQs [W m^{-2}] for Heraklion a) daytime on 21 July 2019, 12.15 local time and b) nighttime on 12 July 2018, 23.55 local time.

10.3 Evaluation

We have evaluated the data from Copernicus Services with local data from meteorological and radiometer station. Meteorological data and Incoming radiation data are collected from a local

station called HECKOR that contains meteorological sensors for air temperature and a radiometer for incoming and outgoing radiation. The evaluation of products took place from 28 February 2018 to 17 October 2018 and 1 June 2019 to 31 December 2019. Heat storage flux were calculated to evaluate in four scenarios, all data from Copernicus, replaced temperature from HECKOR, replaced Incoming short-wave radiation from HECKOR, replaced temperature and incoming short-wave radiation from HEKOR. For each scenario the data are separated to day and night data. The scatterplot, RMSE and MAE have been calculated for each scenario. The analysis has been done for the frontrunner city of Heraklion and inside the HEKOR footprint.

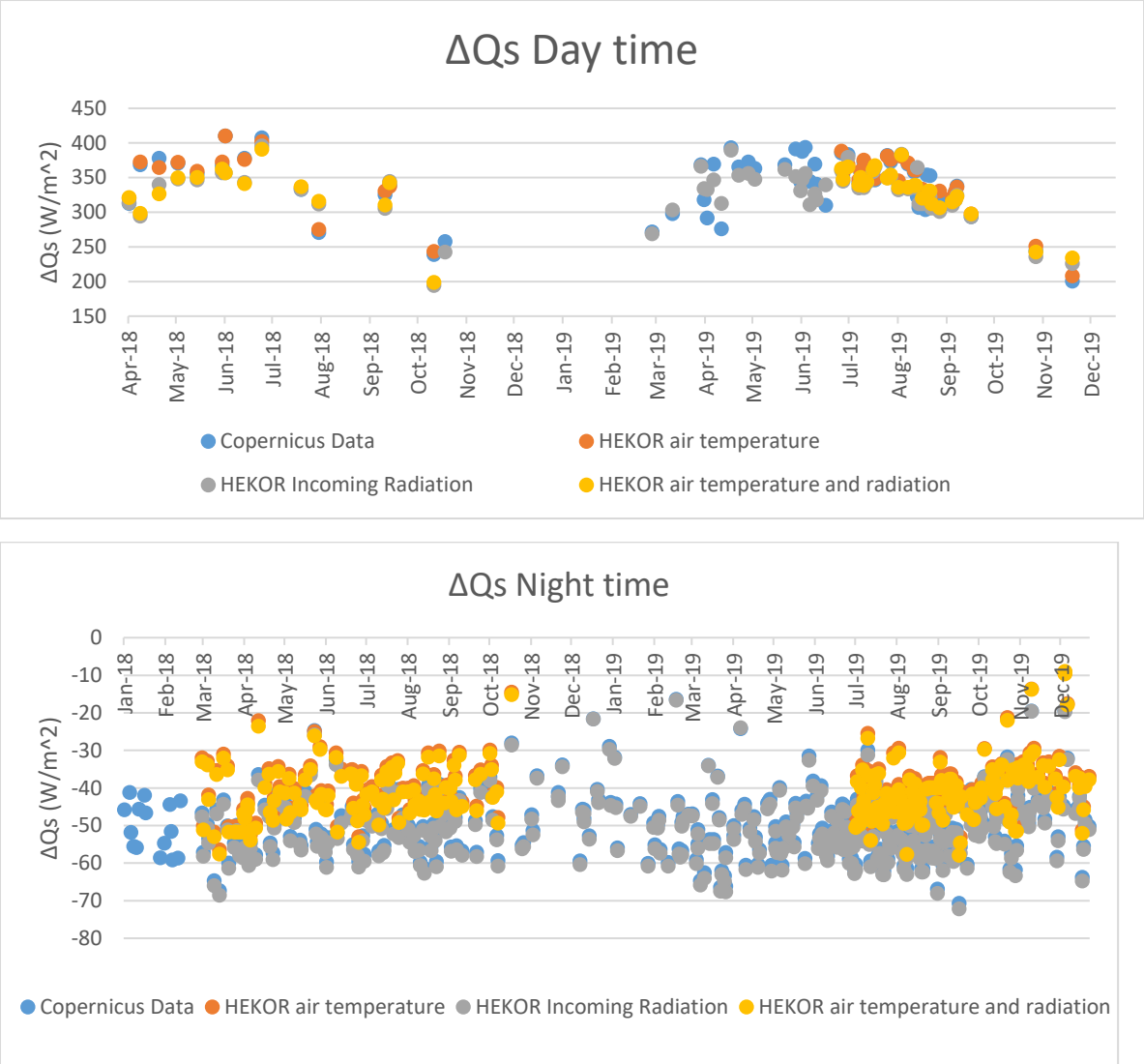

Figure 82 ΔQs values for Day time and Night time.

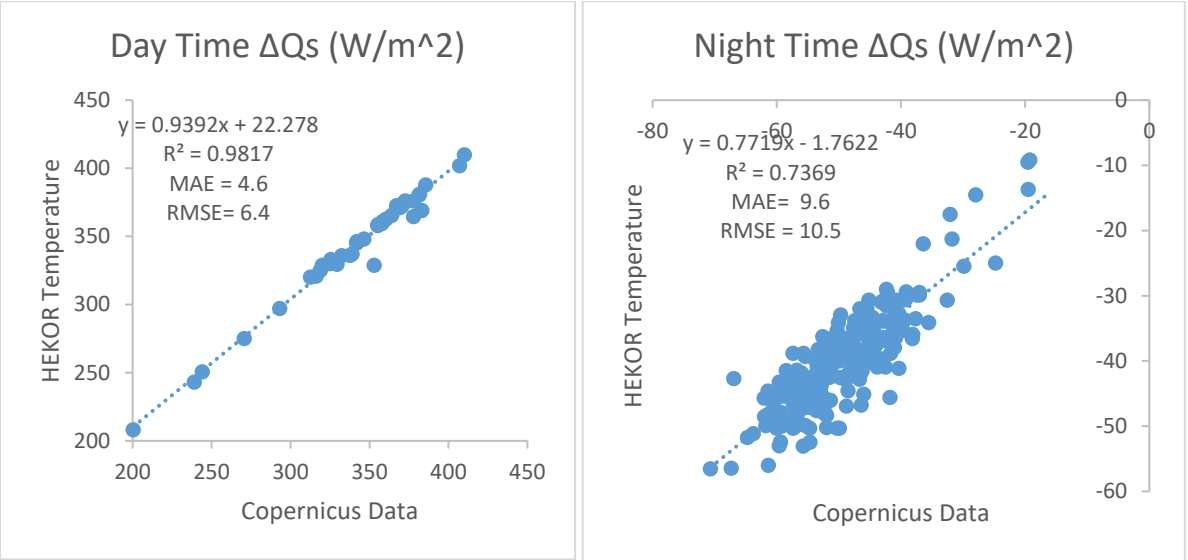

Figure 83 The comparison for the 1st and 2nd scenario, Copernicus Data compared to Copernicus Data replaced temperature from HEKOR local data

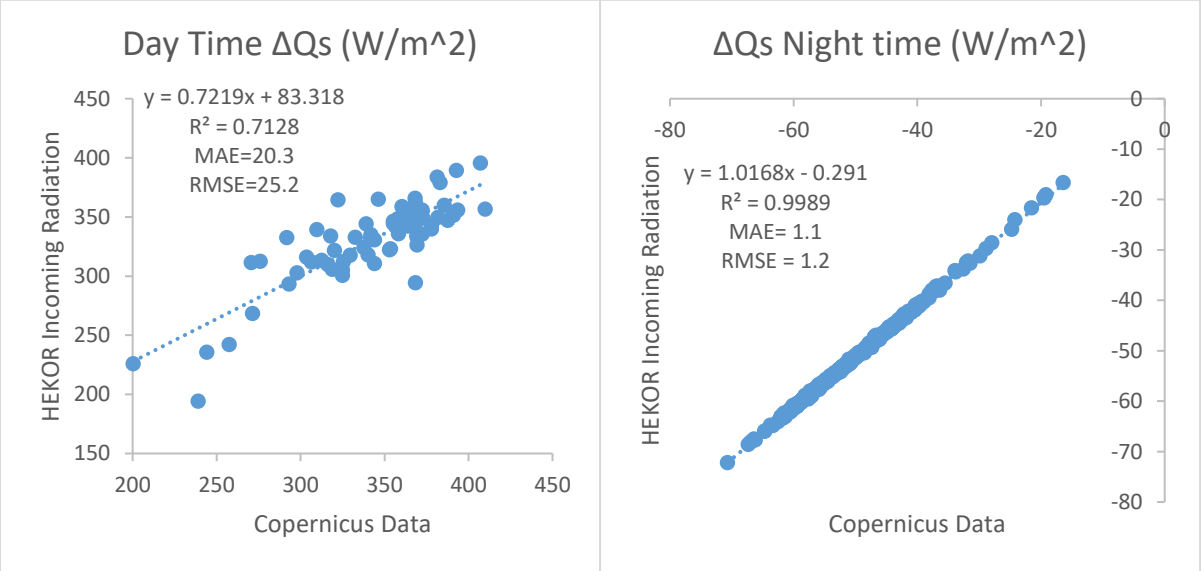

Figure 84 The comparison for the 1st and 3rd scenario, Copernicus Data compared to Copernicus Data replaced incoming radiation from HEKOR local data.

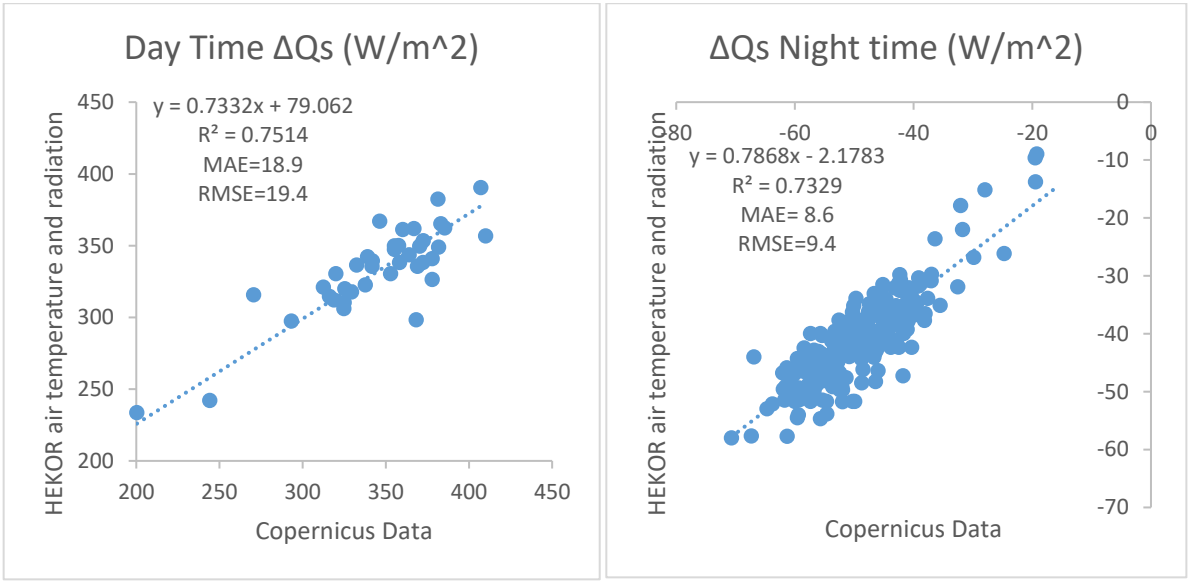

Figure 85 The comparison for the 1st and 4th scenario, Copernicus Data compared to Copernicus Data replaced incoming radiation from HEKOR local data.

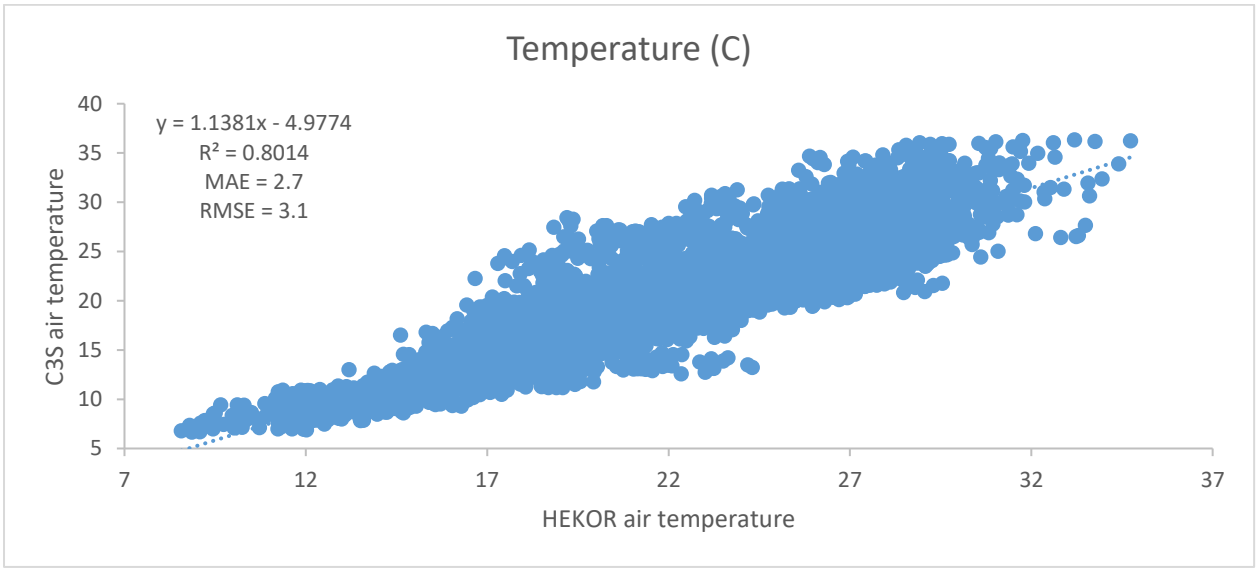

Figure 86 The comparison of air temperature from C3S and HEKOR local data for the whole time series

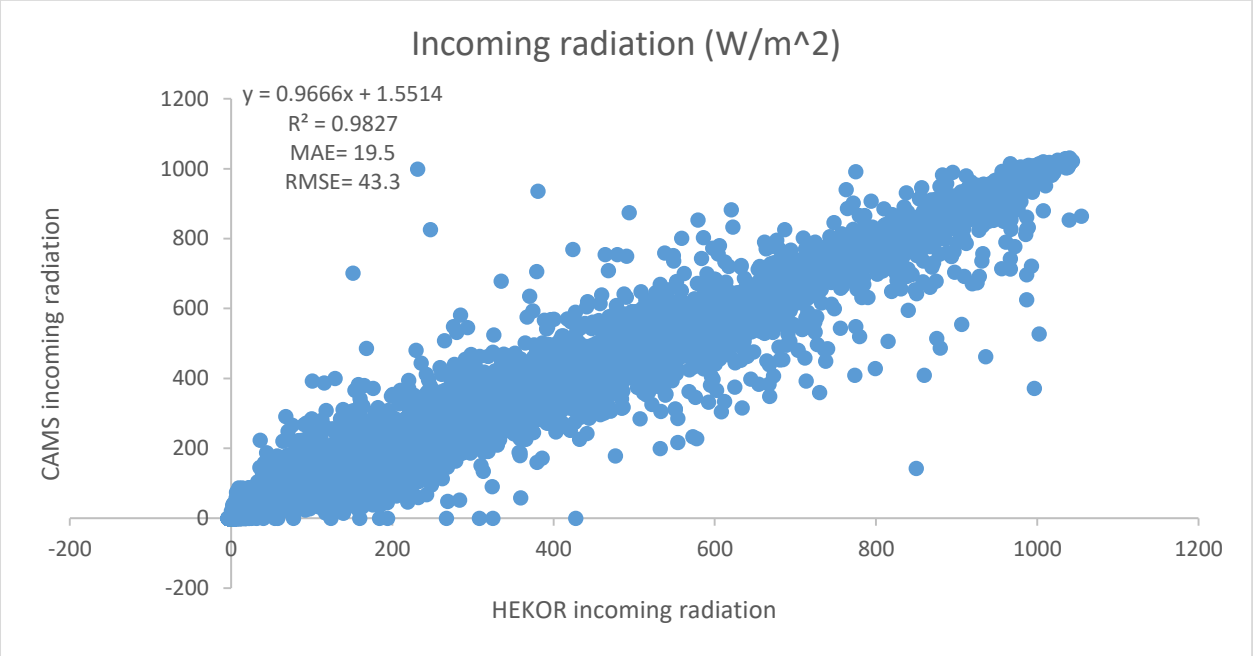

Figure 87 The comparison of incoming shortwave radiation from CAMS and HEKOR local data for the whole time series

The results show a small change in Heat storage flux when the radiation is replaced, especially in day that the difference of incoming radiation is due to the station footprint and temporal resolution, HEKOR produce 30-minute average instead of 1-minute average from CAMS. When the temperature is replaced from HEKOR data to compare results at night, there is a slight variation, but the findings are still quite similar when the incoming radiation is replaced. This is because during night the incoming radiation is 0 and doesn't affect the Heat storage flux. The comparison of Temperature and Incoming radiation data shows a small error between HEKOR and Copernicus services as a result high quality data produces from Copernicus.

10.4 Application Dockerization

A stand-alone docker container of AP09 has been built, which calculates the Heat storage flux maps for a given city, based on land cover input map in Geotiff format, LST from APP01, air temperature from C3S and incoming radiation from CAMS. The source code (IP protected) of the OHM model inside the docker container is in Python language. The rationale behind the dockerization of this application is that it will potentially allow users to choose the time series from which new ΔQs maps will be calculated by the AP09 docker. The Docker contains three folders with dynamic inputs (AP01 LST, AP01 Land cover fractions, incoming radiation and temperature), static inputs (albedo, OHM coefficients) and output.

11 AP10 NATURE BASED SOLUTIONS

11.1 Data & Methodology

In urban areas, contribution of green roofs is a valid alternative to increase the green area, especially where available land for greening is limited. The methodology proposed aims to estimate the potential for green coverage at rooftop level by identifying suitable locations for green roof deployment and supporting decision-making towards broader sustainable urban development.

With the objective of comparing the results of the analysis and their accuracy, three inputs for object detection will be considered:

- LiDAR: From LIDAR data digital surface model is derived, which includes elevation data of the urban environment, including the elevations of urban elements such as buildings, vegetation or roads, among others. The number of points and point density improves data accuracy, which is crucial.
- Stereo Imagery DSM: Out of the granted VHR WorldView-1 and WorldView-3 images acquired at different time steps with different viewing angles, we generate a sub-meter (i.e., 50 cm) spatial resolution DSM. In particular, the DLR "Catena" operational infrastructure is used. Here, the standard chain generates orthorectified images using a worldwide reference image database. For this task, ground control points are automatically extracted from the satellite and reference images, which are used to correct attitude and ephemeris data. Next, the original satellite image is orthorectified using a high-resolution digital elevation model. Finally, automatic atmospheric correction is performed and concurrently the DSM is generated.
- Euro-Maps 3D DSM: Euro-Maps 3D products developed by GAF are DEMs semi-automatically derived from 2.5 m in-flight stereo data provided by IRS-P5 Cartosat-1 and. Among these, the Euro-Maps 3D DSM layer is a homogeneous 5m spaced DSM product including detailed flanking information consisting of several pixel-based quality and traceability layers. A sophisticated and tailored algorithm based on semi-global matching is applied and the reliability of the information is increased by using multiple overlapping stereo pairs. Since 2020, Euro-Maps 3D products are available from ESA as Third Party Mission data for on demand ordering upon submission of a Project Proposal subject to evaluation and acceptance. In this regard, the CORE consortium is going to submit a dedicated proposal in early 2021.

Buildings outlines are derived from cadastral map in form of vector file.

The methodological process for the calculation as described below:

Identification of the maximum green roof potential

As flat or quasi flat roofs are the ones more suitable to host a green cover, slope computation is performed (step 1). For each unit (building), an analysis of the slope is performed on the basis of each DSM by measuring the actual slope at each point/pixel of the roof. The slope map of the building is analyzed using a statistical algorithm that gives us the estimation of the real slope and the flat area available. Buildings with a suitable flat surface are labeled as flat roof by noting their flat zone percentage. The threshold for the slope computation is adjusted on a case by case, considering local regulations and policies. Consequently, for each building, the percentage of flat surface is calculated (step 2), considering roofs whose flat surface percentage is greater than 10% if their size is lower than 100 m² or greater than 5% if their size is greater than 100 m², which are those considered as suitable for hosting a green roof (Marconcini et al. 2016). This process allows for determining the maximum green roof potential (step 3) of each building, which is the maximum area that is suitable to host a green roof.

Prioritization of areas with highest potential/benefit

Benefits of green roofs are larger if these solutions are installed in areas characterized by low NDVI, impervious surface and high LST (step 4), contributing also to reduce the Urban Heat Island effect. All these characteristics determine the priority of the area where the buildings are located.

Identification of buildings with highest potential

The building outlines is read from a vector file where the 2D geometry is defined. The data model needs to be completed with all the available semantic information (step 5). Cadastral information will be used to include the year of construction. In addition, information on flat surface percentage of the building is assigned from the calculated flat surface map and maximum green roof potential (step 3) is calculated.

Prioritization of green roofs

Finally, to prioritize the buildings for implementing green roofs, the area priority and the building priority is combined (step 6). The prioritization of areas is based on LST, NDVI and Imperviousness (step 3), and the prioritization of buildings is based on year of construction and maximum green roof potential. These prioritizations are calculated through a weighted combination that might be specified by the user depending on the city characteristics.

The following graph shows the overall approach and methodological steps for the development of the NBS App:

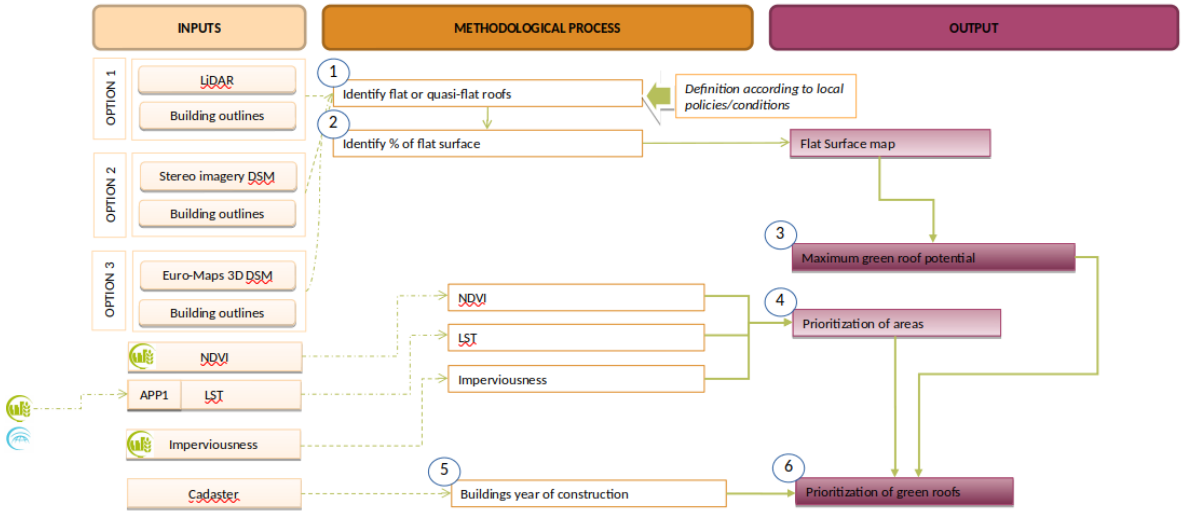

Figure 88. Overview of the Nature Based Solution App

Table 16. Overview of the input datasets for the prioritization of green roofs

INPUT	*Copernicus service*	*Dataset*	*Usage*
LIDAR (option 1)			Identify flat surface of the roofs
Stereo imagery DSM (option 2)			Identify flat surface of the roofs
Euro-Maps 3D DSM (option 3)			Identify flat surface of the roofs
Building outlines			Identify flat surface of the roofs
NDVI	CLMS	NDVI	Identify already existing green roofs (with vegetation >10%)
LST	CLMS, CAMS	LST (APP1)	Prioritize intervention areas
Imperviousness	CLMS	Imperviousness	Prioritize intervention areas
Cadaster			Inclusion of cadastral semantic information (year of construction)

11.2 Results

11.2.1 Sofia

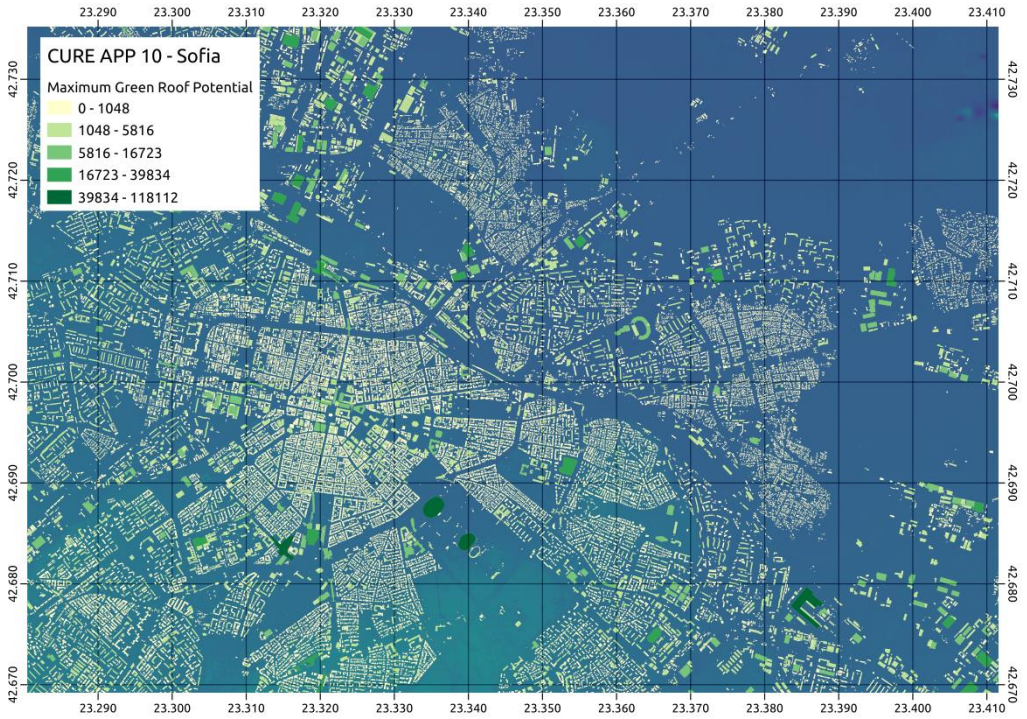

Figure 89. Maximum green roof potential in Sofia.

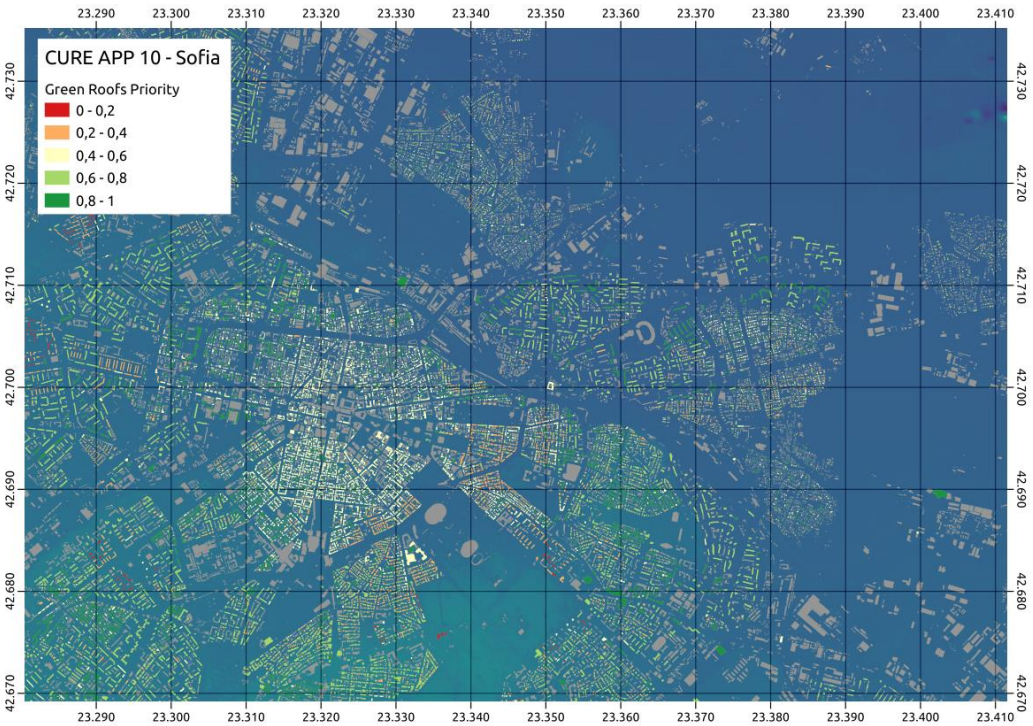

Figure 90. Green roofs priority in Sofia.

11.2.2 San Sebastian

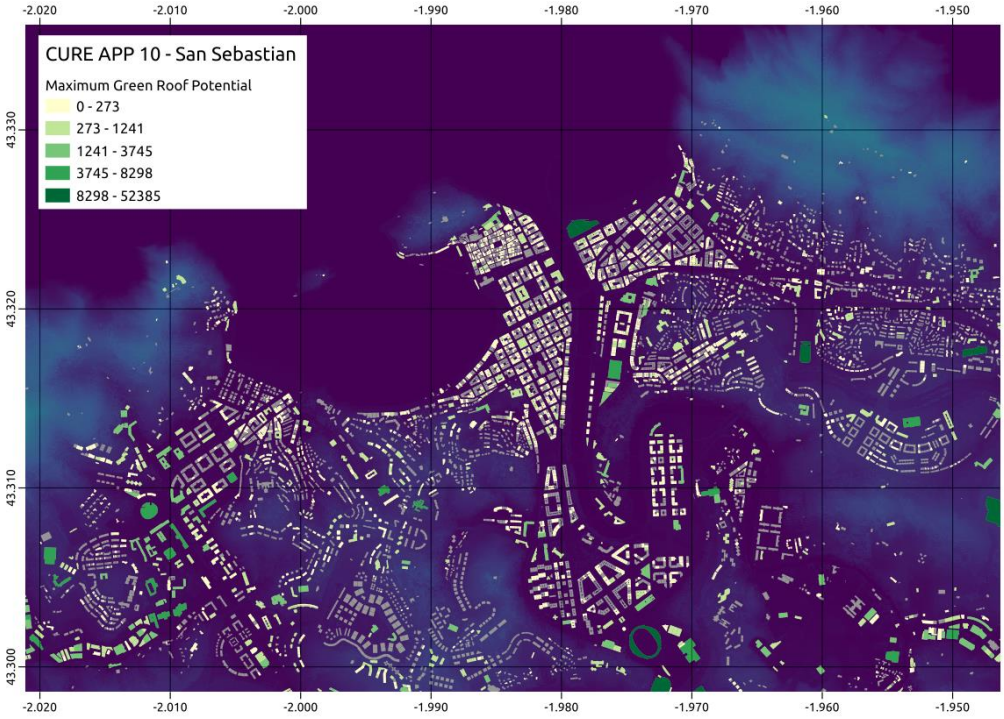

Figure 91. *Maximum green roof potential in San Sebastian.*

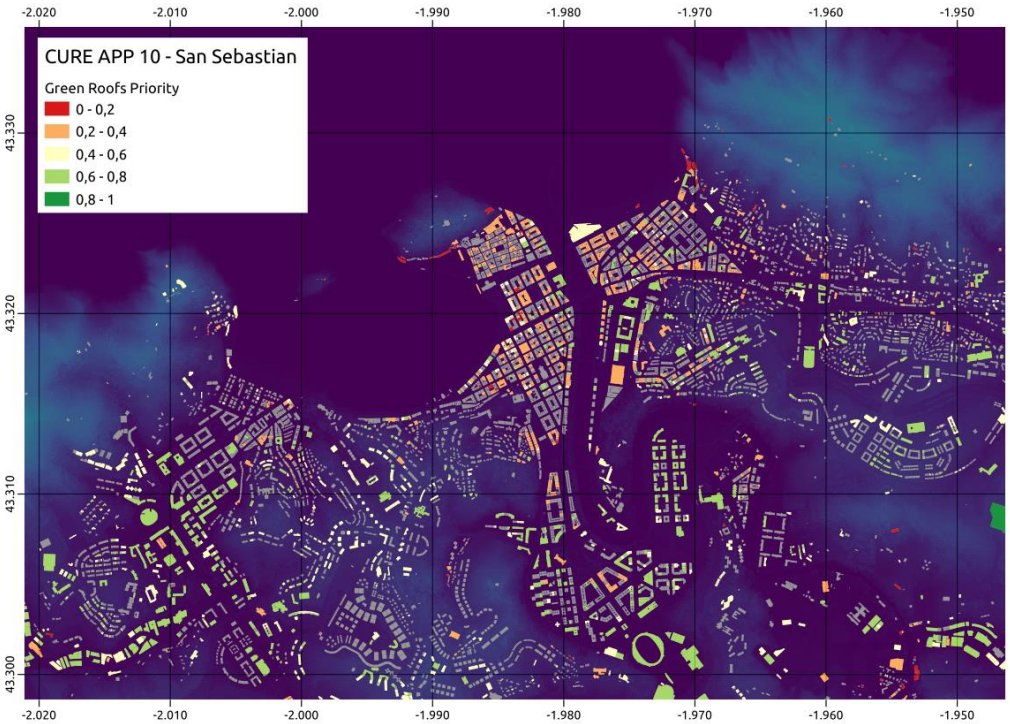

Figure 92. *Green roofs priority in San Sebastian.*

11.3 Evaluation

For the cities analyzed (Sofia and San Sebastian) no information on green roof potential from other products is available.

Initially the comparison of different data sources was proposed for the comparison of results in the calculation of roof slope, i.e., LiDAR, Stereo imagery DSM, and Euro-Maps 3D DSM. However, it has not been possible to obtain different data sources for the same city. In San Sebastian LiDAR has been used, while in Sofia Stereo imagery DSM has been used.

The results look reasonably good in both cities upon visual inspection. However, an in-depth comparison has not been possible as they are different cities with a particular urban morphology in both cases.

11.4 Application Dockerization

The application has been dockerized to be deployed on servers with higher processing and storage capacity. The following table shows the inputs and formats of the application:

Table 17. *Input files and formats for the prioritization of green roofs*

File	*Format*	*Description*
DSM	GeoTIFF	Digital surface model. Very high-resolution raster where each cell represents the elevation. Its source might be LiDAR, stereo imagery DSM or any other DSM.
Buildings	Shapefile	Buildings. The geometry shall be polygons and it shall have at least a column with the building's id and a column with the building's year of construction.
NDVI	GeoTIFF	Normalized difference vegetation index. Raster for area prioritization. Medium resolution is required.
LST	GeoTIFF	Land surface temperature. Raster file where each cell represents the temperature. Its source is APP1.
Imperviousness	GeoTIFF	Imperviousness. Raster for area prioritization. Medium resolution is required.

The outputs of the application together with the format is shown in the following table:

Table 18. *Output file and format for the prioritization of green roofs*

File	*Format*	*Description*
Buildings prioritization	Geopackage	Buildings polygons with three columns: the id of the building; the maximum green roof potential; and the priority value.

The application has a series of parameters to establish the weight of the variables used in the prioritization of green roofs. Less experienced users can use the default values. However, in those cities where specific criteria are required based on the characteristics of the city or the specific objective sought with the installation of green roofs, these parameters can be modified.

12 AP11 HEALTH IMPACTS

12.1 Data & Methodology

12.1.1 The EVA model

The integrated model system is based on the impact-pathway chain and is used for assessment of health impacts from air pollution in many major Danish cities. This includes both health effects and related external costs (sometimes also referred to as "indirect costs") which can be attributed to air pollution exposure.

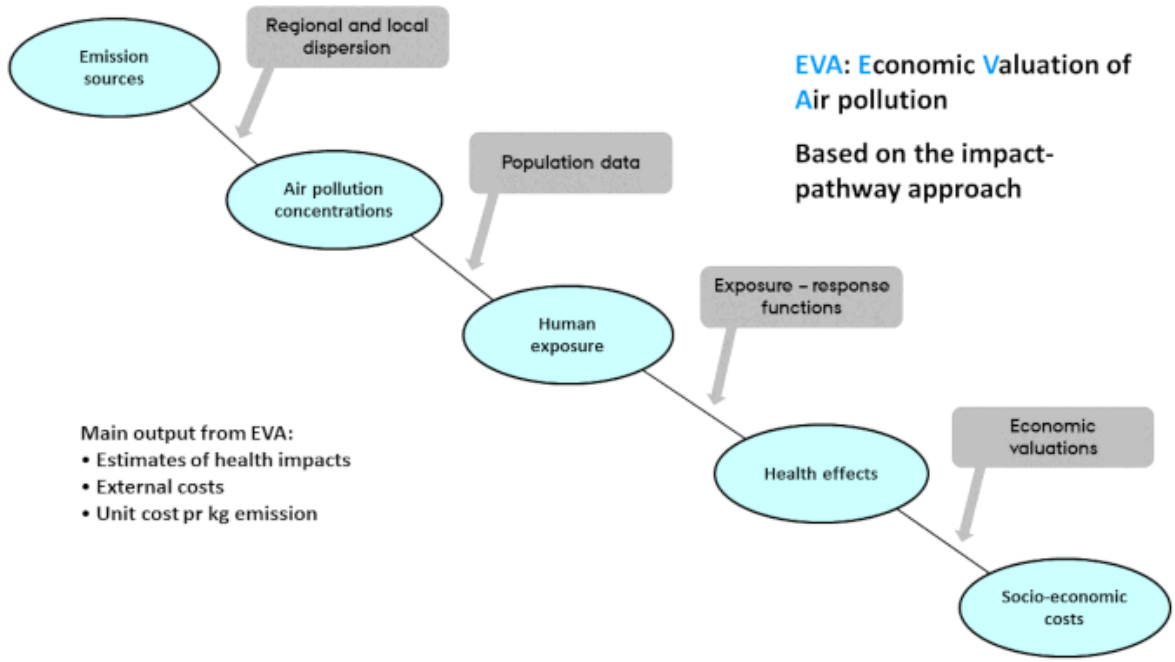

Figure 93. *A schematic diagram of the impact-pathway methodology. The site-specific emissions result (via atmospheric transport and chemistry) in a concentration distribution, which together with detailed population data, can be used to estimate the population-level exposure. Using exposure-response functions and economic valuations, the exposure can be transformed into impacts on human health and related external costs.*

Chemical components important for health impacts and included in the EVA system are: nitrogen dioxide (NO2), sulphur dioxide (SO2), ozone (O3) and particulate matter (PM2.5), where the individual constituents of PM2.5 are: mineral dust, black carbon (BC), organic matter (OM), secondary inorganic aerosols (SIA – i.e. nitrate, sulphate and ammonia), secondary organic aerosols (SOA) and sea salt.

The EVA model is coupled to the air pollution models DEHM (Danish Eulerian Hemispheric Model) and UBM (Urban Background Model) for regional-scale and local-scale health impact assessments, respectively. EVA includes gridded population data, exposure-response functions for health impacts in terms of morbidity and mortality, and economic valuation of the health impacts from air pollution.

The EVA system uses comprehensive and thoroughly tested chemistry-transport models when calculating air pollution levels in general as well as scenarios describing how specific changes in emissions of pollutants to the air affect air pollution levels at regional and local scale.

Modelling of air quality is based on the regional air pollution model DEHM and the urban background model UBM resulting in calculations performed on a 1 km x 1 km grid resolution. Urban background concentrations are the general air pollution in the city and reflect the concentrations in a park, a backyard or the roof of buildings. Urban background concentrations differ from street concentrations, which represent the concentrations in the height of 2 m at the facade of buildings. Street concentrations are calculated using air quality model OSPM.

To estimate the effect of a specific emission source or emission sector, emission inventories for the specific sources are implemented in DEHM, together with all other relevant anthropogenic and natural emission sources, see Table 19 for description of emission sources.

Table 19. *Definition of the SNAP categories and a short description of the emissions of interest.*

Region	SNAP	Emission scenario (or the "tag")
EU/DK	1	Combustion in energy and transformation industries
	2	Non-industrial combustion plants, including private wood combustion
	3	Combustion in manufacturing industry
	4	Production processes
	5	Extraction and distribution of fossil fuels and geothermal energy
	6	Solvents and other product use
	7	Road transport
	8	Other mobile sources and machinery (excl. international ship traffic)
	9	Waste treatment and disposal
	10	Agriculture
	Sum 1–10	Sum of the above 10 SNAP categories
	All	All anthropogenic emissions (SNAP 1–SNAP 10)

To calculate the impacts of the total air pollution levels or of emissions from a specific source or sector, concentrations and address-level population data are combined to estimate human exposure, and then the response is calculated using an exposure-response function (ERF) of the following form: $R = A \cdot C \cdot P$, where R is the response (e.g. in cases, days, or episodes), C the concentration (i.e. the total concentration or additional concentration resulting from emissions of a particular emission source), P the affected share of the population, and A is an empirically determined constant for the particular health outcome, typically obtained from published cohort studies, see Table 20 for exposure-response functions.

Table 20. Example of health effects, exposure-response functions and economic valuation (applicable for Danish/European conditions) included in the EVA model system (note, prices are from 2006). (PM is particulate matter, including primary PM2.5,NO−3and SO2−4. YOLL is years of life lost. SOMO3 (Sum of Ozone Means Over 35 ppb) is the sum of means over 35 ppb for the daily maximum 8-hour values of ozone.

Health effects (compounds)	Exposure-response coefficient (α)	Valuation, euros (2006 prices)
	Morbidity	
Chronic bronchitis (PM)	8.2×10^{-5} cases/$\mu g m^{-3}$ (adults)	52 962 per case
Restricted activity days (PM)	$= 8.4 \times 10^{-4}$ days/$\mu g\, m^{-3}$ (adults) -3.46×10^{-5} days/$\mu g\, m^{-3}$ (adults) -2.47×10^{-4} days/$\mu g\, m^{-3}$ (adults > 65) -8.42×10^{-5} days/$\mu g\, m^{-3}$ (adults)	131 per day
Congestive heart failure (PM) Congestive heart failure (CO)	3.09×10^{-5} cases/$\mu g\, m^{-3}$ 5.64×10^{-7} cases/$\mu g\, m^{-3}$	16 409 per case
Lung cancer (PM)	1.26×10^{-5} cases/$\mu g\, m^{-3}$	21 152 per case
	Hospital admissions	
Respiratory (PM) Respiratory (SO_2)	3.46×10^{-6} cases/$\mu g\, m^{-3}$ 2.04×10^{-6} cases/$\mu g\, m^{-3}$	7931 per case
Cerebrovascular (PM)	8.42×10^{-6} cases/$\mu g\, m^{-3}$	10 047 per case
	Asthma, children (7.6 % <16 yr)	
Bronchodilator use (PM) Cough (PM) Lower respiratory symptoms (PM)	1.29×10^{-1} cases/$\mu g\, m^{-3}$ 4.46×10^{-1} days/$\mu g\, m^{-3}$ 1.72×10^{-1} days/$\mu g\, m^{-3}$	23 per case 59 per day 16 per day
	Asthma, adults (5.9 % >15 yr)	
Bronchodilator use (PM) Cough (PM) Lower respiratory symptoms (PM)	2.72×10^{-1} cases/$\mu g\, m^{-3}$ 2.8×10^{-1} days/$\mu g m^{-3}$ 1.01×10^{-1} days/$\mu g\, m^{-3}$	23 per case 59 per day 16 per day
	Loss of IQ	
Lead (Pb) (<3 year)* Mercury (Hg) (foetus)*	1.3 points/$\mu g\, m^{-3}$ 0.33 points/$\mu g\, m^{-3}$	24 967 per point 24 967 per point
	Mortality	
Acute mortality (SO_2) Acute mortality (O_3)	7.85×10^{-6} cases/$\mu g\, m^{-3}$ 3.27×10^{-6}*SOMO35 cases/$\mu g\, m^{-3}$	2 111 888 per case
Chronic mortality, YOLL (PM) Infant mortality (PM)	1.138×10^{-3} YOLL/$\mu g\, m^{-3}$ (>30 yr) 6.68×10^{-6} cases/$\mu g\, m^{-3}$ (>9 months)	77 199 per YOLL 3 167 832 per case

EVA calculates and uses the annual mean concentrations of CO, SO2 and PM2.5, while for O3, it uses the SOMO35 metric that is defined as the yearly sum of the daily maximum of 8 h running average over 35 ppb, following WHO (2013) and EEA (2017).

In EVA, the number of lost life years for a Danish population cohort with normal age distribution, when applying the ERF of Pope et al. (2002) for all-cause mortality (relative risk, RR of 1.062 (1.040–1.083) on a 95 % confidence interval), and the latency period indicated, sums to 1138 years of life lost (YOLL) per 100.000 individuals for annual PM2.5 increase of 10 µg m−3 (Andersen et al., 2008). EVA uses a counterfactual PM2.5 concentration of 0 µgm−3 following the EEA methodology, meaning that the impacts have been estimated for the full range of modelled concentrations from 0 µg m−3 upwards.

For Copenhagen the results will be obtained through this method:

1. *Air Quality Assessment*

An air quality assessment is carried out that describes the spatial distribution of background concentrations with a resolution of 1 km x 1 km, as well as street concentrations at address level in the Capital Region. This description is based on data from a national data set, which is called Air Quality at Your Street (http://luftenpaadinvej.au.dk). For our second frontrunner city, Sofia, we will rely on a local air pollution data set. Furthermore, a summary of the results from the fixed measuring stations in the Capital Region is carried out and compared with EU limit values for air quality and WHO air quality guidelines.

2. *Health impacts and related external costs*

Health effects and related external costs are calculated for the total air pollution in the Capital Region. The total air pollution includes all sources from the Capital Region, and all other sources in Denmark and abroad. This also describes how much of total air pollution originates from local sources and how much is from sources outside the Capital Region. Moreover, calculations are carried out for each type of emission source in the Capital Region to quantify the contribution of the different sources. In principle, the Capital Region is able to regulate these sources.

Then we add calculations to the health impacts and related external costs based on information about the sources of pollution and their location, the dispersion of air pollution as well as exposure of the population, the dose-response relationship between exposure and health effects, and the valuation of health effects, also referred to as external costs related to health effects from air pollution. The EVA system includes population data with a spatial resolution of 1 km x 1 km.

12.2 Results

Application 11 models the health and economic costs of air pollution for the city of Copenhagen and Sofia. Here we use the air quality maps developed by VITO in Application 7 (Urban Air Quality) for Sofia, where they have mapped the yearly mean concentrations of Nitrogen dioxide and PM2.5 for the year of 2018 based on Copernicus data and also supplemented with local data. The air quality has furthermore been grouped according to sector contribution (road traffic, industry, power plants and residential heating). Using these results, stakeholders can identify key sectors for which measures should be prioritized. The sector contribution also provides a rough estimate for the (theoretical) maximal pollution reduction due to local measures for the sector under consideration. The results for particulate matter for instance highlight the importance of the urban residential emissions at this specific location. Also, the urban traffic emissions contribute a significant fraction to the total concentrations, whereas the urban power plant and industrial emissions are responsible for only a negligible fraction of the total pollution. Approximately a third of the pollution at this specific location is emitted outside the domain, or by sectors that are not explicitly considered in the modelling. The results for NO_2 can be interpreted in a similar way, indicating the importance of the traffic emissions at this specific location. This is then coupled to the

Evaluation of Air Pollution Model, which models the effect of the air pollution on different health parameters, such as:

AD "Acute" premature deaths from short term exposure of O3 and PM25
CD "Chronic" premature deaths from long-term exposure to PM25
ADCD Sum of AD and CD
RHA Respiratory hospital admissions
CHA Cardiovascular hospital admission
COU_C Asthma symptoms/cough
CB Chronic Bronchitis
CB_C Chronic Bronchitis - Children
WLD Work loss days
RAD Restricted activity days
MRAD Minor Restricted activity days
LC Lung Cancer
IM Infant Mortality
PWM_PM25 Population weighted mean for PM25

Figure 94. Health parameters from the EVA model.

Main results Copernicus															
RUN	YEAR	ADO3	AD	CD	ADCD	RHA	CHA	COU_C	CB	CB_C	WLD	RAD	MRAD	LC	IM
Total_Copernicus	2018	14,1	263,3	1326,9	1590,2	1186,3	483,2	104,3	1336,7	3244,4	122493,1	1545656	165,1	24,2	1,14
Background_Copernicus	2018	18,2	197	941,9	1138,9	861,8	376	75,2	958,5	2338,7	87948,8	1109122	212,6	17,4	0,82
Total Local contribution	2018	-4,1	66,3	385	451,3	324,5	107,2	29,1	378,2	905,7	34544,3	436533,3	-47,5	6,8	0,32
Traffic_Copernicus	2018	-3,5	3,7	52,5	56,2	141,4	-0,6	3	37,9	90,7	3495,3	43692,4	-40,7	0,7	0,03
Residential_Copernicus	2018	-0,2	62,7	342,1	404,8	178,7	108,7	26,1	338,9	811,5	30921,8	391234,5	-2,7	6,1	0,29
B_Industry_Copernicus	2018	0	0,2	1,1	1,3	0,8	0,3	0,1	1,1	2,6	95,3	1201,7	-0,1	0	0
A_publicPower_Copernicus	2018	-0,1	-0,1	2,1	2	4,4	-0,3	0,1	0,4	0,8	31,8	403,5	-1,6	0	0
Sum local contributions	2018	-3,8	66,5	397,8	464,3	325,3	108,1	29,3	378,3	905,6	34544,2	436532,1	-45,1	6,8	0,32
Main results Local															
RUN	YEAR	ADO3	AD	CD	ADCD	RHA	CHA	COU_C	CB	CB_C	WLD	RAD	MRAD	LC	IM
Total_Local	2018	13,7	287,3	1471,7	1759,1	1271	524,3	117,2	1462,6	3647,6	134394,2	1697026	161	26,5	1,28
Background_Local	2018	18,2	197	941,9	1138,8	861,9	376	75,2	958,5	2338,6	87946,1	1109086	212,6	17,4	0,82
Total Local contribution	2018	-4,5	90,3	529,8	620,3	409,1	148,3	42	504,1	1309	46448,1	587939,9	-51,6	9,1	0,46
Traffic_Local	2018	-3,8	4,7	76,6	81,4	167	0,8	3,4	44,8	107,2	4126,6	51734,9	-43,4	0,8	0,04
Residential_Local	2018	-0,2	85,9	467,9	553,9	237,9	149,1	38,5	457,9	1198,4	42194,2	534599,2	-1,5	8,3	0,42
B_Industry_Local	2018	0	0,2	1,2	1,5	0,8	0,3	0,1	1,1	2,7	95,2	1202,6	0	0	0
A_publicPower_Local	2018	-0,2	-0,1	2,9	2,9	4,4	-0,3	0	0,4	0,9	31,7	405,2	-1,4	0	0
Sum local contributions	2018	-4,2	90,7	548,6	639,7	410,1	149,9	42	504,2	1309,2	46447,7	587941,9	-46,3	9,1	0,46
Difference (total-background) and sectors sum	2018	0,3	0,4	18,8	19,4	1	1,6	0	0,1	0,2	-0,4	2	5,3	0	0
Abbreviations															
AD	"Acute" premature deaths from short term exposure of O3 and PM25														
CD	"Chronic" premature deaths from long-term exposure to PM25														
ADCD	Sum of AD and CD														
RHA	Respiratory hospital admissions														
CHA	Cardiovascular hospital admission														
COU_C	Asthma symptoms/cough														
CB	Chronic Bronchitis														
CB_C	Chronic Bronchitis - Children														
WLD	Work loss days														
RAD	Restricted activity days														
MRAD	Minor Restricted activity days														
LC	Lung Cancer														
IM	Infant Mortality														
PWM_PM25	Population weighted mean for PM25														

Figure xx. The raw data output from running the model on Sofia, here showing health impacts for different contributions.

The results will be visualized with a storyline and displayed as part of the CURE portal. Below is a draft of an online test interface that was developed during the project.

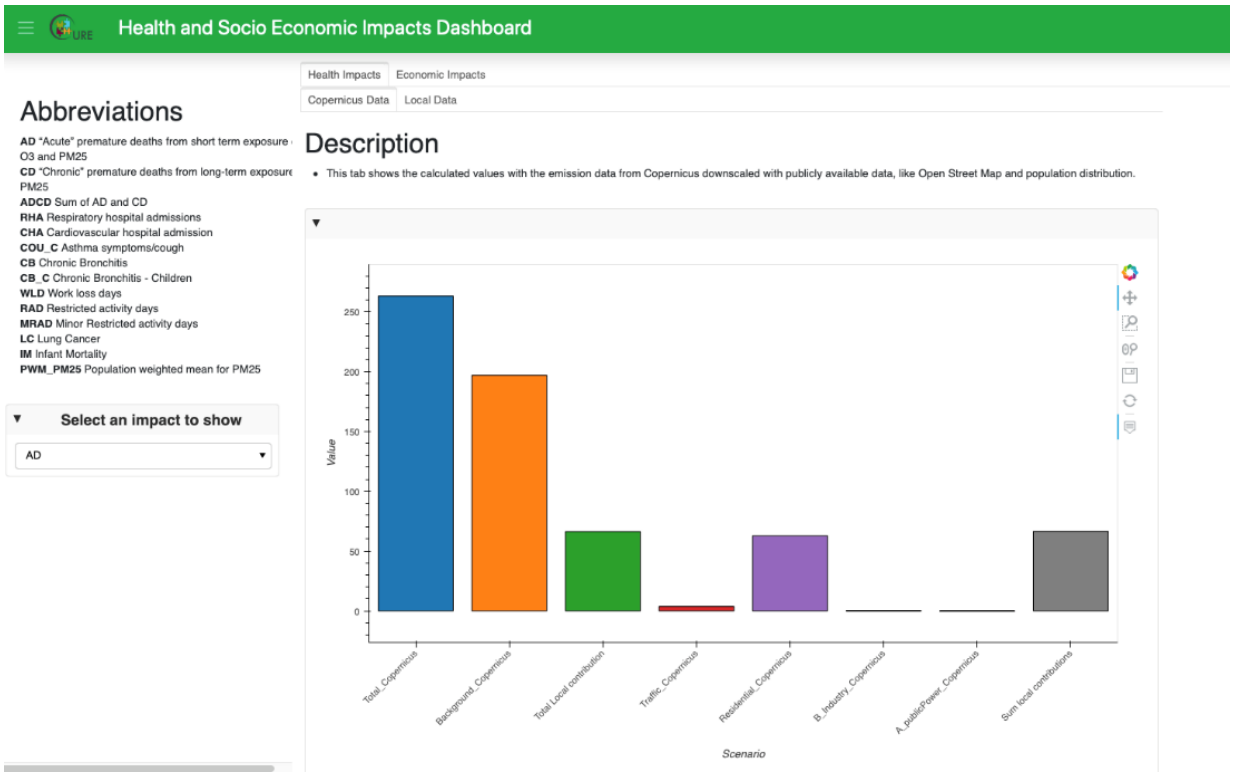

Figure 95. *Screenshot of draft interface of health and economic costs of air pollution for Sofia, Bulgaria (Frontrunner city). Shown here Acute Premature deaths (AD) based on Copernicus data (total, background, residential, traffic and industry, local).*

12.3 Evaluation

12.3.1 Uncertainties

There are considerable uncertainties associated with the calculation of health impacts and external costs related to air pollution.

A significant part of the uncertainty relates to the exposure-response relationships and especially to the exposure-response relationships implemented for NO_2. For the chronic mortality of NO_2, WHO recommends the application of a threshold of 20 µg/m^3, so that it is only concentrations above this threshold that contribute to the impact of NO_2 on chronic mortality. This threshold is therefore implemented in the calculations of the health impact of NO_2. However, there is considerable uncertainty connected with this threshold and the threshold might be too high or should be removed all together. This will have a significant influence on the results from the calculations and a decrease in the threshold will lead to a significant higher number of premature deaths attributable to NO2.

There are also large uncertainties related to the exposure-response relationships for O_3, where recent research indicates that O_3 at lower concentrations also has large impacts on human health. Until now, it has generally been accepted that the health impact of O_3 originates from

exposure to O_3 at high concentrations. New research (Im, 2018) indicates that O_3 concentrations as low as 10 ppb (= 20 µg/m^3) can have significant impact indicating the use of a lower threshold. This will lead to a higher impact from O_3 on health.

There is today very solid documentation for the health impacts related to $PM_{2.5}$. However, there is still a lack of scientific knowledge on which particular chemical constituents of $PM_{2.5}$ are responsible for the health impact. The recommendation from WHO is still to use the same exposure-response function for the different chemical constituents of $PM_{2.5}$ and the results from the EVA-model system is based on this assumption. Changes in this assumption will potentially lead to changes in the magnitude, sources and spatial distribution of the health impacts and external costs from air pollution.

12.3.2 Copernicus vs. Local data

It has been possible to compare Copernicus data with Local data in the case of Sofia, since both have been available for this city, based on air quality calculations made in App 7. Below, two examples of health costs based on Copernicus and Local data, respectively, are shown.

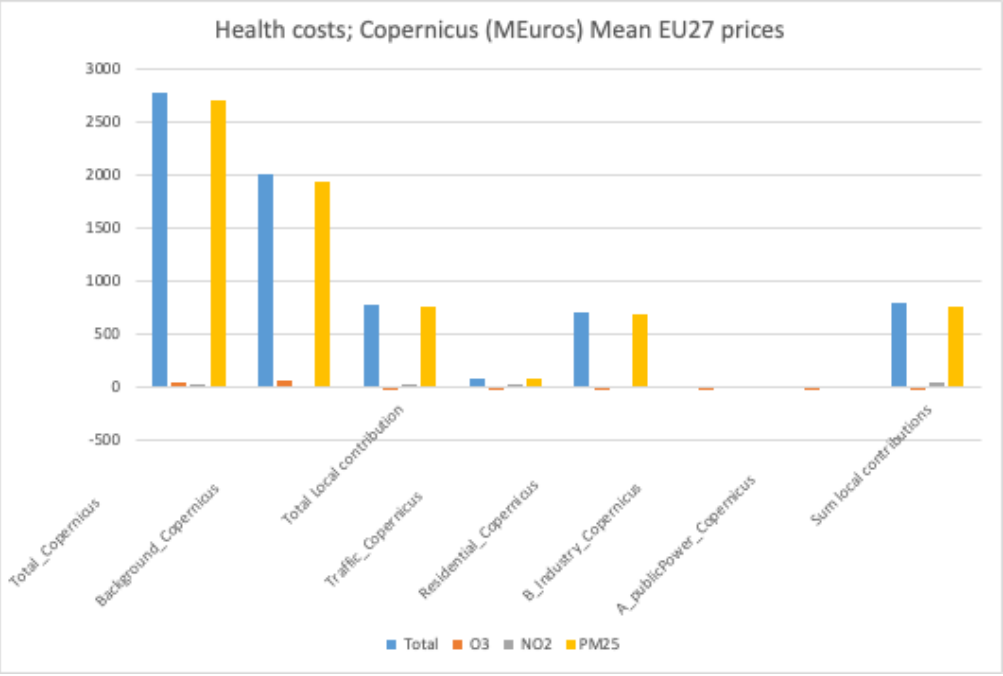

Figure 96. Health costs for Sofia, here showing Copernicus data for O3, NO2, PM2.5.

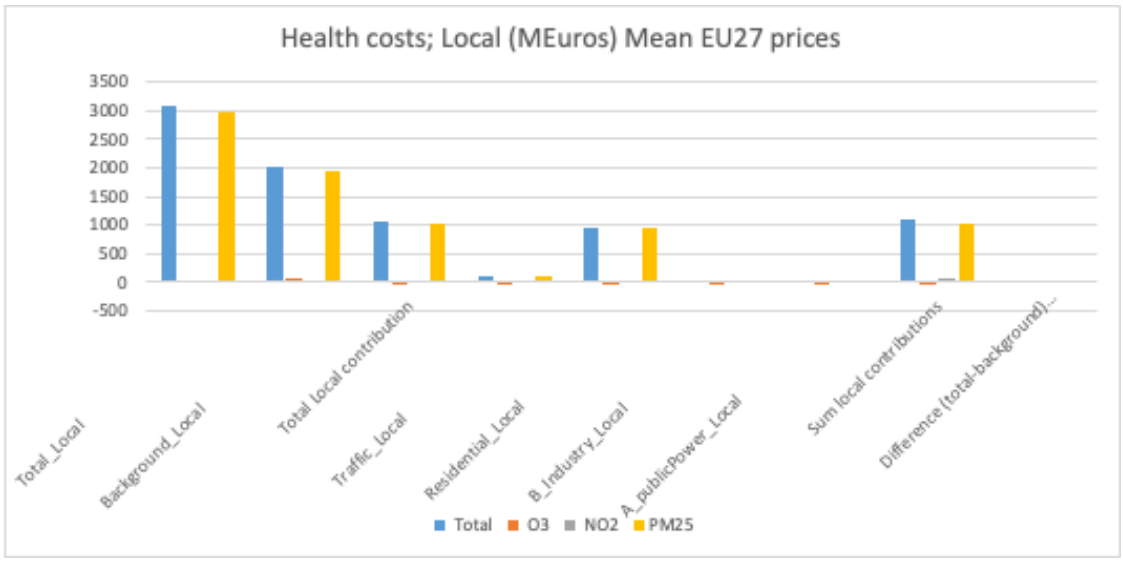

Figure 97. Health costs for Sofia, here showing Local data for O3, NO2, PM2.5.

A slight but not significant difference is seen in the values between the Copernicus and Local data. This makes it possible to upscale the application to other cities, regardless of the obtainability of local data. Of course, a more accurate result will occur from Local data, but this would in some cases require additional technological and economic resources. By showing the quite accurate results of the model run with Copernicus data, it could be a way forward to expand this to many cities at the same time thus lowering the costs of running the model.

REFERENCES

Andersen MS, Frohn LM, Nielsen JS, Nielsen M, Jensen SS, Christensen JH, Brandt J. A Non-linear Eulerian Approach for Assessment of Health-cost Externalities of Air Pollution. Proceedings of the European Association of Environmental and Resource Economists 16th Annual Conference; Gothenburg, Sweden. 25–28 June 2008; 2008. p. 23.

Aubinet, M., Vesala, T., Papale, D., 2012. Eddy Covariance – A Practical Guide to Measurement and Data Analysis. Springer Atmospheric Sciences

Berkowicz, R., Hertel, O., Larsen, S., Sørensen, N., Nielsen, M., 1997. Modelling traffic pollution in streets. URL: https://orbit.dtu.dk/files/128001317/Modelling_traffic_pollution_in_streets.pdf

Berkowicz, R., Ketzel. M., Lofstrom, P., Rordam, H., 2008. NO2 chemisty scheme in OSPM and other Danish models. URL: https://www2.dmu.dk/AtmosphericEnvironment/Docs/NO2scheme.pdf

Brutsaert, W., 1982. Evaporation into the Atmosphere. Springer Netherlands. ISBN: 978-90-481-8365-4

CAMS, 2019. The Copernicus Atmosphere Monitoring Service global and regional emissions (April 2019 version). https://doi.org/10.24380/d0bn-kx16

Christen, A., Coops, N.C., Crawford, B.R., Kellett, R., Liss, K.N., Olchovski, I., Tooke, T.R., Van Der Laan, M., Voogt, J.A., 2011. Validation of modeled carbon-dioxide emissions from an urban neighborhood with direct eddy-covariance measurements. *Atmos. Environ.* 45, 6057–6069. https://doi.org/10.1016/j.atmosenv.2011.07.040

Chrysoulakis, N., Grimmond, S., Feigenwinter, C., Lindberg, F., Gastellu-Etchegorry, J.-P., Marconcini, M., Mitraka, Z., Stagakis, S., Crawford, B., Olofson, F., Landier, L., Morrison, W., Parlow, E., 2018. Urban energy exchanges monitoring from space. *Sci. Rep.* 8, 11498. https://doi.org/10.1038/s41598-018-29873-x

Copernicus, 2020. Copernicus Space Component Data Access system (CSCDA) [WWW Document]. URL https://spacedata.copernicus.eu/ (accessed 12.9.20).

Crawford, B., Grimmond, C.S.B., Gabey, A., Marconcini, M., Ward, H.C., Kent, C.W., 2018. Variability of urban surface temperatures and implications for aerodynamic energy exchange in unstable conditions. Q. J. Royal Meteorol. Soc. 144, 1719-1741.

Cyrys J, Eeftens M, Heinrich J, Ampe C, Armengaud A, Beelen R, Bellander T, Beregszaszi T, Birk M, Cesaroni G, Cirach M, de Hoogh K, De Nazelle A, de Vocht F, Declercq C, Dedele A, Dimakopoulou K, Eriksen K, Galassi C, Graulevičiene R, Grivas G, Gruzieva O, Gustafsson

AH, Hoffmann B, Iakovides M, Ineichen A, Krämer U, Lanki T, Lozano P, Madsen C, Meliefste K, Modig L, Mölter A, Mosler G, Nieuwenhuijsen M, Nonnemacher M, Oldenwening M, Peters A, Pontet S, Probst-Hensch N, Quass U, Raaschou-Nielsen O, Ranzi A, Sugiri D, Stephanou EG, Taimisto P, Tsai MY, Vaskövi É, Villani S, Wang M, Brunekreef B, Hoek G (2012) Variation of NO2 and NOx concentrations between and within 36 European study areas: Results from the ESCAPE study. Atmos Environ 62:374–390 . doi: 10.1016/j.atmosenv.2012.07.080

De Ridder K., Lauwaet D., Maiheu B. 2015. UrbClim - a fast urban boundary layer climate model. Urban Climate 12, 21-48.

De Ridder K., Schayes G., 1997. The IAGL Land Surface Model, Journal of Applied Meteorology 36, 167–182.

Del Grosso, S.J., Parton, W.J., Derner, J.D., Chen, M., Tucker, C.J., 2018. Simple models to predict grassland ecosystem C exchange and actual evapotranspiration using NDVI and environmental variables. *Agric. Forest Meteorol.*, 249, 1-10.

EEA Report No 13/2017 Air Quality in Europe - 2017 report https://www.eea.europa.eu/publications/air-quality-in-europe-2017

EEA, 2019. Air quality in Europe 2019]. URL https://www.eea.europa.eu/publications/air-quality-in-europe-2019

ESA, 2019. Copernicus High Priority Candidate Missions [WWW Document]. URL https://www.esa.int/Applications/Observing_the_Earth/Copernicus/Candidate_missions (accessed 10.25.19).

European Ground Motion Service: Service Implementation Plan and Product Specification Document (2020), EEA https://land.copernicus.eu/user-corner/technical-library/egms-specification-and-implementation-plan

Feigenwinter, C., Vogt, R., Christen, A., 2012. Eddy Covariance Measurements Over Urban Areas, in: Eddy Covariance. Springer Netherlands, Dordrecht, pp. 377–397. https://doi.org/10.1007/978-94-007-2351-1_16

Foken, T., 2006. 50 Years of the Monin–Obukhov Similarity Theory. *Boundary-Layer Meteorol* 119, 431–447. https://doi.org/10.1007/s10546-006-9048-6

García-Díez M., Lauwaet D., Hooyberghs H., Ballester J., De Ridder K., Rodó X., 2016. Advantages of using a fast urban boundary layer model as compared to a full mesoscale model to simulate the urban heat island of Barcelona. Geoscientific Model Development 9, 4439–4450.

Grimmond, C.S.B., Oke, T.R., 1999. Heat Storage in Urban Areas: Local-Scale Observations and Evaluation of a Simple Model. J. Appl. Meteorol. 38, 922–940. https://doi.org/10.1175/1520-0450(1999)038<0922:hsiual>2.0.co;2

Hlavacova, I., Halounova, L., Stanislav, P.: Sentinel-1 INSAR processing of corner reflector information in the northern-bohemian coal basin. The International Archives of the Photogrammetry, Remote Sensing and Spatial Information Sciences, Volume XLI-B7, 2016 XXIII ISPRS Congress, 12–19 July 2016, Prague, Czech Republic.

Hooyberhs H, De Craemer S, Lefebvre W, Vranckx S, Maiheu B, Trimpeneers Em Vanpoucke C, Janssen S, Meysman F, Fierens F. 2020. Validation and optimization of the ATMO-Street model chain by means of a large-scale citizen-science dataset. In review

Im, U., Brandt, J., Geels, C., Hansen, K.M.,Christensen, J.H., Andersen, M.S., Solazzo, E., Alyuz, U., Balzarini, A., Baro, R., Bellasio, R., Bianconi, R., Bieser, J., Colette, A., Curci, G., Farrow, A., Flemming, J., Fraser, A., Jimenez-Guerrero, P., Kitwiroon, N., Pirovano, G., Pozolli, L., Prank, M., Rose, R., Sokhi, R., Tuccella, P., Unal, A., Vivanco, M.G., Yardwood, G., Hogrefe, C., Galmarini, S., 2018. Assessment and economic valuation of air pollution impacts on human health over Europe and the United States as calculated by a multi-model ensemble in the frame work of AQMEII3. Atmospheric Chemistry and Physics. 18, 5967–5989, 2018.

ISO (1989), Hot Environments - Estimation of the heat stress on working man, based on the WBGT-index (wet bulb globe temperature). ISO Standard 7243. Geneva: International Standards Organization.

Jensen, S.S., Ketzel, M., Becker, T., Christensen, J., Brandt, J., Plejdrup, M., Winther, M., Nielsen, O.K., Hertel, O., Ellermann, T., 2017. High resolution multi-scale air quality modelling for all streets in Denmark. Transp. Res. Part D Transp. Environ. 52, 322–339. https://doi.org/10.1016/j.trd.2017.02.019

Kanda, M., Inagaki, A., Miyamoto, T., Gryschka, M., Raasch, S., 2013. A new aerodynamic parametrization for real urban surfaces. *Boundary-Layer Meteorol.* 148, 357–377. https://doi.org/10.1007/s10546-013-9818-x.

Kanda, M., Kanega, M., Kawai, T., Moriwaki, R., Sugawara, H., 2007. Roughness Lengths for Momentum and Heat Derived from Outdoor Urban Scale Models. *J. Appl. Meteor. Climatol.*, 46, 1067 - 1079

Karagulian, F., Belis, C.A., Dora, C.F.C., Prüss-Ustün, A.M., Bonjour, S., Adair-Rohani, H., Amann, M., 2015. Contributions to cities' ambient particulate matter (PM): A systematic review of local source contributions at global level. Atmos. Environ. 120, 475–483. https://doi.org/10.1016/j.atmosenv.2015.08.087

Kato, S., Yamaguchi, Y., Liu, C. C., Sun C. Y., 2008. Surface Heat Balance Analysis of Tainan City on March 6, 2001 Using ASTER and Formosat-2 Data. *Sensors*, 8, 6026 - 6044

Khan, Z., Ludlow, D., Mitraka, Z., Chrysoulakis, N., Feigenwinter, C., Marconcini, M., Lauwaet, D., Hooyberghs, H., Soukup, T., Jupova, K., Torres, E.F., Kjær-Hansen, L., 2020. CURE Project Deliverable D1.1 Summary of User Requirements.

Kljun, N., Calanca, P., Rotach, M.W., Schmid, H.P., 2015. A simple two-dimensional parameterisation for Flux Footprint Prediction (FFP). *Geosci. Model Dev.* 8, 3695–3713. https://doi.org/10.5194/gmd-8-3695-2015

Kohsiek W., De Bruin H.A.R., The H., van den Hurk B.J.J.M., 1993. Estimation of the sensible heat flux of a semi-arid area using surface radiative temperature measurements. *Boundary-Layer Meteorol*, 63, 213–230

Kolomaznik, J., Hlavacova, I., Lazecky, M., Pelant, M. (2016) TACR CZ Certified method for terrain movements and deformation monitoring on transport infrastructure by means of SAR Interferometry http://www.gisat.cz/download/projekt/TACR/GST-TB0400MD003_D3_v1-1.pdf, Technological Agency CZ (TACR)

Kolomaznik, J., Hlavacova, I., Stonacek, V., Lorenzo, A. (2020) Earth Observation for Sustainable development: Detailed terrain deformation analysis in urban areas, EO4SD Service Technical Report.

Kotthaus, S., Smith, T.E.L., Wooster, M.J., Grimmond, C.S.B., 2014. Derivation of an urban materials spectral library through emittance and reflectance spectroscopy. ISPRS J. Photogramm. Remote Sens. 94, 194–212. https://doi.org/10.1016/j.isprsjprs.2014.05.005

Lauwaet D., De Ridder K., Saeed S., Brisson E., Chatterjee F., van Lipzig N.P.M., Maiheu B., Hooyberghs H., 2016. Assessing the current and future urban heat island of Brussels. Urban Climate, 15, 1-15.

Lauwaet D., Hooyberghs H., Maiheu B., Lefebvre W., Driesen G., Van Looy S., De Ridder K., 2015. Detailed Urban Heat Island projections for cities worldwide: dynamical downscaling CMIP5 global climate models. Climate, 3, 391-415.

Lauwaet D., Maiheu B., De Ridder K., Boënne W., Hooyberghs H., Demuzere M., Verdonck M.-L., 2020. A New Method to Assess Fine-Scale Outdoor Thermal Comfort for Urban Agglomerations. Climate, 8, 6; doi:10.3390/cli8010006.

Lazecky, M., Bakon, M., Sousa, J. J., Perissin, D., Hlavacova, I., Patricio, G., Papco, J.,Rapant, P., Real, N. (2015) Potential of Multi-Temporal InSAR Techniques for Structural Health Monitoring, Proceedings of [FP1] FRINGE'15, http://proceedings.esa.int/files/324.pdf

Lazecky, M., Jirankova, E., Bohmova, D. (2010). Usage of insar techniques to detect and monitor terrain subsidence due to mining activities. https://www.researchgate.net/publication/277748130_Usage_of_insar_techniques_to_detect_and_monitor_terrain_subsidence_due_to_mining_activities

Lefebvre, W., Degraeuwe, B., Beckx, C., Vanhulsel, M., Kochan, B., Bellemans, T., Janssens, D., Wets, G., Janssen, S., De Vlieger, I., Int Panis, L., Dhondt, S., 2013b. Presentation and evaluation of an integrated model chain to respond to traffic- and health-related policy questions. Environ. Model. Softw. 40, 160–170.

Lefebvre, W., Van Poppel, M., Maiheu, B., Janssen, S., Dons, E., 2013a. Evaluation of the RIO-IFDM-street canyon model chain. Atmos. Environ. 77, 325–337. https://doi.org/10.1016/j.atmosenv.2013.05.026

Lefebvre, W., Vercauteren, J., Schrooten, L., Janssen, S., Degraeuwe, B., Maenhaut, W., de Vlieger, I., Vankerkom, J., Cosemans, G., Mensink, C., Veldeman, N., Deutsch, F., Van Looy, S., Peelaerts, W., Lefebre, F., 2011. Validation of the MIMOSA-AURORA-IFDM model chain for policy support: Modeling concentrations of elemental carbon in Flanders. Atmos. Environ. 45, 6705–6713. https://doi.org/10.1016/j.atmosenv.2011.08.033

Lemke B., Kjellstrom T. (2012) Calculating Workplace WBGT from Meteorological Data: A Tool for Climate Change Assessment. Industria Health 50, 267–278.

Leuning R, Kelliher FM, De Pury DGG, Schulze ED, *Plant. Cell Environ.* 18, 1183–1200 (1995).

Li, H., Zhou, Y., Li, X., Meng, L., Wang, X., Wu, S., Sodoudi, S. (2018). A new method to quantify surface urban heat island intensity. Science of The Total Environment 624, 262–272.

Liljegren J.C., Carhart R.A., Lawday P., Tschopp S., Sharp R. (2008) Modeling the Wet Bulb Globe Temperature Using Standard Meteorological Measurements. Journal of Occupational and Environmental Hygiene 5(10), 645-655. DOI:10.1080/15459620802310770.

Lindberg, F., Grimmond, C.S.B., Gabey, A., Huang, B., Kent, C.W., Sun, T., Theeuwes, N.E., Järvi, L., Ward, H.C., Capel-Timms, I., Chang, Y., Jonsson, P., Krave, N., Liu, D., Meyer, D., Olofson, K.F.G., Tan, J., Wästberg, D., Xue, L., Zhang, Z., 2018. Urban Multi-scale Environmental Predictor (UMEP): An integrated tool for city-based climate services. *Environ. Model. Softw.* 99, 70–87. https://doi.org/10.1016/j.envsoft.2017.09.020

Marconcini, M., Gorelick, N., Metz-Marconcini, A., Esch, T. (2018). Mapping the Global Settlement Growth from 1985 to 2015 - the World Settlement Footprint Evolution Dataset. 2018 AGU Fall Meeting Conference Paper

Marconcini, M., Metz-Marconcini, A., Üreyen, S. et al. Outlining where humans live, the World Settlement Footprint 2015. Sci Data 7, 242 (2020).

Minderhoud, P. S. J., Hlavacova, I., Kolomaznik, J., and Neussner, O.: Towards unraveling total subsidence of a mega-delta – the potential of new PS InSAR data for the Mekong delta, Proc. IAHS, 382, 327–332, https://doi.org/10.5194/piahs-382-327-2020, 2020

MINH D, Hanssen R, Rocca F.: Radar Interferometry: 20 Years of Development in Time Series Techniques and Future Perspectives. Remote Sens. 2020, 12, 1364, doi:10.3390/rs12091364

Mitraka, Z., Chrysoulakis, N., Doxani, G., Del Frate, F., Berger, M., 2015. Urban Surface Temperature Time Series Estimation at the Local Scale by Spatial-Spectral Unmixing of Satellite Observations. Remote Sens. 7, 4139–4156. https://doi.org/10.3390/rs70404139

Mitraka, Z., Chrysoulakis, N., Kamarianakis, Y., Partsinevelos, P., Tsouchlaraki, A., 2012. Improving the estimation of urban surface emissivity based on sub-pixel classification of high resolution satellite imagery. Remote Sens. Environ. 117, 125–134. https://doi.org/10.1016/j.rse.2011.06.025

NASA/METI/AIST/Japan Spacesystems, and U.S./Japan ASTER Science Team. ASTER Level 2 Surface Temperature Product. 2001, distributed by NASA EOSDIS Land Processes DAAC, https://doi.org/10.5067/ASTER/AST_08.003. Accessed 2020-12-10.

Offerle, B., Grimmond, C. S. B, Oke, T. R. 2003. Parameterization of Net All-Wave Radiation for Urban Areas, *Journal of Applied Meteorology*, 42(8), pp. 1157–1173. doi: 10.1175/1520-0450(2003)042<1157:PONARF>2.0.CO;2.

Offerle, B., Grimmond, C.S.B.B., Fortuniak, K., 2005. Heat storage and anthropogenic heat flux in relation to the energy balance of a central European city centre. Int. J. Climatol. 25, 1405–1419. https://doi.org/10.1002/joc.1198

Oke, T.R., Mills, G., Christen, A., Voogt, J.A., 2017. Urban Climates. Cambridge University Press, Cambridge. https://doi.org/10.1017/9781139016476

Parastatidis, D., Mitraka, Z., Chrysoulakis, N., Abrams, M., 2017. Online Global Land Surface Temperature Estimation from Landsat. Remote Sens. 9, 1208. https://doi.org/10.3390/rs9121208

Pepe, A., Calò, F. (2017) A review of interferometric synthetic aperture RADAR (InSAR) multi-track approaches for the retrieval of Earth's surface displacements Appl. Sci., 7 (12), 1264: https://www.mdpi.com/2076-3417/7/12/1264/htm

Pope CA, Burnett RT, Thun MJ, Calle EE, Krewski D, Ito K, Thurston GD. Lung cancer, cardiopulmonary mortality and long-term exposure to fine particulate air pollution. JAMA-J Am Med Assoc. 2002;287:1132–1141.

Poursanidis, D., Mitraka, Z., Somarakis, G., Dohr, M., Chrysoulakis, N., 2020. CURE Project Deliverable D7.4 Data Management Plan.

Stagakis, S., Chrysoulakis , N., Spyridakis , N., Feigenwinter, C., Vogt, R., 2019. Eddy Covariance measurements and source partitioning of CO_2 emissions in an urban

environment: Application for Heraklion, Greece . *Atm. Environ*., 201, 278-292. https://doi.org/10.1016/j.atmosenv.2019.01.009

Triantafyllou I, Karavias A, Koukouvelas I, Papadopoulos GA, Parcharidis I. 2022. "The Crete Isl. (Greece) Mw6.0 Earthquake of 27 September 2021: Expecting the Unexpected" GeoHazards 3, no. 1: 106-124.

U.S. Army (2003) Technical Bulletin Medical 507 and Air Force Pamphlet 48-152(I). Heat stress control and heat casualty management.

Voogt, J.A., Grimmond, C.S.B., 2000. Modeling Surface Sensible Heat Flux Using Surface Radiative Temperatures in a Simple Urban Area. *J. Appl. Meteorol.* 39, 1679–1699. https://doi.org/10.1175/1520-0450-39.10.1679

Ward, H. C. *et al.* (2016) 'Surface Urban Energy and Water Balance Scheme (SUEWS): Development and evaluation at two UK sites', *Urban Climate*, 18, pp. 1–32. doi: 10.1016/j.uclim.2016.05.001.

WHO, 2016. Ambient air pollution: A global assessment of exposure and burden of disease. URL: https://www.who.int/publications/i/item/9789241511353

WHO. Health risks of air pollution in Europe – HRAPIE: Recommendations of concentration-response functions for cost-benefit analysis of particulate matter, ozone and nitrogen dioxide. World Health Organization; [last access: 25 April 2018]. 2013. available at: http://www.euro.who.int/__data/assets/pdf_file/0006/238956/Health_risks_air_pollution_HRAPIE_project.pdf?ua=1.

Willett, K. M. & Sherwood, S. (2012) Exceedance of heat index thresholds for 15 regions under a warming climate using the wet-bulb globe temperature. Int. J. Climatol., 32, 161–177.

Yoshida, A., Tominaga, K. and Watatani, S. (1990) 'Field measurements on energy balance of an urban canyon in the summer season', *Energy and Buildings*, 15(3–4), pp. 417–423. doi: 10.1016/0378-7788(90)90016-C.

Yoshida, A., Tominaga, K. and Watatani, S. (1991) 'Field investigation on heat transfer in an urban canyon', *Heat Transfer - Japanese Research; (United States)*. Available at: https://www.osti.gov/biblio/5496556.

Zhou B., Lauwaet D., Hooyberghs H., De Ridder K., Kropp J. P., Rybski D., 2016. Assessing seasonality in the surface urban heat island of London. Journal of Applied Meteorology and Climatology, 55, 493-505.